Experimental Study of the Formation of Liquid Saline Water on Mars

by

Erik Fischer

A dissertation submitted in partial fulfillment
of the requirements for the degree of
Doctor of Philosophy
(Climate and Space Sciences and Engineering)
in the University of Michigan
2018

Doctoral Committee:

Professor Nilton O. Rennó, Co-Chair
Dr. Germán M. Martínez, Co-Chair
Professor Emeritus John R. Barker
Professor Sara A. Pozzi

Erik Fischer

erikfis@umich.edu

ORCID iD: 0000-0002-2098-5295

DEDICATION

In dedication to my grandparents,

my parents, my brother and Varsha.

Ad Astra

ACKNOWLEDGEMENTS

I would like to thank NASA for the financial support of this research through the Astrobiology Program: Exobiology and Evolutionary Biology, award # 09-EXOB09-0050 and through the Mars Data Analysis Program, award # 14-MDAP14_2-0113. I want to thank the German Academic Exchange Service for the financial support during my first year here at Michigan.

I would like to thank my committee members for taking their time to serve on my PhD committee and for their excellent suggestions.

I am very grateful to my advisors: Professor Nilton O. Rennó and Dr. Germán M. Martínez. Nilton, thank you for giving me the opportunity to join your research group and dive into Martian research. Thank you both for your continued help in finding funding throughout my Ph.D. and onwards, your excellent and meticulous suggestions in academic writing and our open-minded group meetings and the long discussions of ideas after. Thank you for always being available for questions and help. Germán, thank you for giving me great insight into the early part of an academic career, from postdoc to tenure-track positions. Thank you for your tutoring and friendship. Thank you both for giving me the opportunity to be a part of the Mars Science Laboratory mission and hopefully soon also the Mars 2020 mission. I could not imagine a better team of advisors.

I would also like to thank the University of Michigan and especially the Department of Climate and Space Sciences and Engineering for providing a great academic environment to foster my research.

Thank you to all my friends, old and new, in Germany and the US. There is no better way to take my mind off work than by spending time with you. Special thanks to Doug, Shrikant, Pooja, Anup, Brandon, Liz, Maria, Germán and Sebastian.

Further, I would like to thank all my lab mates throughout the years: Harvey, Álvaro, Cauê, Doug, Max, Dave, Durval, Chase, Shaneen and Daniel. Thank you all for providing a great work environment.

I am extremely grateful to my family: Mutti, Vati, Hagen, Oma und Opa, besten Dank für eure Unterstützung und Ratschläge in meinem Studium und Leben sowohl in Deutschland als auch hier in den USA. Ich freue mich immer auf jeden Besuch zu Hause. Holger, Jule, Annika, Anett und Heiko besten Dank an euch, ich genieße jedes Familientreffen, ob im kleineren Rahmen im Urlaub oder alle beisammen zur Weihnachtszeit.

Finally, Varsha, I am most thankful to you. You are always there to celebrate accomplishments but also to get through rough times. Thank you for your great support throughout this endeavor and beyond. You always keep my feet on the ground and my eyes on the goal.

TABLE OF CONTENTS

DEDICATION ..... **ii**

ACKNOWLEDGEMENTS ..... **iii**

LIST OF TABLES ..... **ix**

LIST OF FIGURES ..... **xii**

LIST OF APPENDICES ..... **xix**

LIST OF UNCOMMON SYMBOLS AND ACRONYMS ..... **xx**

ABSTRACT ..... **xxiii**

CHAPTER I Introduction **1**

1.1 An Overview of Mars 1

1.1.1 Mars in the Solar System 1

1.1.2 The Martian Atmosphere 2

1.1.3 The Martian Surface 3

1.2 Past, Current and Future Mars Exploration 5

1.3 Water on Mars: The Motivation for this Work 10

CHAPTER II The Michigan Mars Environmental Chamber **16**

2.1 Overview 16

2.2 Pressure Control 17

2.3 Temperature Control 18

2.4 Relative Humidity Control 19

2.5 Supporting Instruments 20

CHAPTER III Searching for Brine on Mars Using Raman Spectroscopy 22

Abstract 22

3.1 Introduction 23

3.2 Methods and Setup 25

3.3 Results 27

3.4 Discussion 34

3.5 Conclusion 37

CHAPTER IV Experimental Evidence for the Formation of Liquid Saline Water on Mars 39

Abstract 39

4.1 Introduction 40

4.2 Methodology 41

4.2.1 Environmental Chamber 41

4.2.2 Raman Spectroscopy 42

4.3 Results 44

4.3.1 Spectra of Single Components 44

4.3.2 Spectra of Brine Formation Experiments 46

4.4 Discussion and Conclusion 50

CHAPTER V Formation and Persistence of Brine on Mars: Experimental Simulations throughout the Diurnal Cycle at the Phoenix Landing Site 52

Abstract 52

5.1 Introduction 53

5.2 Experimental Setup 55

5.3 Results 60

5.3.1 First Experiment: Diurnal Cycle of Salt Deposited on Ice at Martian Polar Surface Conditions 60

5.3.2 Second Experiment: Effect of a Subsequent Diurnal Cycle 63

5.3.3 Third Experiment: Diurnal Cycle of Initially Frozen Brine at Martian Polar Surface Conditions 66

5.3.4 Fourth Experiment: Diurnal Cycle of Initially Frozen Brine at the Environmental Conditions of the Phoenix Strut 70

5.4 Discussion 72

5.5 Conclusion 75

CHAPTER VI Recalibration of the Phoenix Mission's Relative Humidity Sensor 76

Abstract 76

6.1 Introduction 77

6.2 Setup and Methodology 80

6.2.1 Environmental Chamber 80

6.2.2 TECP Engineering Unit vs Flight Unit 81

6.2.3 A New Calibration Function 83

6.3 Results 84

6.4 Discussion 87

6.5 Conclusion..... 90

CHAPTER VII Summary and Conclusions 91

CHAPTER VIII Future Work..... 95

8.1 Brine Kinetics..... 95

8.2 Mixed Salts..... 97

8.3 Planetary Protection 97

8.4 Mission Support 99

APPENDICES 100

BIBLIOGRAPHY 111

LIST OF TABLES

1.1 Basic planetary parameters of Mars……2

1.2 Comparison of the abundance of Martian atmospheric constituents with those of Earth…….3

3.1 Decomposed peak positions and widths (in parentheses) of the Raman spectra shown in this study. Asterisks indicate weak peaks with low intensities……..28

4.1 Spectral Signatures of Calcium Perchlorate, Liquid Water, and Water Ice. Values in parentheses are FWHM values for each peak……....45

5.1 Gaussian components of the O-H stretching band of the reference Raman spectra of $Ca(ClO_4)_2 \cdot 4H_2O$, water ice, and liquid water (left) [*Zhang and Chan*, 2003; *Fischer et al.*, 2014], as well as of the Raman spectra shown in Fig. 5.5 (right). Each column contains the wavenumber and FWHM of each spectral peak. The values of the spectral peaks and their FWHM are color-coded to indicate the presence of salt (black), water ice (blue), either water ice or liquid water (gray), and liquid water (red). The Gaussian components of the spectrum taken at 00:10, when the temperature is below the eutectic value, contain spectral peaks of hydrated perchlorate salt and water ice. In spite of the temperature being above the eutectic value and the image of the sample indicating that the ice starts to melt at 04:37, spectral peaks corresponding to liquid water are not observed at 05:15. The fact that the signal of the ice at the bottom of the sample is stronger at this time (the appearance of a shoulder caused by the 3068cm^{-1} ice spectral peak and a general increase in intensity of all spectral peaks of ice, as shown in Fig. 5.5) provides indirect evidence that the ice has started to melt. The ice signal likely increases because the salt becomes more translucent when it absorbs liquid water. At 08:00 the Raman spectrum indicates the presence of liquid water unambiguously. The spectral peak at ~3129 cm^{-1} indicates that water ice is still present, but by 11:00 this peak has disappeared. Evaporation of water causes the salt concentration of the solution to increase continuously until a salt crust forms at 13:45 (Fig. 5.7e). At this time, the Gaussian components still contain spectral peaks corresponding to brine because the signal from the thin crust is weak. Evaporation thickens the salt crust until crystalline calcium perchlorate hydrates dominate the spectrum at 23:55. The brine freezes below the salt crust when the temperature decreases below the eutectic value. The Gaussian components fit the full measured spectrum with accuracy $\bar{R}^2 \geq 0.98\%$.....64

5.2 As in Table 5.1, but for the second experiment. The Gaussian decomposition of the spectrum at 13:45 shows a liquid water peak at 3539 cm^{-1}, indicating that the sample is brine when the salt crust forms (see Fig. 5.10a). Another peak at 3328 cm^{-1} seems to indicate the presence of ice, but this is unlikely because the temperature at 13:45 is the warmest of Sol 19, about 60 K above the eutectic point, and the sample was initially prepared as a saturated solution. A peak at a lower wavenumber (closer to the 3230 cm^{-1} peak in the water reference) with a slightly different FWHM leads to a similar accuracy for the complete decomposition. We believe that this is caused by inaccuracies in peak positions when wide FWHM values occur in the Gaussian decomposition, as it is the case for the 3328 cm^{-1} peak in this decomposition. Ambiguities in the detection of phase changes using Gaussian decomposition will be described in more detail in a future study. Only salt and ice peaks are present at 23:55 because most of the water in the sample has evaporated and the remaining solution is frozen (see Fig. 5.10b). The Gaussian decomposition does not change until 03:25, when an additional ice peak at 3114 cm^{-1} appears (see Fig. 5.8). At this time the frozen solution in the sample is whitish and opaque, similar to the material found in the Dodo-Goldilocks trench by the Phoenix lander (Fig. S2). At 04:25 the peak at 3114 cm^{-1} and the white color disappear (Fig. 5.10e). This happens when the temperature exceeds the eutectic value. At 06:40, about 2 h after exceeding the eutectic temperature, no peak indicating brine is detected, suggesting that the frozen solution is whitish because it is nearly salt-saturated. Most of the water substance has either evaporated or sublimated, and not enough water is available to form brine in a subsequent diurnal cycle…….67

5.3 As in Table 5.1, but for the third experiment. At 04:00 the spectrum contains ice and salt peaks, as well as a single water peak at 3559 cm^{-1}. The presence of the water peak might be caused by small amounts of brine in the ice even at temperatures far below the eutectic value. This behavior was also observed at the end of the fourth experiment, when brine remained liquid even after the sample was kept below the eutectic temperature for at least 30 min (Table 5.4). The spectral decomposition has barely changed by 05:30, when the eutectic temperature has been exceeded and brine starts to become visible in the image (Fig. 5.13b). At 07:00 the salt peak disappears, and only water and ice peaks are left, consistent with Fig. 5.13c. At 11:45 the ice has melted completely, and the ice peaks have disappeared from the spectrum. Only liquid water peaks remain until the onset of a crust formation at 14:30. The onset of brine and crust formation occurs 45 min later than in the first experiment……69

5.4 As in Table 5.1, but for the fourth experiment. The decomposition of the frozen mix at 01:15 contains ice and salt peaks. Despite exceeding the eutectic temperature at 01:30, spectral changes have not occurred by 04:25. This might be explained by a lower rate of temperature increase after crossing the eutectic temperature (Fig. 4) than that occurring on the ground (Fig. 2). The ice peaks start to disappear after ~04:30 and are completely gone by 12:35, with only the liquid water peaks remaining. This change is also visible in Fig. 5.16d, showing the remaining ice melting. The spectrum does not change from 17:15 until the end of the experiment, with the sample staying liquid even during the last 30 min of the experiment when the temperature decreases below the eutectic value.

In this experiment, a salt crust does not form on the sample because the lower maximum temperature and near-saturated air mitigate evaporation……73

A.1 Characteristics of the Gaussian decompositions of the spectra shown in the figures of this letter. This data is necessary to reproduce decomposition figures from the main body and figures in the auxiliary material……101

LIST OF FIGURES

1.1 Topography of the Martian surface based on Mars Orbiter Laser Altimeter (MOLA) measurements, showing the strong north/south dichotomy in elevation. Image credit: NASA/JPL/GSFC…….....4

1.2 Stability diagram of $Ca(ClO_4)_2$, $Mg(ClO_4)_2$ and $NaClO_4$ salts. The colored dashed lines represent the deliquescence relative humidity at which the various salts form aqueous solutions. The eutectic temperatures of $Ca(ClO_4)_2$, $Mg(ClO_4)_2$ and $NaClO_4$ are shown in their respective colors…….11

1.3 (a) Spheroids on the strut of the PHX lander at various sols and times. The spheroids are largest and most spherical at around midafternoon on Sol 44, probably because the RH and temperature have reached peak values and the spheroids are liquid brine, grown by deliquescence [*Renno et al.*, 2009]. (b) Sol 19 Surface Stereo Imager image of the first trench dug by the Phoenix Robotic Arm. Ice was exposed and removed with little effort, suggesting that it was either saline ice or layered ice formed in the presence of brines. From *Renno et al.* [2009]……12

1.4 HiRISE images showing RSL activity in the central peaks of Horowitz crater. From *Ojha et al.* [2015]…….....13

1.5 An example of a slope streak on a hill in Cerberus Tholi (8°N, 163°E). From *Kreslavsky and Head* [2009]…….14

2.1 Layout of the Michigan Mars Environmental Chamber, including its pressure, temperature and relative humidity control system……..17

3.1 Setup of the Michigan Mars Environmental Chamber (MMEC)…….....26

3.2 Decomposition of the Raman spectrum of liquid water in the O-H stretching vibrational band…….....29

3.3 Decomposition of the Raman spectrum of water ice in the O-H stretching vibrational band…….....30

3.4 Decomposition of the Raman spectrum of hydrated perchlorate salt. (a) Perchlorate symmetric stretching band. (b) O-H stretching vibrational band…….31

3.5 Decomposition of the Raman spectrum of a perchlorate salt solution. (a) Perchlorate symmetric stretching band. (b) O-H stretching vibrational band…….....32

3.6 Decomposition of the Raman spectrum of a saturated perchlorate salt solution. (a) Perchlorate symmetric stretching band. (b) O-H stretching vibrational band……..34

3.7 Decomposition of the Raman spectrum of a dried out perchlorate salt solution. (a) Perchlorate symmetric stretching band. (b) O-H stretching vibrational band……..35

4.1 Decomposed Raman spectra of $Ca(ClO_4)_2 \cdot 4H_2O$, water ice, and liquid water: (a) The decomposed O-H vibrational spectrum of hydrated $Ca(ClO_4)_2$ at -50°C, 800 Pa, and 100% RH shows eight Gaussian components, at 3446, 3471, 3487, 3515, 3542, 3564, 3603, and 3628 cm^{-1}, with $\bar{R}^2 \geq 0.999$. (b) Water ice at -80°C and 800 Pa indicating five Gaussian components, at 3046, 3115, 3227, 3336, and 3399 cm^{-1}, with $\bar{R}^2 \geq 0.997$. (c) Decomposition of the O-H vibrational region of the spectrum of liquid water [*Zhang and Chan*, 2003], indicating four broad Gaussian components, at 3230, 3420, 3540, and 3620 cm^{-1}, with $\bar{R}^2 \geq 0.997$……...45

4.2 (a) Raman spectra of $Ca(ClO_4)_2 \cdot 4H_2O$ exposed to saturated air. The spectra do not show evidence for deliquescence even after the sample has been kept at T = -50°C (about 25°C above $T_e \approx$ -74°C) and RH = 100% for 205 min. The values shown in the figure correspond to the spectral peaks of the Gaussian decomposition of the 205 min curve. Analysis of this decomposition indicates that all significant spectral peaks in the O-H stretching region correspond to hydrates. The appearance of a small peak at 936 cm^{-1} indicates a partial change to $Ca(ClO_4)_2 \cdot 8H_2O$. (b) Decomposed O-H vibrational spectrum of the 205 min curve. It shows eight Gaussian components at 3447, 3470, 3486, 3516, 3541, 3562, 3604, and 3628 cm^{-1}, all except one of them with FWHM ≤ 50 cm^{-1}. Comparison with Figure 4.1a and Table 4.1 shows that these components indicate the presence of crystalline hydrated $Ca(ClO_4)_2$. $\bar{R}^2 \geq 0.999$……...47

4.3 (a) Spectra of $Ca(ClO_4)_2 \cdot 4H_2O$ in contact with water ice. The values shown in the figure correspond to the spectral peaks of the Gaussian decomposition of the -56°C curve. The blue and green curves contain spectral peaks indicating the presence of hydrated salt and water ice, similar to those shown in Figure 4.2 (see Table 4.1). The orange and red curves contain broad spectral peaks at ~3545 and 3605 cm^{-1}, indicating the formation of liquid brines by melting of the water ice within ~3 h after the beginning of the experiment. (b) Decomposed O-H vibrational band of the spectrum of $Ca(ClO_4)_2$ in contact with ice at -75°C. It shows 12 Gaussians components: at 3067, 3120, 3236, and 3410 cm^{-1} indicating the presence of ice and at 3440, 3468, 3487, 3510, 3536, 3577, 3602, and 3630 cm^{-1} indicating the presence of crystalline hydrated salt. $\bar{R}^2 \geq 0.999$. (c) Decomposed O-H vibrational band of the spectrum at -56°C. It shows seven Gaussians components at 3060, 3127, and 3356 indicating the presence of ice, at 3250 and 3424 cm^{-1} indicating the presence of liquid water or ice, and at 3545 and 3605 cm^{-1} indicating the presence of liquid water, all except one with a width of FWHM > 50 cm^{-1}. $\bar{R}^2 \geq 0.999$…….49

5.1 Environmental conditions on Sol 19, when “soft ice” was unveiled by the Phoenix robotic arm in the Dodo-Goldilocks trench. The black and gray lines represent values from numerical simulations of the ground temperature and frost point of the surrounding air at the Phoenix landing site, while red and blue crosses represent the temperature and frost point measured inside the MMEC. The ground temperature first exceeds the $Ca(ClO_4)_2$ eutectic value (199 K) at 04:32, about 5 min before the first visual evidence for the formation of brine in the MMEC. Detailed calculations of the environmental conditions on this sol are provided in the Appendix……...56

5.2 As in Fig. 5.1, but for the second experiment. To ensure similar sample conditions as in the first experiment, the second experiment started with brine at the beginning of crust formation at 13:45. The experiment ended at 06:30 of the next sol, about 2 h after the sample temperature exceeded the eutectic value…….58

5.3 As in Fig. 5.1, but starting with a mix of water ice and calcium perchlorate at 04:00. Similar to the first experiment, the MMEC closely simulates the temperature in the trench (red crosses), but it overshoots the frost point temperature values inferred from the Phoenix measurements between 06:00 and 15:00 (blue crosses)……..59

5.4 Sol 19 temperature at 0.5 m above the ground (the height of place on the Phoenix strut where spheroids were observed) at the Phoenix landing site. The black curve represents the diurnal evolution of the temperature (0.5 m above the surface), while red crosses represent the temperature experimentally simulated in the MMEC. The frost point temperature was not simulated in this experiment. The diurnal temperature cycle at 0.5m height has lower amplitude than at the ground, with higher minimum and lower maximum temperatures. This causes the brine to stay liquid for most of the diurnal cycle……...59

5.5 Raman spectra in the O-H stretching band throughout the full diurnal cycle shown in Fig. 5.1 (first experiment). The wavenumber and FWHM of the Gaussian components of each spectrum are shown in Table 5.1. The appearance of the broad peak at 3578 cm^{-1} in the spectrum taken at 08:00 clearly indicates the presence of liquid solution……62

5.6 As in Fig. 5.5, but for the perchlorate vibration band. In the spectrum taken at 08:00, the ~954 cm^{-1} peak of crystalline $Ca(ClO_4)_2 \cdot 4H_2O$ shifted toward ~936 cm^{-1}, consistent with the presence of liquid solution. After the sample dries out at the end of the experiment, this peak does not shift back, indicating that it is not an unambiguous indicator for the presence of liquid brine……...62

5.7 Images of the sample color-coded according to the spectra shown in Figs. 5.5 and 5.6. (a) Salt on top of ice at the start of the experiment at 00:10 when the temperature is below the eutectic value. (b) Evidence for brine at 05:15, shortly after the eutectic temperature is exceeded. (c) Salt has completely dissolved, but water ice is still present at 08:00. (d) Only brine is present at 11:00. (e) Evidence for the presence of a salt crust at 13:45. The salt crust can be distinguished from the liquid by its different reflective properties. (f)

Mainly crystalline salt hydrates with frozen brine below it at end of the diurnal cycle at 23:55…….....63

5.8 Raman spectra in the O-H stretching band throughout the partial diurnal cycle shown in Fig. 5.2 (second experiment). Gaussian components of each spectrum are shown in Table 5.2. A change from the smooth curve representing salt-saturated brine (black) to the narrow peaks indicating crystalline salt is observed……65

5.9 As in Fig. 5.8, but for the perchlorate vibration band. This experiment starts with brine and ends with hydrated calcium perchlorate. The perchlorate peak remains at 936 cm^{-1} during the entire experiment……...65

5.10 Images of the sample color-coded according to spectra shown in Figs. 5.8 and 5.9. (a) Evaporation of water causes a salt crust to start to form at 13:45. (b) Mainly crystalline perchlorate hydrates at the end of the diurnal cycle at 23:55. (c) The frozen brine starts to become white at 02:05. (d) Whitish frozen brine at 03:25, similar to the material found in the Dodo-Goldilocks trench. (e) The sample becomes translucent again after the eutectic temperature is exceeded at 04:25 and the remaining ice partially melts. (f) Wet calcium perchlorate hydrates at 06:40, with no evidence for brine. The fact that brine is not observed even 2 h after the eutectic temperature has been exceeded indicates that the sample lacks bulk water (frozen brine at 03:25 is whitish because it is nearly salt-saturated and therefore lacks bulk water)……66

5.11 Raman spectra in the O-H stretching band throughout the partial diurnal cycle shown in Fig. 5.3 (third experiment). Gaussian components of each spectrum are shown in Table 5.3……...68

5.12 As in Fig. 5.11, but for the perchlorate vibration band. The perchlorate peak at 936 cm^{-1} is at a similar location for both, the mix of water ice and salt (frozen brine) (black curve) and brine (green and cyan curves), indicating that it is not an unambiguous indicator of brine……68

5.13 Images of the sample color-coded according to the spectra shown in Figs. 5.11 and 5.12. (a) Frozen mix of water ice and perchlorate salt at 04:00 at 195 K after preparing the sample at 150 K. The darker color compared to the whitish frozen brine in the second experiment shown in Fig. 5.10d is likely due to a larger water content in the frozen mix, consistent with the observation of brine later in the diurnal cycle when the eutectic temperature is exceeded. (b) Brine forms at 05:30, after the temperature exceeds the eutectic value. (c) Brine on top of frozen brine at 07:00. (d) Brine only at 11:45. (e) Start of crust formation at 14:30……..69

5.14 Raman spectra in the O-H stretching band throughout the diurnal cycle shown in Fig. 5.4 (fourth experiment). Gaussian components of each spectrum are shown in Table 5.4…71

5.15 As in Fig. 5.14, but for the perchlorate vibration band. The perchlorate peak is at 936 cm^{-1} for both, the mix of water ice and salt and brine, similar to the peak shown in Fig. 5.12……..71

5.16 Images of the sample (a-e) and of a spheroid of the same composition (f-j), similar to those observed on the Phoenix strut, color-coded to represent the times when the Raman spectra were taken (Figs. 5.14 and 5.15). (a) Frozen mix of water ice and perchlorate salt at 01:15. Translucent areas in the sample compared to the completely whitish frozen brine in Fig. 5.10d are likely because of the larger water content of the frozen mix. (b) Onset of liquefaction at 01:35 after the temperature exceeds the eutectic value. (c) Brine and ice at 04:25, with the Raman signal indicating only the presence of ice (Table 5.4). (d-e) Only brine remains between 12:35 and 17:15. (f) Frozen spheroid at 01:15. (g) No clear sign of melting is observed at 01:35, after the eutectic temperature is exceeded. (h) Melting of the spheroid is indicated by bubble formation and movement. (i) Crust formation on the spheroid at 12:35. This indicates higher evaporation on the spheroid than on the sample holder likely because of the spheroid's larger surface-area-to-volume ratio. (j) Dry spheroid at 17:15……72

6.1 (Top) The TECP is mounted on the end of the 2.3 m long Robotic Arm. The TECP is 119 mm in length and its needles are 15 mm long. (Bottom) Close-up of the TECP, with the relative humidity sensor indicated by an arrow and with the function of each needle identified. From *Zent et al.* [2010]……..78

6.2 The Michigan Mars Environmental Chamber is capable of simulating Martian polar conditions, covering the environmental conditions found at the Phoenix landing site that were not tested during preflight tests. The TECP Engineering Model is sitting on top of thermal plate to allow thermal contact……80

6.3 The TECP preflight calibration (red) only partially overlaps the relative humidity measurements at the Phoenix landing site (gray). We use the output of a TECP engineering unit (blue) at the same environmental conditions as the preflight calibration and at additional values known to have occurred at the landing site (green) to translate the in situ measurements into values the engineering unit would have recorded (black). We then cover this entire range of temperature and relative humidity conditions to calibrate the engineering unit and find a recalibration for the flight unit……82

6.4 Water vapor pressure measured by the TECP for the entire range of board temperatures and color coded by sol number using the new calibration function…….85

6.5 Recalibrated relative humidity data at the sensor throughout the diurnal cycle at the Phoenix landing site with color coded sol number. The occurrence of saturation (RH > 100%) around sol 90 coincides with the observation of ground fog at the landing site…86

6.6 Error bars (gray) on the water vapor pressure data (red) shown in Fig. 6.4 based on our recalibration method. For illustrative purposes only 1% of all data points are shown here…….87

6.7 Orbital and in-situ estimates of water vapor pressure at the Phoenix landing site based on other instruments for comparison. The TECP data shown here are based on the 2009 calibration. The water vapor pressure values obtained from our recalibration are in the range of the values shown here. From *Tamppari et al.* [2010]……88

6.8 Comparison of our new calibration with previous calibration results. While our data is similar to the two previous calibrations at nighttime, it is an order of magnitude larger during daytime, where it is more similar to the original calibration……89

8.1 Stability diagram as in Fig. 1.2, with superimposed values of: simultaneous RH and ground temperature for the first 1772 sols of the MSL mission (maroon), simultaneous RH and air temperature at 2 m measured by the PHX/MET instrument for the entire duration (151 sols) of the PHX mission (sky-blue), simulated ground (green) and subsurface (purple) temperature on sol 19 of the PHX mission. Results from previous laboratory experiments of deliquescence of Ca, Mg and Na perchlorates are shown in colored circles. RH values shown here have been calculated with respect to liquid, in accordance with the dashed lines representing phase change……..96

8.2 Three- and two-dimensional sketches of a ternary phase diagram. (Left) Liquidus surfaces colored in gray, with composition plotted along the sides of the triangular base, and temperature plotted vertically. Isotherms are shown as contours on the gray liquidus surfaces. The binary eutectics are represented by the boundary curves between the surfaces that the two phases on each side of the curve crystalizes. (Right) Crystallization path of mixture of composition X, showing that the solids resulting from the crystallization of mixture X (bold path) contains components A, B and C……..98

8.3 Overview of the Mars 2020 rover instruments including MEDA. Image credit: NASA…….99

A.1 Spectra of sodium perchlorate in contact with ice. Experiments similar to those for $Ca(ClO_4)_2$ were performed for $NaClO_4$ in contact with ice while the temperature of the sample was raised above its eutectic temperature $T_e \approx$ -37 ºC at the typical rate occurring diurnally in the shallow Martian subsurface. When the crystalline salt (here mostly anhydrous $NaClO_4$ but with small peaks in the O-H region indicating partial hydration) hydrates or forms a liquid solution, the 954 cm^{-1} peak in the Raman spectrum shifts toward 937 cm^{-1}. The appearance of the typical O-H vibrational band for liquid water indicates the occurrence of a liquid solution within about 1 hour of the start of the experiment, when the salt is in contact with ice at environmental conditions of Mars' polar region……...102

A.2 Decomposed OH vibrational spectrum of $NaClO_4$ in contact with ice at -18 ºC. The O-H vibrational spectrum at -18 ºC shown in Figure A.1 contain four Gaussians components at 3230, 3437, 3559, and 3610 cm^{-1} with FWHM > 50 cm^{-1} indicating the presence of liquid water. $\bar{R}^2 \approx 1.000$……...102

A.3 Simulated ground temperature (red curve), simulated air temperature at 2 m above the ground (black curve), air temperature measured at 2 m by MET (gray asterisks) and simulated frost point temperature above the surface (blue curve) on sol 19……..108

B.1 Simplified CAD drawing of the external Michigan Mars Environmental Chamber structure. The updated version is doubled in length, consisting of two of the tubes shown here. Dimensions are in inches……..109

B.2 Simplified CAD drawing of the thermal plate setup inside the Michigan Mars Environmental Chamber, showing a sample holder, the plate's insulation from the chamber walls, its cooling loops for the LN_2 and the cartridge heaters at the bottom of the thermal plate. Dimensions are in inches……..110

LIST OF APPENDICES

A.1 Supplementary Material for Chapter IV 101

A.2 Supplementary Material for Chapter V 103

A.2.1 The Michigan Mars Environmental Chamber 103

A.2.2 Data Analysis 103

A.2.3 Environmental Conditions at the Phoenix Landing Site on Sol 19 104

B. Design Drawings of the Michigan Mars Environmental Chamber 109

LIST OF UNCOMMON SYMBOLS AND ACRONYMS

AU	Astronomical unit, 149 597 870 700 m
$Ca(ClO_4)_2$	Calcium perchlorate
cm^{-1}	Wavenumber
CRISM	Compact Reconnaissance Imaging Spectrometer for Mars
DAN	Dynamic Albedo Neutrons
DNRH	Digital number relative humidity
e	Water vapor partial pressure
e_s	Saturation water vapor partial pressure
eu	Engineering unit
fu	Flight unit
FWHM	Full width at half maximum
GUI	Guided User Interface
GSFC	Goddard Space Flight Center
H	Scale height of the atmosphere
HiRISE	High Resolution Imaging Science Experiment
JPL	Jet Propulsion Laboratory
LIDAR	Light Detection and Ranging
LN_2	Liquid Nitrogen
LTST	Local true solar time

MAWD	Mars Atmospheric Water Detector
MECA	Microscopy, Electrochemistry and Conductivity Analyzer
MEDA	Mars Environmental Dynamics Analyzer
MET	Meteorological Station
$Mg(ClO_4)_2$	Magnesium perchlorate
MMEC	Michigan Mars Environmental Chamber
MOLA	Mars Orbiter Laser Altimeter
MRO	Mars Reconnaissance Orbiter
MSL	Mars Science Laboratory
MY	Martian year, starting from the northern Spring equinox of April 11, 1955
$NaClO_4$	Sodium perchlorate
OMEGA	Observatoire pour la Minéralogie, l'Eau, les Glaces et l'Activité, Visible and Infrared Mineralogical Mapping Spectrometer
PBL	Planetary Boundary Layer
PDS	Planetary Data System
PID	Proportional-integral-differential
PHX	Phoenix lander
ppm	Parts per million
pr-μm	Precipitable micrometer
PWC	Precipitable water content
q	Specific humidity
R^2	Coefficient of determination
RA	Robotic Arm

RH	Relative humidity
RSL	Recurring Slope Lineae
RTD	Resistance temperature detector
R_v	Specific gas constant of water vapor
SHERLOC	Scanning Habitable Environments with Raman and Luminescence for Organics and Chemicals
Sol	Martian solar day
TECP	Thermal and Electrical Conductivity Probe
T_b	Board temperature
T_e	Eutectic temperature
TES	Thermal Emission Spectrometer
T_f	Frost point temperature
T_g	Ground temperature
$.xH_2O$	x-hydration state of a salt
β	Surface wetness

ABSTRACT

Liquid water is essential for life on Earth. To search for conditions that could support life on Mars, we need to understand if liquid water can be present, even temporarily, at its surface and shallow subsurface. Brine is a highly concentrated saline solution that can exist in the liquid state at temperatures well below the freezing point of pure water, such as those on Mars.

Water ice and perchlorate salts capable of melting this ice and producing liquid solutions have been discovered in the Martian regolith from polar to equatorial regions. In addition to melting of ice, perchlorate salts may also form a brine on Mars by deliquescence, absorbing water vapor when the relative humidity is above a certain threshold. Evidence for brine at the surface and in the shallow subsurface of Mars has been reported in the last few years, such as in its polar region at the Phoenix landing site and at mid- and low-latitudes at surface features called Recurring Slope Lineae and Slope Streaks.

We have designed and developed the Michigan Mars Environmental Chamber to perform experiments at Martian conditions. We study brine formation and assess whether deliquescence and/or melting are consistent its formation, and to calibrate a variety of in-situ sensors at Martian conditions. Our chamber is equipped with a Raman spectrometer, which we use to provide reference spectra of various mixing states of liquid water, ice and perchlorate salt during brine formation. We show that perchlorate brines can be identified by analyzing the decomposed Raman spectra of the investigated samples. This serves as an important reference for future in-situ Raman spectrometers on Mars and can aid in the detection of brine formation.

We find that when water vapor is the only source of water, bulk deliquescence of perchlorates is not rapid enough to occur during the short periods of the day when the environmental conditions are favorable. However, when the salts are in contact with water ice, liquid brine forms more quickly, indicating that aqueous solutions could form temporarily where salts and ice coexist in the Martian regolith.

We further simulate full diurnal cycles of temperature and atmospheric water vapor at the Phoenix landing site of mixtures of ice and salt such as encountered at the Phoenix landing site and show that brine can form and stay liquid for most of the diurnal cycle. This is predicted to occur seasonally in areas of the polar region where the temperature exceeds the eutectic value and frost or snow is deposited on saline soils, or where water ice and salts coexist in the shallow subsurface.

Finally, we show results of the recalibration of the relative humidity sensor of the Phoenix lander. We have use a spare engineering unit to recalibrate the sensor in the full range of Phoenix landing site conditions. This provides processed relative humidity data at Martian polar conditions to enhance our understanding of the hydrological cycle at the Phoenix landing site, which is important for potential brine formation.

We conclude that deliquescence is unlikely to form temporarily habitable conditions on Mars. The most likely places to do so are regions where subsurface water ice and perchlorate salts coexists. This is most likely at the north and south polar region and parts of the mid- to low-latitudes bearing water ice.

CHAPTER I

Introduction

1.1 An Overview of Mars

1.1.1 Mars in the Solar System

Mars is the fourth planet from our sun and the outermost terrestrial planet in our solar system. It has a reddish appearance even to the naked eye due to the high iron-oxide content of the topmost surface layer. It also has two small and irregular moons, Phobos and Deimos. In many regards, Mars is the planet most similar to Earth. It has around half the diameter of Earth and Venus, and 1.4 times that of Mercury, making it the second smallest planet. Gravity on Mars is 38% of Earth's. Mars' orbit around the Sun is approximately two Earth years long, while its day (called sol) is just 37 minutes longer than Earth's. Mars has a similar axial tilt to Earth resulting in a similar impact on the seasons, but while Earth's astronomical seasons are rather similar in length, varying from 89 to 94 days, Mars' seasons differ more, from 143 sols of northern fall to 193 sols of northern spring. This is because Mars has a much more eccentric orbit than Earth, with its perihelion in northern fall, resulting in stronger seasonal variations in the southern hemisphere. Mars has two polar caps, largely made of water ice, which strongly vary in size seasonally, due to

the deposition and sublimation of CO_2 ice with the seasons [*Read and Lewis*, 2004]. Table 1.1 provides some basic planetary parameters for Mars and Earth in comparison [*Williams*, 2016].

Parameter	**Mars**	**Earth**
Mean radius	3390 km	6371 km
Surface gravity	0.378 g	1 g
Sidereal day length	24 h 37 m 22 s	23 h 56 m 4 s
Orbital period	669 sols	356 days
Axial tilt	25.2º	23.4º
Semi-major axis	1.5 AU	1 AU
Eccentricity	0.094	0.017
Moons	2	1
Solar constant	586 W/m^2	1361 W/m^2
Surface pressure	6-10 hPa	1013 hPa
Surface temperature	130-308 K	184-330 K

Table 1.1: Basic planetary parameters of Mars.

1.1.2 The Martian Atmosphere

Most of Mars' atmosphere has been lost after the planet lost its magnetosphere. This very slow atmospheric loss process continues to this day [*Jakosky and Phillips*, 2001]. The remaining atmosphere consists primarily of CO_2, as shown in Table 1.2 [*Mahaffy et al.*, 2013]. It is therefore much thinner than on Earth, with the surface pressure about two orders of magnitude lower than on Earth. The scale height on the other hand is 11.1 km, larger than the 8.5 km on Earth, due to the low gravity [*Williams*, 2016]. The mean surface pressure is about 6 hPa, but varies greatly with elevation and season. The seasonal variation occurs because of the poles being in total darkness in winter with temperatures reaching values low enough for 25% of the atmospheric CO_2 to deposit around the pole as dry ice, driving the seasonal pressure cycle all over Mars [*Read and Lewis*, 2004].

The solar constant is less than half of the value on Earth resulting in lower temperatures. The thin atmosphere and low thermal inertia of the surface result in a large surface temperature range from 130 K in winter at the polar caps (below the freezing point of CO_2) to 308 K in summer at the equator.

Gas	**Mars**	**Earth**
CO_2	95.97%	0.04%
Ar	1.93%	0.93%
N_2	1.89%	78.08%
O_2	0.15%	20.95%
CO	0.06%	$<10^{-4}$%

Table 1.2: Comparison of the abundance of Martian atmospheric constituents with those of Earth.

Water is rare on Mars. Liquid H_2O is not stable at the atmospheric surface conditions due to the low pressure, water vapor pressure and temperature. The water vapor in the entire atmospheric column is on the order of 1 pr-μm, four orders of magnitude lower than on Earth. Most of the Martian water is confined to the subsurface and the high latitudes as ice. In addition, water ice exists as snow, ice fog, frost and water ice clouds [*Read and Lewis,* 2004].

The Martian atmosphere contains large amounts of dust, giving it its orange hue. The atmospheric dust particles have an average diameter of 1.5 μm. Dust storms are a common occurrence ranging in size and duration from local minutes-long dust devils to global storms shrouding the entire planet for months [*Read and Lewis,* 2004].

1.1.3 The Martian Surface

The Martian surface is primarily composed of basalt, a rock of volcanic origin. The top layer of the soil is made up of fine iron oxide dust, giving Mars its distinctive orange to red color. The majority of surface features were formed by impacts during the Late Heavy Bombardment

period. Other features were formed during a time when Mars was believed to be warmer and wetter than today, including geological features formed by extensive flooding [*Bell*, 2008]. Martian volcanoes such as the Tharsis volcanoes and Olympus Mons are the most visible features of Mars' active tectonic past. Olympus Mons is the tallest planetary mountain in our solar system with a height of 21-26 km. There is a strong dichotomy in elevation between the southern and the northern hemisphere of Mars, clearly visible in Figure 1.1, possibly due to a large impact event. On average, the elevation in the northern hemisphere is ~5 km lower than in the southern hemisphere. This dichotomy affects local and global wind patterns and cloud formation.

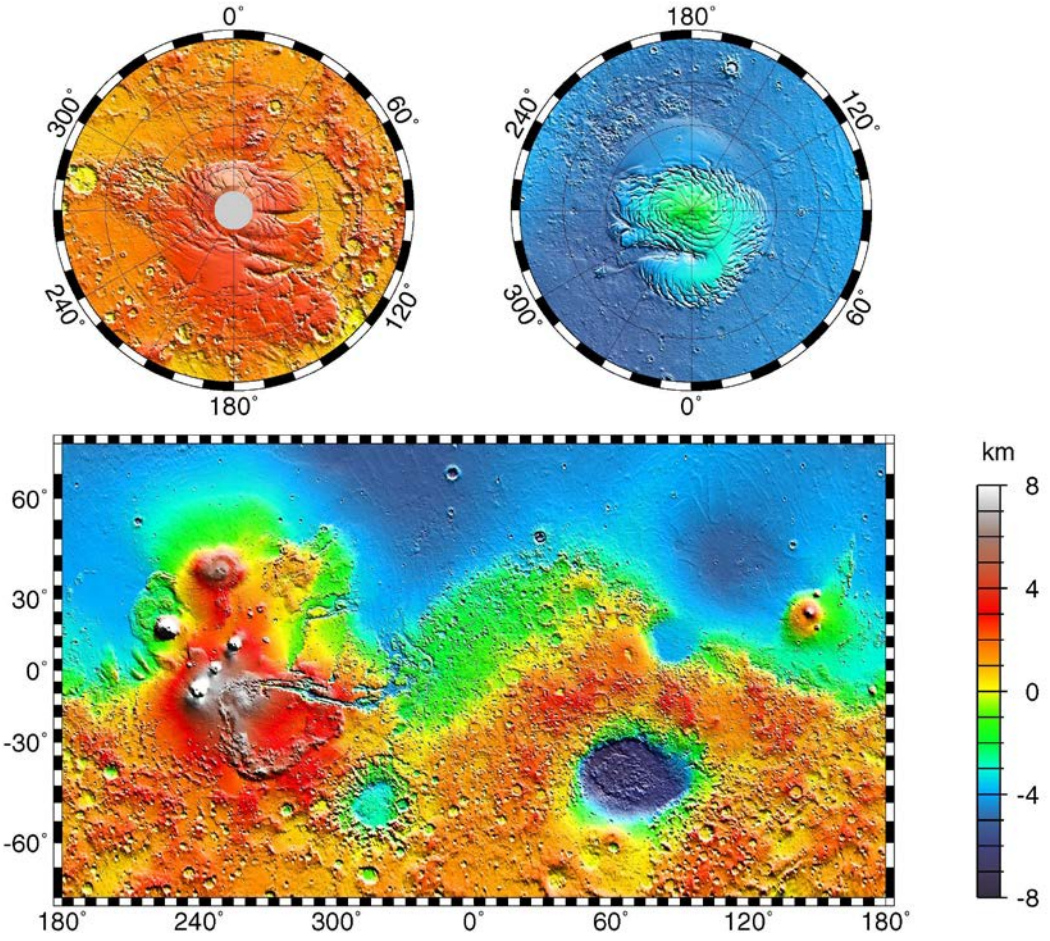

Figure 1.1: Topography of the Martian surface based on Mars Orbiter Laser Altimeter (MOLA) measurements, showing the strong north/south dichotomy in elevation. Image credit: NASA/JPL/GSFC.

1.2 Past, Current and Future Mars Exploration

> *"That planet has a considerable but moderate atmosphere. So that the inhabitants probably enjoy a situation in many respects similar to ours."*
>
> *- William Frederick Herschel on Mars, 1784*

This section gives a brief overview of the history of Martian observation and exploration. More details can be found in *Sheehan* [1996] and *Taylor* [2010].

Mars has fascinated astronomers since antiquity, with observations dating back to Egypt in the second millennium BCE. Later, due to its red color the Babylonians, Greeks and Romans associated it with the god of war. Plato, Aristotle and later Ptolemy placed it in the Greco-Roman geocentric view of the universe. This view remained largely unchanged until 1543, when Nicolaus Copernicus published his heliocentric model with the planets orbiting the sun in circles. Because of the inability to fit observations made by Tycho Brahe into this system, Johannes Kepler proposed the system of planets orbiting in ellipses with the sun at one focal point in his laws of planetary motion published between 1615 and 1621.

Better visual observations began with the development of telescopes in the first decade of the 17th century. Galileo Galilei made the first telescopic observations of Mars in 1610. In 1659 Christiaan Huygens was the first person to record surface features, now known as Syrtis Major Planum, followed by Giovanni Domenico Cassini observing the northern polar cap in 1666 and Huygens the southern equivalent in 1672. That same year Cassini estimated the distance between Earth and Mars to within 10% error. From 1777 to 1784 Sir William Herschel observed the Martian polar caps, based on their seasonal changes suggesting that they were made of ice. In 1784 he described for the first time the Martian atmosphere with the introductory statement to this section.

Using improved telescopes, astronomers Johann Mädler and Wilhelm Beer observed Mars from 1830 to 1840 to draw the first maps of the surface.

In 1877 Asaph Hall discovered the two Martian moons, naming them Phobos and Deimos. That same year Giovanni Schiaparelli saw long straight lines across the surface, calling them *canali* (mistranslated to *canals* instead of the correct *channels*). This influenced astronomers Percival Lowell and Camarille Flammarion in 1892 and 1894 to assume the *canali* were built by an intelligent race, inspiring the public, while contemporary colleagues such as Edward Barnard, Eugene Antoniadi, Alfred Wallace and George Hale correctly suggested they were neither straight nor artificial, but optical illusions.

Investigating the atmosphere in 1908, based on what would now be called modeling, Lowell estimated a Martian surface pressure of 87 hPa based on Mars' low gravity. This value was refined to 66 hPa in 1925 by Donald Menzel and again in 1929 by Bernard Lyot to 24 hPa. Throughout the 1930s spectroscopic observations of the Martian atmosphere by Walter Adams and Theodore Dunham showed no evidence of water. In 1947 Gerard Kuiper detected CO_2 in the spectra suggesting 2 hPa of partial pressure. More unsuccessful attempts at detecting water spectroscopically were performed between 1947 and 1962 by Kuiper, Kiess, Korliss, Spinrad and Richardson, until in 1963 Spinrad, Munch and Kaplan finally detected 5-10 pr-μm of water. They suggested an atmospheric pressure of <25 hPa, still assuming a mostly nitrogen atmosphere with 4 hPa of CO_2. A value of 5-6 hPa on average was inferred from observations and modeling by Young in 1971, already well into the spacecraft era.

The Mars spacecraft age began in 1960, just three years after Sputnik 1 with two Soviet launch failures aimed at Martian flybys. This tragic start continued in the next launch window in 1962 with two further launch failures and the successful launch of Mars 1 which was lost en route

to Mars. In the US the same year saw the start of the Mariner project with the intention to launch within two years. On time in 1964, Mariner 3 failed en route to Mars similar to the Soviet Zond 2 around the same time. The second American probe Mariner 4, launched in the same month, was the first successful Mars mission. It conducted a flyby, obtaining the first images of the surface and finding no magnetic field.

In 1969 Mariner 6 and 7 successfully acquired higher quality images of 10% of the surface, confirmed the surface pressure of 6.5 hPa and measured a polar cap temperature of -123 ºC, implying frozen CO_2. The same year a Soviet orbiter had a launch failure. In 1971, after the failure of Mariner 8, Mariner 9 were the first to enter Mars orbit, arriving during a global dust storm. Nonetheless, it mapped 70% of the planet and suggested a water-rich history based on observed landforms leading to the search for life. In 1971, after an unnamed Soviet mission failure, Mars 2 and 3, each being a Soviet orbiter/lander/rover combination, reached Mars' orbit successfully. The orbiters photographed the surface and measured water and dust in the atmosphere, but the landers failed with Mars 2 crashing and Mars 3 achieving the first soft landing on Mars but arriving during the same global dust storm that Mariner 9 encountered and failing after 14.5 seconds on the surface, without recording any scientific measurements. The next four Soviet missions during the 1973 launch window were Mars 4-7, two orbiters and two landers (in that order). Mars 4 and 7 missed the planet; Mars 5 operated for 22 days in orbit and Mars 6 sent no signals after parachute deployment during the descent phase.

The next milestone for NASA were the 1975 Viking 1 and 2 orbiter/lander combinations launched to search for life. The landers landed in 1976 with a 90 day design lifetime and transmitted data until 1982/1980. They carried a variety of scientific instruments, including a meteorology boom, color imagers, the MAWD spectrometer to measure the atmospheric water

vapor content throughout the seasons, an infrared radiometer for surface temperature measurements and biology experiments to search for microbial life on the surface. The search for life produced negative results.

The Viking missions were a huge scientific success in spite of finding no sign for life. A 13 year hiatus from Mars missions followed until 1988 when the Phobos 1 and 2 missions were launched by the USSR to orbit Mars and land on Phobos. Phobos 1 lost communications en route. Phobos 2 was successfully inserted into Martian orbit, but lost contact just before the start of the Phobos lander activities.

In the 90s NASA's Mars exploration program restarted. In 1992 Mars Observer lost communications en route. In 1996 Mars Global Surveyor was launched to study surface features in high resolution, find landing sites, and measure surface elevation accurately. It operated successfully until 2006. In the same launch window Mars Pathfinder and Sojourner, a lander/rover combination was launched. It was an inexpensive mission, part of NASA's Faster Better Cheaper program, with the first successful Mars rover and also including a weather station that detected dust devils from the surface for the first time.

The late 90s were a crisis for Mars research. In 1998 Nozomi, a Japanese orbiter, failed to enter orbit. That same year NASA's Mars Climate Orbiter went off track and burned up in Mars' atmosphere due to an infamous imperial to metric unit conversion error. One year later, Mars Polar Lander and the Deep Space 2 penetrators failed to land on the surface.

The 2000s were highly successful. In 2001 Mars Odyssey was launched. The orbiter detected large amounts of subsurface hydrogen indicating water ice. Mars Odyssey is the longest lasting spacecraft in Mars orbit to date with plans to operate it until at least 2025. 2003 saw the first ESA mission to Mars: Mars Express with the lander Beagle 2. The orbiter has been highly

successful and is still operating but the lander lost contact during landing. The same year saw the arrival of the Spirit and Opportunity rovers. They found clear geological signs of past water activity and to date Opportunity is still operating. Mars Reconnaissance Orbiter launched in 2005, carrying a large optics camera for high resolution images and operating as a relay for surface operations. MRO is also still operating. In 2007 Phoenix was launched. It is the first lander to land in the polar region to investigate water ice in the shallow subsurface for 130 days. It observed water ice and likely frozen brine in the subsurface and photographed spherules (likely briny water) on its struts that appeared to be liquid temporarily.

This decade continues with a more international line-up of Mars missions. In 2011 Fobos-Grunt: A new Russian Phobos sample return mission stranded in LEO. More successfully in the same launch window, Mars Science Laboratory (MSL), the largest rover to date arrived on Mars, investigating Mars' climate, geology and whether past conditions could have supported life. After close to 2000 sols at time of writing it is still operational. 2013 saw the entry of India as the fourth international player to successfully send spacecraft to Mars. Its Mars Orbiter Mission (Mangalyaan) is a technology demonstrator with secondary science objectives. The same year NASA's Mars Atmosphere and Volatile Evolution Mission launched to investigate how Mars' atmosphere and water have been lost over time. Finally the last mission to date was ESA's 2016 ExoMars Trace Gas Orbiter and Schiaparelli lander sent for atmospheric mapping and to study methane and other trace gases. Schiaparelli's signal was lost during landing.

Multiple missions are planned for the near-future. In 2018, within a few months of this writing the InSight lander, similar in layout to Phoenix, will launch to study the Martian subsurface. Four big missions are planned to launch in 2020. Mars 2020 is NASA's successor to MSL, preparing for sample return missions and future human exploration. ESA will follow with

the ExoMars 2020 lander and rover to search for the existence of past life. The United Arab Emirates plan to launch its Hope probe to study the atmosphere and climate. Also, China plans to send its Mars Global Remote Sensing Orbiter and Small Rover. In 2022 India will follow up on its success with Mangalyaan 2 and Japan is planning a sample return from Phobos in 2024 with their Martian Moons Exploration mission.

1.3 Water on Mars: The Motivation for this Work

The presence of liquid water is the most important prerequisite for life as we know it on Earth. To search for life, or at least conditions that could support life as we know it, on other planetary bodies, we need to understand where liquid water can exist.

Compared to Earth, Mars holds a much smaller amount of H_2O on the ground and in the atmosphere. By far, most of the Martian water exists as ice in the polar caps and in the shallow subsurface in high latitudes. A small amount of H_2O is held in the atmosphere, on the order of 1 to 10 pr-μm. The water vapor pressure at the triple point of water (~600 Pa) is below the present day atmospheric pressure in the lower regions of Mars, such as the Phoenix and the Curiosity landing sites (~700-950 Pa), but the low surface temperature (~180-285 K), in combination with the extremely low water vapor pressure (on the maximum order of ~1Pa), inhibits the formation and persistence of pure liquid water [*Haberle et al.*, 2001; *Zent et al.*, 2010; *Harri, et al.*, 2014]. It is thermodynamically unstable.

However, perchlorate salts were discovered on Mars in the polar and equatorial regions suggesting they are distributed globally [*Hecht et al.*, 2009; *Glavin et al.*, 2013; *Ming et al.*, 2014]. Furthermore, sulfates and chlorides were discovered at low latitudes, at Meridiani Planum and Gusev crater [*Clark et al.*, 2005; *Campbell et al.*, 2008; *Schmidt et al.*, 2008], while chlorides were

also discovered from low to midlatitudes in the southern hemisphere [*Osterloo et al.*, 2008]. These salts can depress the freezing point of water below the Martian surface temperature [*Farmer*, 1976; *Clark*, 1978; *Brass*, 1980; *Clark and Hart*, 1981; *Moore and Bullock*, 1999; *Haberle et al.*, 2001; *Rao et al.*, 2005; *Bryson et al.*, 2008; *Chevrier and Altheide*, 2008; *Renno et al.*, 2009]. Figure 1.2 shows the stability diagram of three perchlorate salts as an example. They may have the capability to form temporary highly-saline liquid solutions when in contact with water, either from water vapor in the near-surface atmosphere (deliquescence) [*Renno et al.*, 2009; *Zorzano et al.*, 2009; *Davila et al.*, 2010; *Gough et al.*, 2011; *Nuding et al.*, 2015; *Nikolakakos and Whiteway*, 2015], or from water ice (melting) [*Fairén et al.*, 2009; *Cull et al.*, 2010b; *Chevrier et al.*, 2012; *Fischer et al.*, 2014; *Fischer et al.*, 2016]. Water ice has been detected in the shallow subsurface from mid-latitude to polar regions of Mars, both, remotely using satellite measurements and in-situ [*Boynton et al.*, 2002; *Feldman et al.*, 2002; *Mitrofanov et al.*, 2002; *Byrne et al.*, 2009; *Smith et al.*, 2009; *Wilson et al.*, 2017; *Dundas et al.*, 2018].

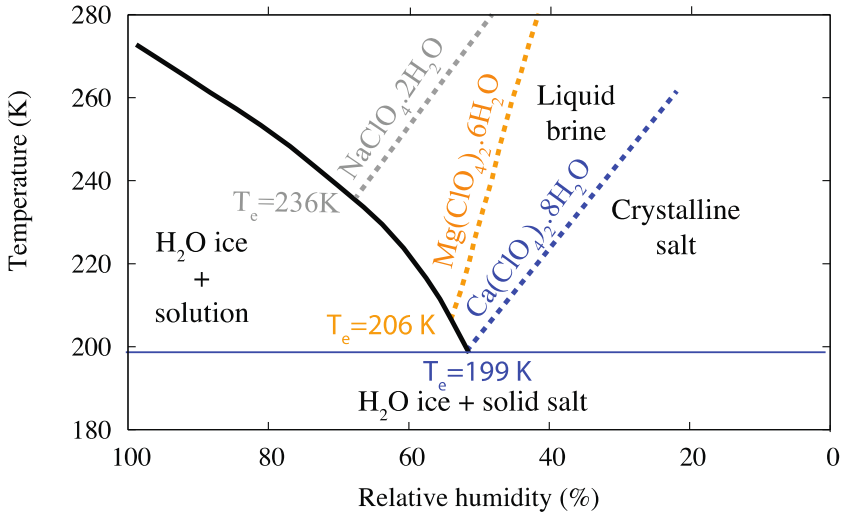

Figure 1.2: Stability diagram of $Ca(ClO_4)_2$, $Mg(ClO_4)_2$ and $NaClO_4$ salts. The colored dashed lines represent the deliquescence relative humidity at which the various salts form aqueous solutions. The eutectic temperatures of $Ca(ClO_4)_2$, $Mg(ClO_4)_2$ and $NaClO_4$ are shown in their respective colors.

There is spectroscopic, thermodynamic and visual evidence for temporarily liquid brine at the surface and in the shallow subsurface of Mars. At the Phoenix landing site, visual and thermodynamic evidence for brine formation was found both in disturbed and in undisturbed areas [*Renno et al.*, 2009]. Spheroids observed on a strut of the Phoenix lander and the "soft ice" found in one of the trenches dug by Phoenix (Fig. 1.3) were likely frozen brine that had been formed previously by perchlorates on icy soil. Alternatively, the spheroids could be either ice particles nucleated by the dark material splashed on the strut, or grown by deliquescence on contamination products of the retro-thruster engines [*Renno et al.*, 2009].

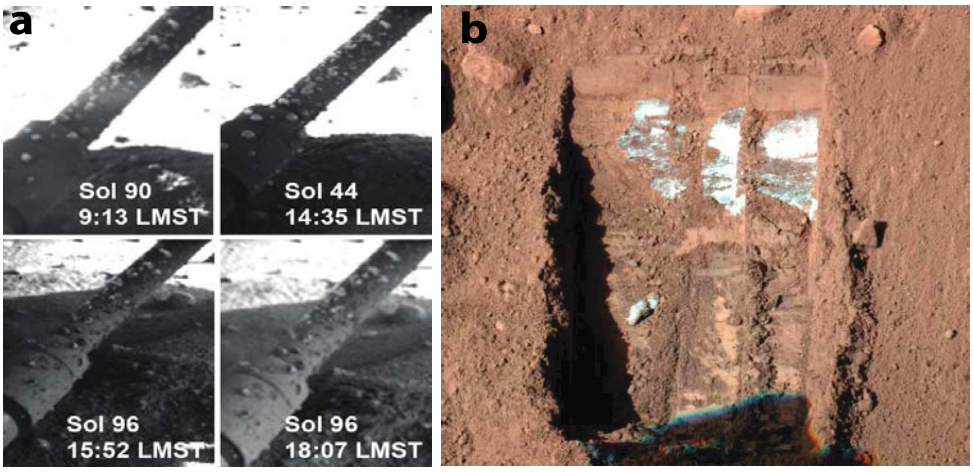

Figure 1.3: (a) Spheroids on the strut of the PHX lander at various sols and times. The spheroids are largest and most spherical at around midafternoon on Sol 44, probably because the RH and temperature have reached peak values and the spheroids are liquid brine, grown by deliquescence [*Renno et al.*, 2009]. (b) Sol 19 Surface Stereo Imager image of the first trench dug by the Phoenix Robotic Arm. Ice was exposed and removed with little effort, suggesting that it was either saline ice or layered ice formed in the presence of brines. From *Renno et al.* [2009].

At low and mid-latitudes, landforms called Recurring Slope Lineae (RSL) (Fig. 1.4) have been observed. They are 0.5-5 m wide, hundreds of meters long, low-albedo features that form in late southern spring and summer and vanish during the colder seasons [*McEwen et al.*, 2011]. RSL have been hypothesized to form as a result of contemporary liquid water activity. The spectral

identification of perchlorate in association with RSL could suggest brine or hydrated salts [*Ojha et al.*, 2015]. The source of liquid water in RSL is not well understood, but it could include surface and subsurface water ice, atmospheric water vapor through deliquescence and discharge of local aquifers. Alternatively, recent analyses suggest that RSL may instead be dry granular flow features because their terminal slopes match the stopping angle for granular flows of cohesionless sand [*Dundas et al.*, 2017].

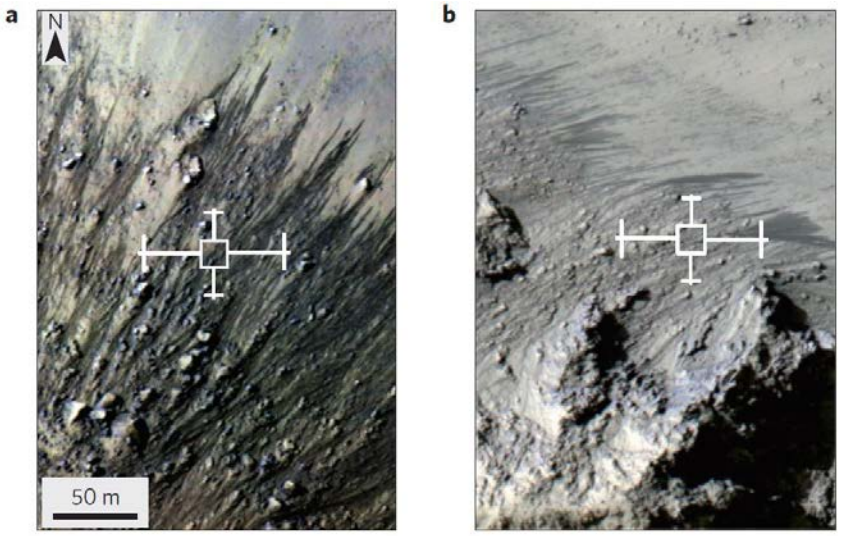

Figure 1.4: HiRISE images showing RSL activity in the central peaks of Horowitz crater. From *Ohja et al.* [2015].

Slope Streaks are distinct albedo features at low latitudes up to ~1000 m long and as wide as ~100 m (Fig. 1.5) that form with no seasonal preference [*Kreslavsky and Head*, 2009; *King et al.*, 2010], and that fade within timescales as long as decades [*Martínez and Renno*, 2013]. Similarly to RSL, Slope Streaks have been hypothesized to form as a result of liquid water activity. Even though the most widely accepted explanations for their formation involve dry mechanisms, such as dust avalanches following oversteepening of air fall deposits [*Sullivan et al.*, 2001], wet mechanisms proposed for their formation include ground water discharge [*Ferris et al.*, 2002] and

percolation of chloride and perchlorate brine downward to depths of decimeters [*Kreslavsky and Head*, 2009].

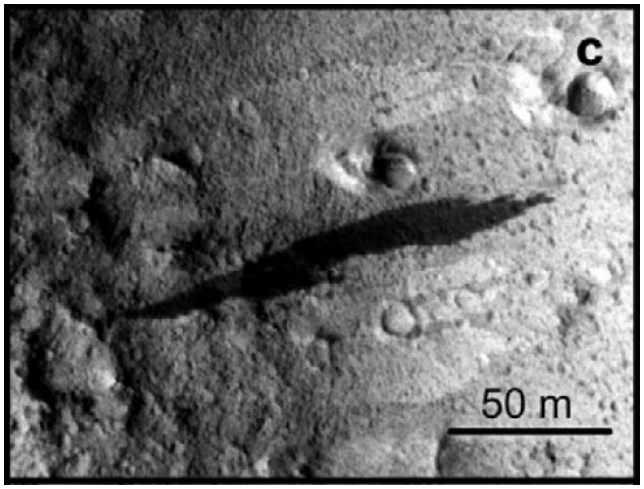

Figure 1.5: An example of a slope streak on a hill in Cerberus Tholi (8°N, 163°E). From *Kreslavsky and Head* [2009].

The possibility of brine formation on Mars is key to the search for life. On Earth the known limits of life are ever-expanding. It was shown in the last two decades that a diverse array of terrestrial microorganisms thrives in brines; in subsurface saline aquifers, deep-sea brine pools, ancient subglacial brine reservoirs, and Dead Sea brine with more than 20% salt content [*Green and Lyons*, 2009; *Mikucki et al.*, 2009; *Joye et al.*, 2009; *Biddanda et al.*, 2009; *Thomas and Dieckmann*, 2002; *Boetius and Joye*, 2009]. The discovery of sulfur and iron cycling microbial communities in the subglacial brine that episodically drains from Taylor Glacier in Antarctica's Dry Valleys [*Mikucki et al.*, 2009], as well as the discovery of microbes in brine channels and brine inclusions in sea ice [*Junge et al.*, 2001] are particularly relevant to the understanding of the habitability of Mars.

To experimentally investigate possible brine formation at Martian conditions, the environmental conditions at the Martian surface and in the shallow subsurface have to be

understood. Then, those conditions can be recreated in a laboratory setting. In Chapter II, I describe the design of the Michigan Mars Environmental Chamber (MMEC) to accomplish this goal. Chapter III then describes techniques that I developed with the help of my advisors to detect and analyze brine formation using Raman spectroscopy. Next, Chapter IV describes our investigation into brine formation on Mars by deliquescence and melting of water ice. In Chapter V I describe our investigation into brine formation and persistence throughout simulated diurnal cycles at the Phoenix landing site in the north polar region of Mars. Chapter VI covers my work on improving our understanding of the environmental conditions that could lead to brine formation by improving the calibration of the relative humidity sensor on the Phoenix lander. In Chapter VII I will conclude my findings throughout these studies. Finally, I will give an outlook into future efforts in Chapter VIII.

CHAPTER II

The Michigan Mars Environmental Chamber

2.1 Overview

We have designed and developed the Michigan Mars Environmental Chamber (MMEC) as a laboratory apparatus for experimental research into the stability of liquid water on Mars. We use the MMEC to accurately simulate Martian environmental conditions, to study the formation, stability and persistence of various salt brines on the Martian surface and in the subsurface, and to test and calibrate a variety of in-situ sensors pre- or post-flight. The structure of the MMEC was designed by Harvey Elliott, a senior PhD student. Harvey and I designed, selected and assembled the control systems, interfaces, feedthroughs, tubing and cabling. I performed the calibrations of the MMEC's temperature, pressure and relative humidity control systems and conducted all experiments presented in this dissertation.

Figure 2.1 shows a diagram of the chamber layout, including its pressure, temperature and relative humidity control systems. The MMEC can recreate the entire range of Martian surface conditions in pressure, temperature and relative humidity from polar to equatorial latitudes throughout the entire diurnal and seasonal cycle. Pressure and temperature are automatically

controlled through a custom-made guided user interface (GUI), based on the chosen settings. The relative humidity is displayed and stored using the same interface, but controlled manually. The following sections will describe the pressure, temperature and relative humidity control systems in detail, and further describe a variety of additional instruments that have been successfully used in combination with the chamber. The following chapters will give details about a number of research applications that we have used the chamber for. Simplified CAD drawings of the chamber structure are shown in the Appendix (Figs. B.1 and B.2).

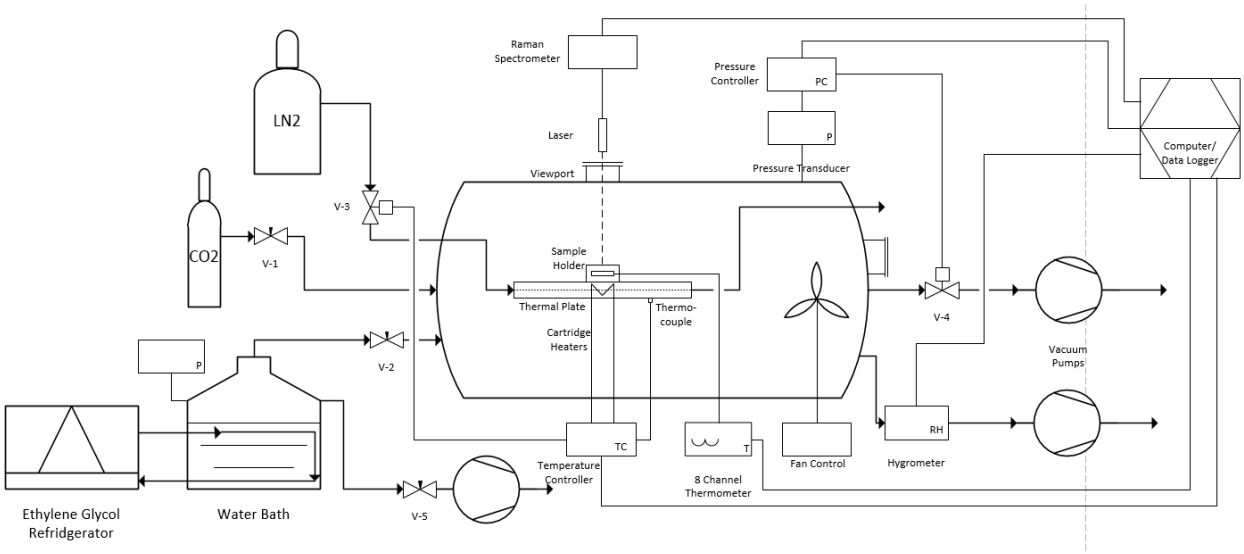

Figure 2.1: Layout of the Michigan Mars Environmental Chamber, including its pressure, temperature and relative humidity control system.

2.2 Pressure Control

The MMEC can simulate pressure between 10 and 10^5 Pa, with narrower pressure ranges calibrated based on the experiment. To simulate the Martian atmosphere for the purpose of all studies reported on in this thesis, the pressure control system is set up to accurately control the pressure between ~100 and 1450 Pa. This includes nearly the entire Martian pressure range at the

surface [*Martínez et al.*, 2017], excluding only the highest mountain peaks such as that of Olympus Mons.

The pressure in the atmospheric chamber is controlled by an automated feedback control system. The chamber is fed by a manually regulated, constant flow of compressed bone-dry or instrument grade CO_2, with moisture content of <20 ppm or <10 ppm respectively. The pressure inside the chamber is measured by an MKS Baratron® 627B absolute pressure transducer with an accuracy of 0.12% and a resolution of 0.001%. On the other end of the chamber a BOC Edwards GVSP 30 vacuum scroll pump evacuates the chamber with a maximum possible displacement of 36 m^3/h. The outflow is throttled by an MKS 653B butterfly throttle control valve using a high-speed stepper motor that can open and close within 1.7 seconds. This valve is controlled by an MKS 1651C digital pressure controller, commanded by the GUI. This setup allows for an easy control of the pressure system through the GUI with a stability of the pressure set point of < 1 Pa in steady operations.

2.3 Temperature Control

The MMEC has achieved sample temperatures from 145 to 500 K on its thermal plate. All temperatures ever measured on the surface of Mars fall inside this range [*Martínez et al.*, 2017]. The thermal plate is cooled using liquid nitrogen (LN_2). The boiling point of nitrogen at 77 K at ambient pressure allows for even lower temperatures, than those tested so far. The liquid nitrogen enters the thermal plate through insulated tubing and cools it through a series of cooling loops on its bottom side, before exiting. The LN_2 flow is controlled through a Valbia VB030 actuator motor that can open and close a ball valve in the LN_2 line within 8 seconds. Watlow Firerod® cartridge heaters are embedded in the thermal plate to raise the temperature. An Omega thermocouple

measures the plate temperature with an accuracy of ±1.1 K. The thermal system is controlled by a Watlow EZ-Zone® PID controller connected to the GUI. Additionally eight Omega resistance temperature detectors (RTDs) can be placed wherever needed inside the chamber and are connected to a Lakeshore model 218 temperature monitor which also feeds the measurements to the GUI.

2.4 Relative Humidity Control

The entire range of relative humidity values observed on Mars can be simulated in the MMEC at the corresponding temperatures. Lowest achievable relative humidity values range from <1% at temperatures >250 K to ~5% at temperatures <215 K. On the other end of the humidity range we can simulate supersaturation (RH >100%) at any Martian temperature.

These values are achieved by using a manually controlled humidity system in the MMEC. A sealed water reservoir outside the chamber provides the necessary supply of water vapor. This supply's temperatures is regulated by a Thermo Scientific NESLAB RTE 740 bath circulator that runs refrigerant through a cooling loop embedded in the water reservoir, at temperatures between 233 and 473 K. This effectively controls the water vapor pressure above the water in the reservoir, feeding into the MMEC. The flow of water vapor from the reservoir into the environmental chamber is regulated manually by a needle valve. To measure the current relative humidity inside the chamber at the location of the sample an Anest Iwata ISP-250B dry scroll vacuum pump draws a small sample of atmosphere from the sample area to the outside of the chamber using stainless steel tubing. This tubing is kept at a higher temperature than the sample area to ensure no frost formation in the tubing. This chamber atmosphere sample is drawn by the pump through a Buck Research Instruments CR-1A chilled mirror hygrometer which measures its frost point. The flow

rate through the hygrometer is controlled with a manual valve and an Omega FMA-1606 flow meter. The relative humidity at the sample inside the chamber is then determined using the measured frost point and temperature at the sample [*Savijärvi and Määttänen*, 2010]:

$$RH = \frac{e}{e_{s,i}(T)} = \frac{e_{s,i}(T_f)}{e_{s,i}(T)}$$

$$e_{s,i}(T) = 611.35\ exp\frac{22.542(T - 273.16)}{T + 0.32}$$

where e is the water vapor pressure, $e_{s,i}$ is the saturation vapor pressure over ice (both in Pa), T is the temperature at the sample and T_f is the frost point temperature measured by the hygrometer (both measured in K). The hygrometer also feeds its measurements to the GUI.

2.5 Supporting Instruments

The MMEC can be fitted with a variety of instruments. Two quartz-glass windows, one directly above the thermal plate allow optical instruments to observe the sample area from outside the chamber. Two electrical feedthroughs (32 pins and 15 pins) allow further instrumentation inside the chamber and can easily be replaced by other types of feedthroughs. We have used a Kaiser Optical Systems RXN1-532 Raman spectrometer with 17 inch standoff optics for most of the experiments discussed in Chapters III to V. This is a 532 nm laser Raman spectrometer with a spectral range of 100 to 4375 cm^{-1}. The standoff optics allow the entire instrument probe head to remain outside the chamber without having to expose it to Martian conditions. We use the Raman spectrometer as a diagnostic tool to identify phase changes of water substance and the hydration of salts. Typically, we accumulate multiple multi-second shots of the laser using the Kaiser Optical Systems HoloGRAMS™ 4.2 software to improve the signal quality and errors. The penetration depth of the Raman laser depends on the optical properties of the sample. As an example, we have

observed a strong signal of water ice covered by a 2 mm deep layer of liquid brine but nearly no signal of water ice covered by a layer of crystalline salt of the same thickness.

For the purpose of instrument calibration, we can install a variety of in-situ relative humidity sensors inside the chamber. The recalibration of one such sensor, the backup engineering unit of the polymer-based capacitive relative humidity sensor of the Thermal and Electrical Conductivity Probe (TECP) that flew on the Phoenix mission is discussed in Chapter VI. Other relative humidity sensors that have been used inside the MMEC for calibration include engineering models of the relative humidity sensor on the Rover Environmental Monitoring Station (REMS) of the Mars Science Laboratory (MSL) Curiosity rover and an engineering model of the relative humidity sensor on the Mars Environmental Dynamics Analyzer (MEDA) of the Mars 2020 rover.

Further instruments that have been installed inside the MMEC include a microwave ring resonator for soil moisture measurements, an electromagnetic field sensor, a digital camera for sample observation and a microscope.

CHAPTER III

Searching for Brine on Mars Using Raman Spectroscopy

This chapter is published: Fischer, E. (2016), Searching for brine on Mars using Raman spectroscopy/Detección de salmueras en Marte mediante espectroscopia Raman. *Física de la Tierra, 28*, 181-195.

Abstract

In the last few years, water ice and perchlorate salts capable of melting this ice and producing liquid solutions have been discovered at the surface and shallow subsurface of Mars. In addition to via melting of ice, perchlorate salts may also form liquid solutions by absorbing water vapor when the relative humidity is above a certain threshold in a process known as deliquescence. Formed either by melting or deliquescence, liquid solutions (brine) are the most likely way of liquid water activity on the Martian surface and in the shallow subsurface and are therefore important to understand the habitability of Mars. Using Raman spectroscopy, we provide reference spectra of various mixing states of liquid water, water ice and calcium perchlorate, all of which can occur during brine formation. We focus on the perchlorate symmetric stretching band and the O-H stretching vibrational band to distinguish brine from crystalline salt and water ice. We show

that perchlorate brines can be identified by analyzing the peaks and their widths in the decomposed Raman spectra of the investigated samples. This serves as an important reference for future in-situ Raman spectrometers on Mars, such as those on the ExoMars and Mars 2020 rovers and can aid in the detection of brine formation on Mars.

3.1 Introduction

Liquid water is one of the ingredients needed for potential past or present habitability of Mars. One of the likely forms in which liquid water can temporarily form and persist on the Martian surface or in the shallow subsurface is in a salty solution as brine. The salt stabilizes the liquid state against the low pressure and temperature environment. Other possible forms of liquid water are undercooled liquid interfacial water, subsurface melt water and ground water [*Martínez and Renno*, 2013]. Here, we focus on brine because it is the most likely form of temporarily stable bulk liquid water on the surface or in the shallow (~10 cm) subsurface of Mars.

Perchlorate salts have been shown to be a promising candidate for brine formation on Mars. Perchlorate salts of calcium, magnesium and sodium were detected in-situ at the Phoenix landing site in Mars' northern polar region using data from the Wet Chemistry Laboratory instrument [*Hecht et al.*, 2009; *Kounaves et al.*, 2014], as well as at Gale crater using data from the Sample Analysis at Mars instrument [*Glavin et al.*, 2013; *Leshin et al.*, 2013]. Furthermore, perchlorate salts have been detected at mid-latitudes using satellite measurements by the High Resolution Imaging Science Experiment and some studies indicate that they might temporarily produce brines, explaining the evolution of Recurring Slope Lineae [*Ojha et al.*, 2015]. Furthermore, evidence suggesting temporarily liquid brine has been observed by the Phoenix lander [*Rennó et al.*, 2009]. Two different types of brine formation from perchlorate salts have been suggested. One is brine

formation by deliquescence, the absorption of atmospheric water vapor by hygroscopic salts (e.g. perchlorates) [*Chevrier et al.*, 2009; *Gough et al.*, 2011; *Nuding et al.*, 2015]. The other is brine formation by melting of water ice in contact with the salt [*Fischer et al.*, 2014]. Water ice has been detected in the shallow subsurface from mid-latitude to polar regions of Mars, both remotely using satellite measurements and in-situ [*Boynton et al.*, 2002; *Feldman et al.*, 2002; *Mitrofanov et al.*, 2002; *Byrne et al.*, 2009; *Smith et al.*, 2009].

Raman spectroscopy is a useful tool to detect brine. In the upcoming years two ground-based missions are planned to use Raman spectroscopy to analyze surface material on Mars. The ExoMars Rover, to be launched in 2020, will carry a Raman spectrometer as part of the Pasteur instrument suite, primarily to search for biosignatures on Mars [*Rull et al.*, 2013]. Mars 2020 will carry the Scanning Habitable Environments with Raman and Luminescence for Organics and Chemicals (SHERLOC) instrument, a Raman spectrometer used to detect organic compounds [*Beegle et al.*, 2014]. Here, we show Raman spectra of material samples involved in the formation of brine on Mars. We show spectra for water ice, liquid water, hydrated calcium perchlorate, calcium perchlorate brine, saturated calcium perchlorate brine and hydrated (solid) calcium perchlorate that has been dried out from a solution. We focus on brines formed from calcium perchlorate because of its very low eutectic temperature (~199 K) [*Marion et al.*, 2010]. This low eutectic point allows a possible brine to stay liquid for long parts of the diurnal cycle. Furthermore, calcium perchlorate is the most common perchlorate salt at the Phoenix landing site and Gale crater [*Kounaves et al.*, 2014; *Glavin et al.*, 2013]. Our spectra have been obtained in the Michigan Mars Environmental Chamber (MMEC), a custom chamber able to accurately simulate Martian conditions in pressure, temperature and relative humidity. The goal of this study is to give an overview of the type of Raman spectra to expect when studying brine formation.

3.2 Methods and Setup

We obtained Raman spectra under Martian conditions using a combination of the MMEC and a Raman spectrometer. The MMEC is a cylindrical chamber with internal measurements of 64 cm in diameter and 160 cm in length, used for Martian environmental simulations and instrument testing (Figure 3.1). Pressure control is achieved by a dry scroll vacuum pump in combination with an MKS 653B butterfly valve and an MKS 1651C pressure controller. The chamber pressure can be adjusted between 10 and 10^5 Pa and bone-dry CO_2 is used as the Martian air simulant. The sample temperature can be set between 145 and 500 K using LN_2 in combination with Watlow cartridge heaters and is controlled by a Watlow EZ-ZONE® temperature controller and thermocouples. The MMEC uses a temperature controlled water bath to add water vapor to the chamber atmosphere for relative humidity control. A Buck CR1-A chilled mirror hygrometer is used to monitor the relative humidity at the sample. The entire range in relative humidity from ~0 to 100% can be simulated.

The Raman spectrometer used in this study to acquire the sample spectra is a Kaiser Optical Systems Inc. RamanRXN1 unit operating at a wavelength of 532 nm, with a spectral range of 100 – 4375 cm^{-1}, a power at the sample of 74 mW and a 17 inch standoff distance. This allows for the sensor head to operate from outside the vacuum chamber through a viewport. The spectrometer was calibrated using a neon light source, white light and cyclohexane. The spectral resolution is 1 cm^{-1}. All spectra were obtained by accumulating seven laser exposures of the sample with an integration time of 7 s each. We focus on the Raman spectroscopic regions of the perchlorate symmetric stretching band at ~900 – 1000 cm^{-1} and the O-H stretching vibrational band at ~3000 – 3800 cm^{-1} to detect characteristic peaks of the tested materials.

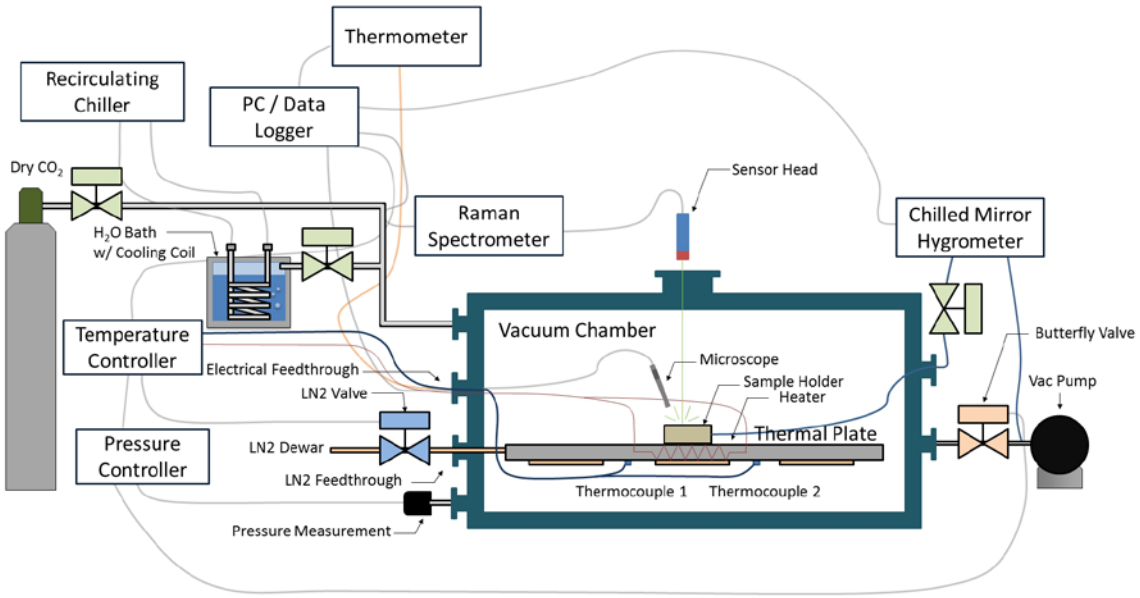

Figure 3.1: Setup of the Michigan Mars Environmental Chamber (MMEC).

We chose calcium perchlorate tetrahydrate for simulating Martian brine as it is a likely brine candidate due to its ubiquity on Mars, its hygroscopic properties and its low eutectic temperature [*Hecht et al.*, 2009; *Kounaves et al.*, 2014; *Glavin et al.*, 2013; *Leshin et al.*, 2013; *Ojha et al.*, 2015; *Marion et al.*, 2010]. Other perchlorate hydrates like those of sodium or magnesium show similar spectra as calcium perchlorate [*Fischer et al.*, 2014], but especially magnesium perchlorate tends to show fluorescence when excited by a 532 nm laser. Lower wavelengths have shown to be successful in preventing this [*Nikolakakos and Whiteway*, 2015].

We use a 0.3 cm^3 cylindrical sample holder cup for all experiments. For the liquid water spectrum it was filled with 0.15 cm^3 of distilled water. The spectrum was taken at ambient pressure and temperature to prevent evaporation. All remaining spectra were obtained at a Martian pressure of 800 Pa. To obtain the water ice spectrum we froze distilled water at 190 K. We obtained Raman spectra of a thin layer (< 2 mm) of calcium perchlorate tetrahydrate with average particle diameter < 300 μm at 190 K to prevent hydration state changes or deliquescence. We chose this particle size

because particles of this size can be transported by saltation on Mars and may accumulate locally [*Kok and Renno*, 2009]. Next, we obtained a Raman spectrum of an unsaturated calcium perchlorate solution (brine) with a concentration of about 600 g/L and a saturated brine, both at ~255 K. We obtained the saturated brine spectrum by letting excess water evaporate from the solution at ~255 K until the salt recrystallized while regularly taking Raman spectra. The final spectrum is of calcium perchlorate, recrystallized from a brine by evaporation of the water. The sample was inspected visually and no liquid component was found after the water was evaporated for 10 hours. The spectrum was then taken after the sample was cooled to 190 K to compare the recrystallized calcium perchlorate with the original salt at the same temperature and to ensure that any remaining solution has frozen.

We use Gaussian decomposition to analyze the obtained spectra quantitatively. A baseline is subtracted and each spectrum is decomposed into a number of Gaussian curves. The Gaussians' positions, full width at half maximum (FWHM) and their relative amplitude are obtained. We imposed the condition that each local maximum (outside of the noise) has to be resolved and that the final fit shows an $\bar{R}^2 \geq 98\%$. It should be noted that the accuracy in peak position in the decomposition is greater with more narrow peaks, and wider peaks present a larger uncertainty in the exact position of the Gaussian.

3.3 Results

Here we show Raman spectra and their Gaussian decompositions of six materials and mixtures that are related to the formation of brine on Mars. In-situ spectra will likely be more complex mixtures of these materials or mixtures with other materials, the most likely being the regolith. The spectra shown here are obtained under simplified mixture conditions to develop a

database for comparison with more complex spectra that might be observed in-situ on Mars. All Gaussian decomposition peaks described here are summarized in Table 3.1.

	ClO_4 peaks	**O-H peaks**
H2O (l)		3230 (217), 3420 (218), 3540 (206), 3620 (109)
H2O (s)		3046 (99), 3115 (57), 3227 (206), 3336 (56), 3399 (140)
$Ca(ClO_4)_2.4H_2O$	939 (16)*, 952 (9)	3115 (81)*, 3249 (113)*, 3437 (147)*, 3437 (27), 3467 (23), 3487 (15), 3509 (25), 3536 (23), 3560 (155)*, 3602 (13), 3630 (18)
$Ca(ClO_4)_2$ solution	934 (13)	3282 (268), 3454 (178), 3582 (125)
$Ca(ClO_4)_2$ solution (saturated)	936 (17)	3256 (219)*, 3495 (249), 3555 (106)
$Ca(ClO_4)_2.xH_2O$ (recrystallized)	934 (13)	3311 (271), 3389 (66), 3456 (38), 3496 (31), 3520 (19), 3543 (17), 3546 (132)

Table 3.1: Decomposed peak positions and widths (in parentheses) of the Raman spectra shown in this study. Asterisks indicate weak peaks with low intensities.

In the first experiment we obtained the Raman spectrum of pure liquid water at ambient conditions (Figure 3.2). The band of interest for liquid water is the O-H stretching vibrational band from ~3000 – 3800 cm^{-1}. Since this is a pure liquid water, no peaks are observed in the perchlorate symmetric stretching band. The Gaussian decomposition shows 4 main components in the O-H band, similar to those reported by *Zhang and Chan*, (2003), at 3230, 3420, 3540 and 3620 cm^{-1}. The first two are ice-like components, while the other two are unique for liquid water. All four peaks show FWHM values greater than 100 cm^{-1}. Furthermore, there is a small temperature dependence of the peak positions and relative intensities observable between the 3230 and 3420 cm^{-1} peaks [*Dolenko et al.*, 2000]. We observed a shift of the 3230 cm^{-1} peak towards higher wavenumbers with decreasing temperature, while the 3420 cm^{-1} peak shifted towards lower wavenumbers with decreasing temperature. Both shifts show a rate of ~0.2 – 0.5 cm^{-1}/K. We also observed an increase of the 3230 cm^{-1} peak's relative intensity compared to the 3420 cm^{-1} peak with decreasing temperature.

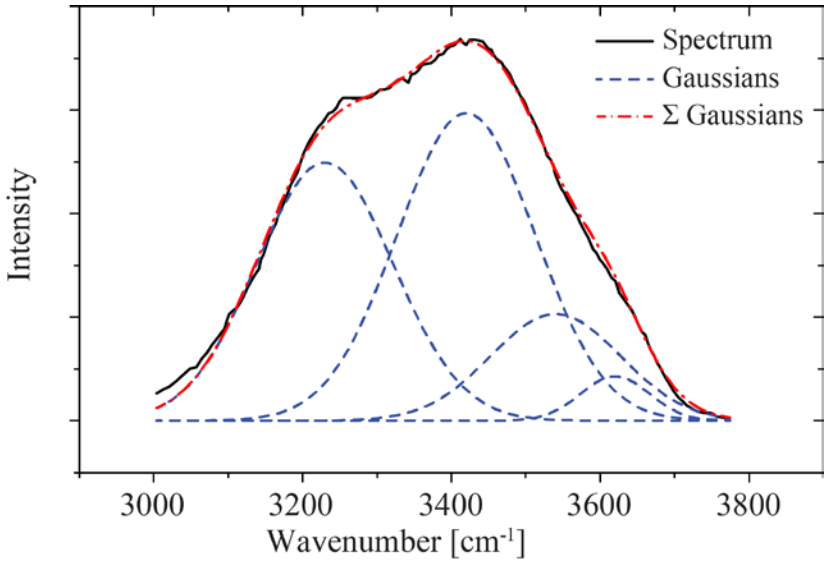

Figure 3.2: Decomposition of the Raman spectrum of liquid water in the O-H stretching vibrational band.

In the second experiment we obtained the Raman spectrum of water ice at various temperatures. Figure 3.3 shows the spectrum at 190 K. Similar to liquid water, the band of interest for water ice is the O-H stretching vibrational band. The Gaussian decomposition shows 5 peaks at 3046, 3115, 3227, 3336 and 3399 cm^{-1}. The latter two peaks coincide with the ice-like peaks in the liquid water spectrum. The 3115 cm^{-1} peak shows the strongest intensity and can be used as an indicator of the presence of water ice in a mixture. Similar to the 3420 cm^{-1} peak in the liquid water spectrum, the peaks in the water ice spectrum shift towards lower wavenumbers with decreasing temperature at the same rate of ~0.3 – 0.5 cm^{-1}/K. A non-negligible change in peak position with pressure was not observed, even for the large atmospheric pressure difference between ambient and Mars pressures.

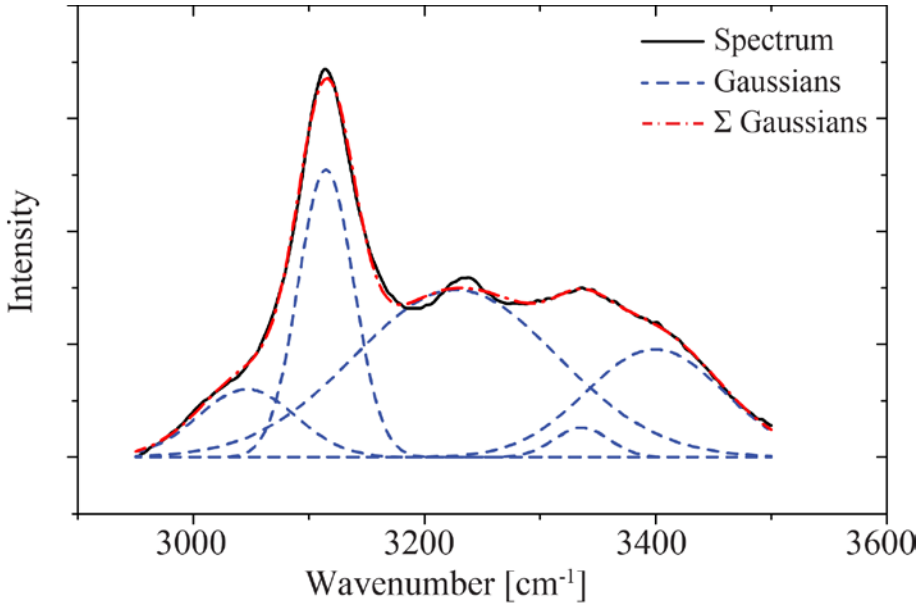

Figure 3.3: Decomposition of the Raman spectrum of water ice in the O-H stretching vibrational band.

In the third experiment we obtained the Raman spectrum of $Ca(ClO_4)_2.4H_2O$ at 190 K. There are two spectral bands of interest for perchlorate salts: the perchlorate symmetric stretching band (~900 – 1000 cm^{-1}) (Figure 3.4a) and the O-H stretching vibrational band (Figure 3.4b). The perchlorate band shows a prominent peak at 952 cm^{-1}, representative of the tetrahydrate. In the case of an anhydrous perchlorate salt, the perchlorate band shows a peak at 990 cm^{-1} and the O-H band does not show any peaks [*Nuding et al.*, 2014]. The minor Gaussian at 939 cm^{-1} in the perchlorate band might be due to a small amount of a higher hydration state in the sample. The O-H band shows a number of very narrow peaks at 3437, 3467, 3487, 3509, 3536, 3602 and 3630 cm^{-1}, with FWHM values of less than 50 cm^{-1}, typical for crystalline hydrated perchlorates [*Fischer et al.*, 2014]. The first three low-intensity peaks at 3115, 3248 and 3437 cm^{-1} are close in position and width to water ice peaks (see Table 3.1).

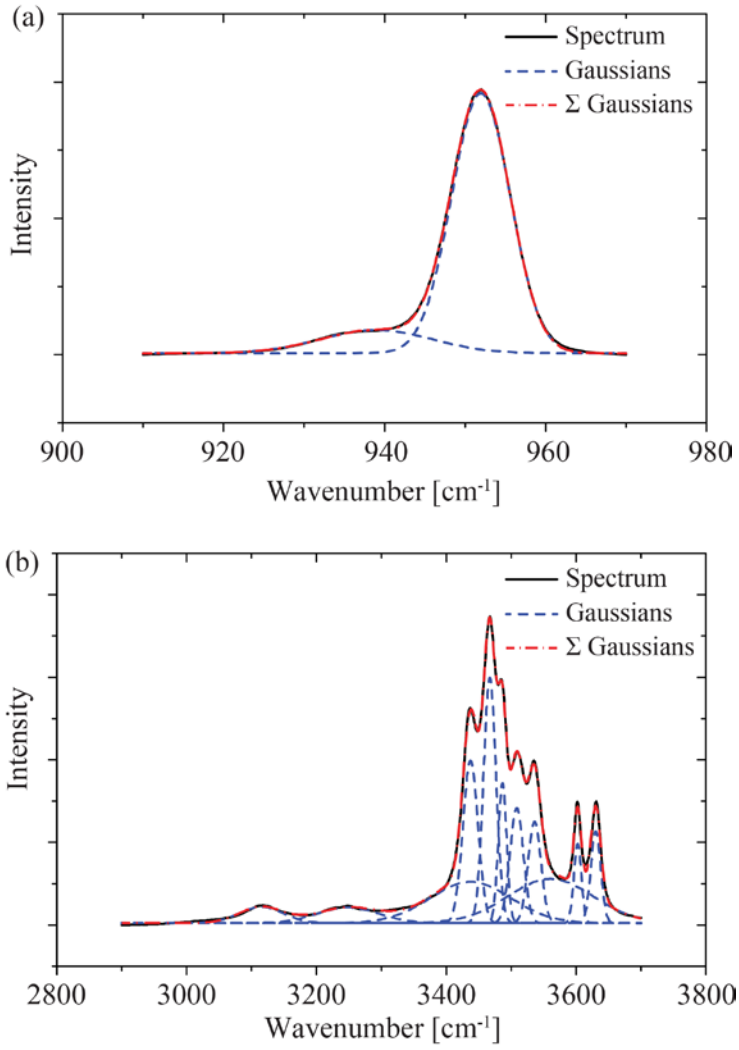

Figure 3.4: Decomposition of the Raman spectrum of hydrated perchlorate salt. (a) Perchlorate symmetric stretching band. (b) O-H stretching vibrational band.

In the fourth experiment we obtained the Raman spectrum of a calcium perchlorate solution (brine) at 255 K, 56 K above the eutectic temperature and typical for midday temperature values at the Phoenix landing site [*Savijärvi and Määttänen*, 2010]. The perchlorate stretching band (Figure 3.5a) shows a single Gaussian peak centered at 934 cm^{-1}, indicating that no $Ca(ClO_4)_2.4H_2O$ phase remains. The O-H band (Figure 3.5b) shows three wide Gaussian peaks centered at 3282, 3454 and 3582 cm^{-1}, with FWHM values greater than 100 cm^{-1}. These peaks show strong similarities in position and width to the liquid water peaks described above, with only

the highest wavenumber and lowest intensity water peak missing. The addition of the perchlorate to the water results in a shift of the liquid water peaks to higher wavenumbers. The exact shift cannot be quantified here, due to the above-mentioned uncertainty in exact position of the wide peaks. Another change from the pure water spectrum is the stronger relative intensity of the 3882 cm^{-1} peak due to the addition of the perchlorate salt. The intensity of this peak in the brine is similar to the two lower wavenumber peaks, while for pure liquid water its relative intensity was less than half.

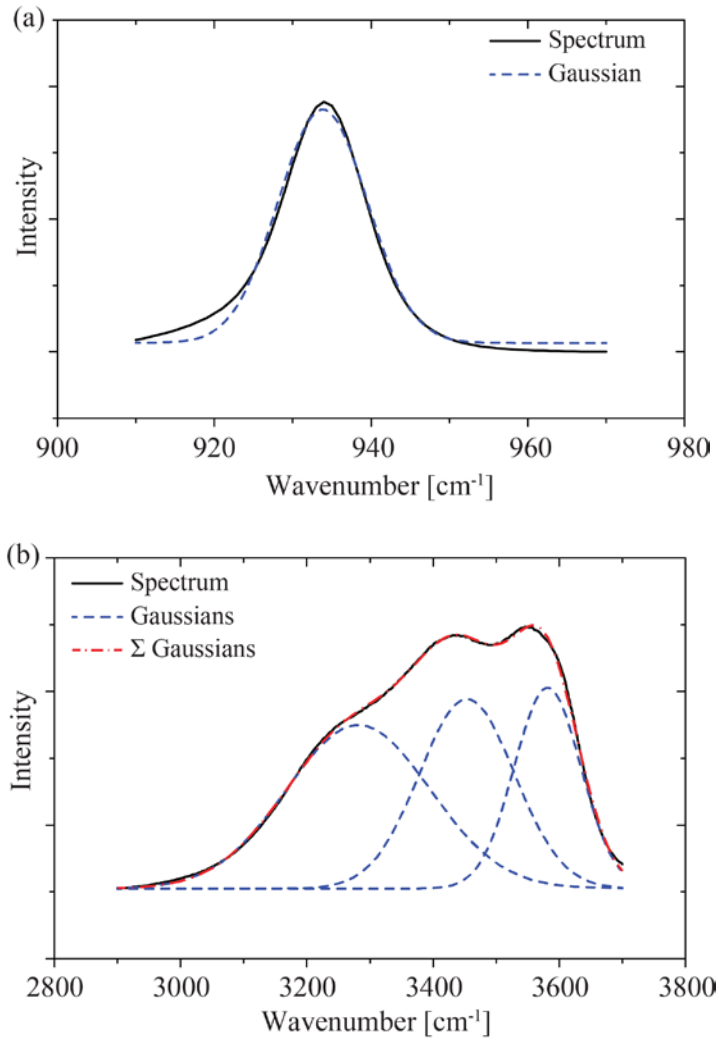

Figure 3.5: Decomposition of the Raman spectrum of a perchlorate salt solution. (a) Perchlorate symmetric stretching band. (b) O-H stretching vibrational band.

In the fifth experiment we obtained the Raman spectrum of a saturated calcium perchlorate brine at 255 K. The perchlorate stretching band of the saturated solution (Figure 3.6a) shows no significant difference from the non-saturated case. The peak is centered at 936 cm^{-1} and no peak at higher wavenumbers appears in this band. The O-H spectrum shows 3 Gaussian peaks at 3256, 3495 and 3555 cm^{-1} with FWHM values greater than 100 cm^{-1} (Figure 3.6b). These positions and widths are comparable to those of the non-saturated case. The major difference lies in the relative intensities of the peaks. With an increasing perchlorate salt concentration in the solution, the 3555 cm^{-1} peak's relative intensity increases compared to those of the other two Gaussians in the O-H spectrum. We did not observe a continued trend of a peak position shift towards higher wavenumbers.

In the sixth and final experiment we obtained the Raman spectrum of calcium perchlorate recrystallized from a solution to simulate a dried out brine under Martian conditions. We ensured that the entire sample was dried out by stirring the sample and visual inspection. The spectrum was obtained at 190 K to compare with the original tetrahydrate. While the sample is crystallized and dried out, the perchlorate band (Figure 3.7a) shows a single Gaussian peak at 934 cm^{-1}, at the same position as for the liquid solution and lower than the 952 cm^{-1} peak of the calcium perchlorate tetrahydrate shown in Figure 3.4a. The O-H band is more complex (Figure 3.7b), showing two wide peaks (FWHM > 100 cm^{-1}) at 3311 and 3546 cm^{-1}, and five narrow peaks (FWHM < 100 cm^{-1}) with similar positions and widths to those of the calcium perchlorate tetrahydrate shown in Figure 3.4b, showing that the salt is indeed crystalline again.

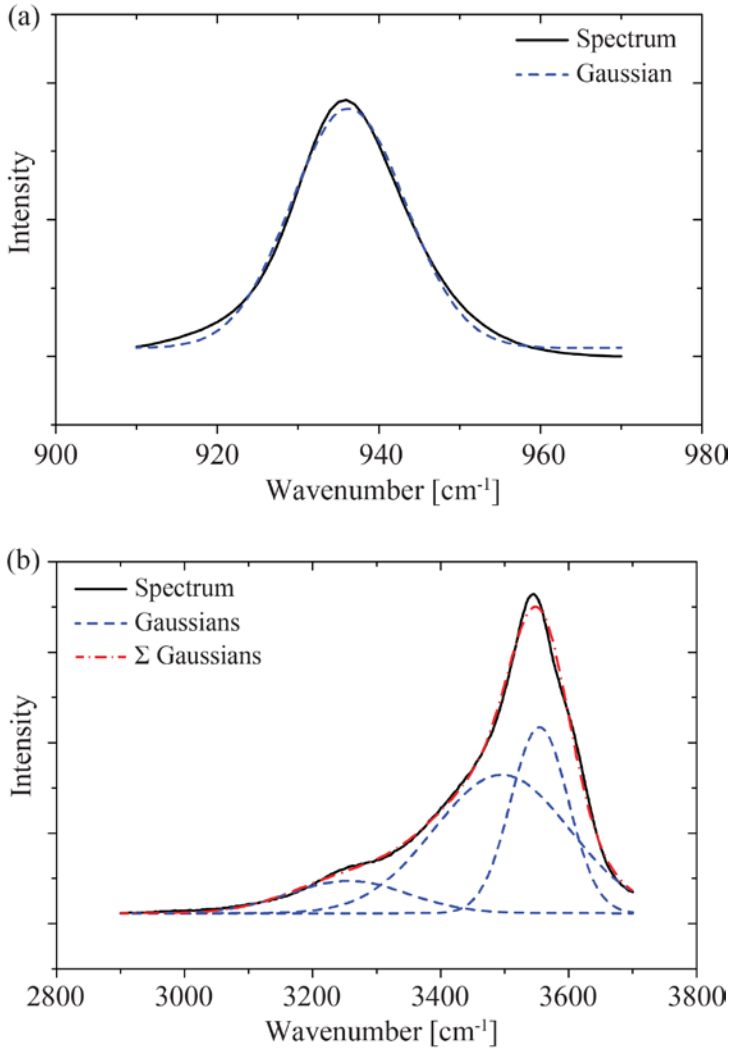

Figure 3.6: Decomposition of the Raman spectrum of a saturated perchlorate salt solution. (a) Perchlorate symmetric stretching band. (b) O-H stretching vibrational band.

3.4 Discussion

The Raman spectrum obtained in the first experiment (Figure 3.2) serves as a reference for the detection of a liquid water state. Although pure liquid water is unlikely to exist at Martian atmospheric conditions, the existence of the wide Gaussian peaks (FWHM > 100 cm^{-1}) around 3230, 3420 and 3540 cm^{-1} in any obtained sample is strong evidence for the existence of a form of liquid water. This can help identifying any liquid water state in a mixed sample obtained in-situ

on Mars. Care has to be taken with the 3230 and 3420 cm^{-1} water peak since they are both ice-like peaks and also existent in water ice.

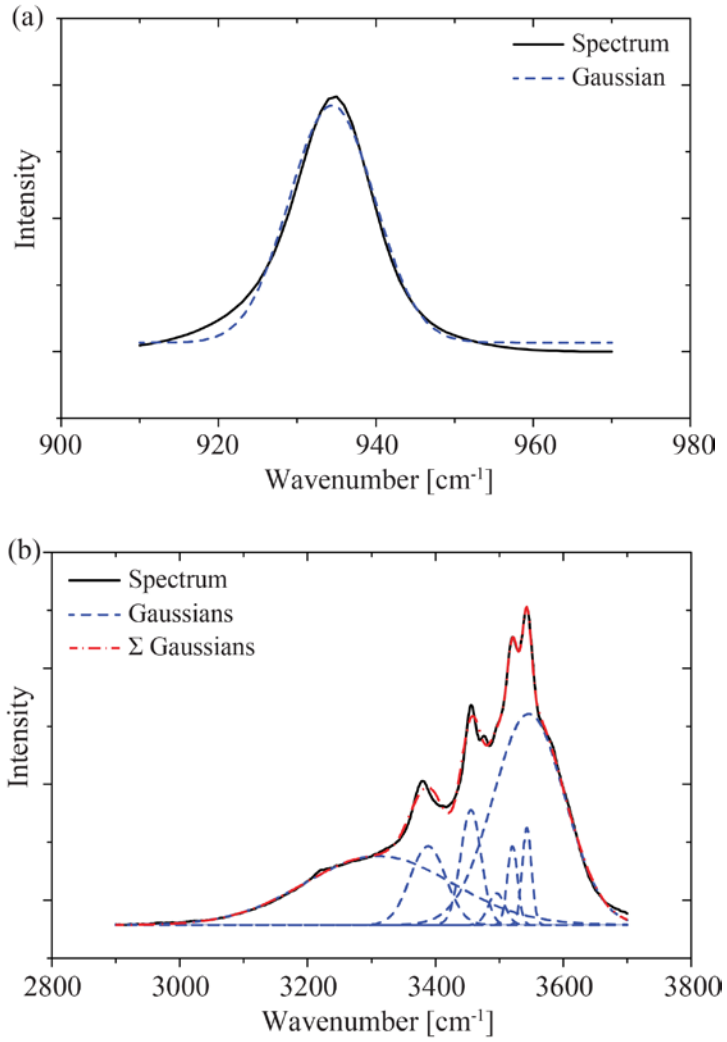

Figure 3.7: Decomposition of the Raman spectrum of a dried out perchlorate salt solution. (a) Perchlorate symmetric stretching band. (b) O-H stretching vibrational band.

The identification of water ice peaks in the second experiment (Figure 3.3) helps detecting subsurface ice on Mars as in the polar or mid-latitude regions for example [*Smith et al., 2009; Rennó et al.*, 2009]. Furthermore, frost events have been suggested at Gale crater [*Martínez et al.*,

2016]. Raman spectroscopy at equatorial latitudes can help identifying frost events such as those suggested.

The Raman spectrum of calcium perchlorate hydrate obtained in the third experiment (Figure 3.4) provides a reference for the verification of the existence of perchlorate salt hydrates in the Martian soil using Raman spectroscopy. The positions and narrow widths of the decomposed peaks clearly differentiate the hydrated (but crystalline) perchlorate salts from their briny solutions. The appearance of the O-H peaks for the perchlorate salts indicate hydration from an anhydrous state. Further hydration state changes between hydrated states show shifts in the perchlorate vibration band. The wider peaks in Figure 4b at 3115, 3248 and 3437 cm^{-1} typical for water ice (see Table 3.1) indicate that a small amount of water existed on the surface of the salt grains and froze when the temperature was lowered below the eutectic point. While the anhydrous perchlorate salts show a peak at ~990 cm^{-1}, hydrated states shift this peak to lower wavenumbers, such as ~952 cm^{-1} for the calcium perchlorate tetrahydrate or 934 cm^{-1} for higher hydration states [*Zhang and Chan*, 2003].

Figure 3.5 shows the Raman spectrum of a calcium perchlorate brine. The differences in the O-H spectrum between the wide, water-like peaks here and the narrower, more numerous peaks described above for the crystalline salt, are a clear method to identify the onset of brine formation from a crystalline perchlorate salt. This may aide in the detection of brine pockets in the Martian soil. The perchlorate vibrational band also shows a clear shift from the 952 cm^{-1} peak of the crystalline salt to the 934 cm^{-1} peak here, implying that this is another indicator (although not definitive) of brine formation.

Figure 3.6 shows the impact of an increased salt concentration on the Raman spectrum when compared to Figure 3.5. While the perchlorate peak shows no significant difference with

concentration, the relative intensity of the O-H peaks changes dramatically. Increasing the perchlorate salt concentration in the solution increases the relative intensity of the third O-H peak at 3555 cm^{-1}, compared to the other two peaks. We assume that this is the most likely Raman spectrum to be encountered on Mars when looking at a perchlorate brine.

We investigate the recrystallized perchlorate salt spectrum in Figure 3.7 to test the hypothesis that both the existence of the wide water-like peaks in the O-H band and the perchlorate band peak shift to 934 cm^{-1} are clear indicators of brine formation. The perchlorate vibrational band shows the single Gaussian peak at 934 cm^{-1}, in the same position as that of the liquid states, even though the sample was fully recrystallized. This suggests that the shift from 952 to 934 cm^{-1} observed for the liquid solution is not a sufficient indicator of the existence of a brine. We assume that this shift is an indicator of a change to a higher hydration state, such as calcium perchlorate octahydrate for example. Further research has to be performed to clarify this. The O-H vibrational band shows a return to the narrow (FWHM < 50 cm^{-1}) peaks in similar positions to those of the original calcium perchlorate tetrahydrate in Figure 3.4. This change in the O-H spectrum can be used to detect efflorescence of brine. Results of this experiment show that the O-H stretching vibrational band is better suited to distinguish between a solid perchlorate salt and a perchlorate brine.

3.5 Conclusion

The materials necessary to form brine at Martian conditions have been shown to exist from polar to equatorial latitudes on Mars. Perchlorate salts such as calcium perchlorate with their ability to form liquid solutions at very low temperatures are suggested to exist globally in the top layer of the Martian regolith. They can potentially form these brines by absorbing the limited amounts of

water vapor from the atmosphere or by melting bulk water ice that exists at the surface of polar latitudes and in the shallow subsurface of mid to polar latitudes. Here we show decomposed Raman spectra of various materials or mixtures involved in this brine formation process. We focus on calcium perchlorate as our example perchlorate salt because of its very low eutectic temperature ($T_e \approx 199$ K). Other perchlorate salts known to exist in the Martian regolith, such as magnesium or sodium perchlorate, show similar spectra in the O-H and perchlorate bands. The spectra shown here serve as a reference for future studies and in-situ measurements by Raman spectrometers on future landers or rovers. We show that the O-H spectrum is preferential in the detection of brine due to its clear changes in peak positions and widths with the change from crystalline salt to a solution. The perchlorate spectrum also shows a clear shift in the peak positions with changes in hydration state and state of matter, but our experiments show that this shift by itself is not a sufficient indicator of a brine. Our results show that Raman spectroscopy is an excellent tool for the in-situ detection of brine on Mars. A large database of experimentally obtained spectra can aid in the identification of constituents in mixed samples on Mars.

CHAPTER IV

Experimental Evidence for the Formation of Liquid Saline Water on Mars

This chapter is published: Fischer, E., Martínez, G. M., & Rennó, N. O. (2014), Experimental evidence for the formation of liquid saline water on Mars. *Geophysical Research Letters, 41*(13), 4456-4462.

Abstract

Evidence for deliquescence of perchlorate salts has been discovered in the Martian polar region while possible brine flows have been observed in the equatorial region. This appears to contradict the idea that bulk deliquescence is too slow to occur during the short periods of the Martian diurnal cycle during which conditions are favorable for it. We conduct laboratory experiments to study the formation of liquid brines at Mars environmental conditions. We find that when water vapor is the only source of water, bulk deliquescence of perchlorates is not rapid enough to occur during the short periods of the day during which the temperature is above the salts' eutectic value, and the humidity is above the salts' deliquescence value. However, when the salts are in contact with water ice, liquid brine forms in minutes, indicating that aqueous solutions

could form temporarily where salts and ice coexist on the Martian surface and in the shallow subsurface.

4.1 Introduction

Our view of Mars has changed dramatically in the past two decades, from an inhospitable cold desert to a potentially habitable planet. Water ice was discovered in the shallow subsurface of areas ranging from polar latitudes to midlatitudes [*Boynton et al.*, 2002; *Mitrofanov et al.*, 2002; *Feldman et al.*, 2002; *Smith et al.*, 2009; *Byrne et al.*, 2009]; salts such as $Ca(ClO_4)_2$, $Mg(ClO_4)_2$, and $NaClO_4$, capable of deliquescing and forming aqueous solutions at Martian temperatures were discovered in the polar and equatorial regions [*Hecht et al.*, 2009; *Glavin et al.*, 2013]. The idea that deliquescence (defined as the dissolution of a salt by the absorption of water vapor [*Mirabel et al.*, 2000]) is a slow process not capable of producing bulk aqueous solutions during the few hours of the diurnal cycle in which conditions are favorable for it is well established [*Möhlmann*, 2011] because Mars is extremely cold and dry [*Lewis et al.*, 1999; *Meslin et al.*, 2013]. This appears to contradict the discovery of observational evidence for deliquescence in Mars' polar region [*Rennó et al.*, 2009] and of possible flows of liquid brines in the equatorial region [*McEwen et al.*, 2011].

In an effort to shed light on this issue, we use Raman scattering spectroscopy [*Zhang and Chan*, 2003] to study the formation of liquid brines from bulk amounts of salt at Mars environmental conditions. Here we define "bulk" as a macroscopic collection of salt grains. First, we study the formation of liquid brines when water vapor is the only source of water (bulk deliquescence). Then, we investigate the formation of liquid brines when the salts are placed in direct contact with water ice like that observed in Mars' polar region [*Martínez et al.*, 2012; *Smith*

et al., 2009; *Whiteway et al.*, 2009]. Our results have important implications for the understanding of habitability because liquid water is essential for life as we know it, and halophilic terrestrial bacteria thrive in brines [*Mikucki et al.*, 2009; *Boetius and Joye*, 2009].

4.2 Methodology

4.2.1 Environmental Chamber

All experiments reported in this letter were conducted in the Michigan Mars Environmental Chamber (MMEC), a cylindrical chamber with internal diameter of 64 cm and length of 160 cm. The MMEC is capable of simulating temperatures ranging from 145 to 500 K, CO_2 pressures ranging from 10 to 10^5 Pa, and relative humidity ranging from nearly 0 to 100%.

We use salts from Sigma Aldrich with typical particle diameters <300 μm (determined by visual inspection of images of the salt particles). Particles of this size are the most easily transported by saltation [*Kok and Renno*, 2009] and therefore can easily be accumulated in low topographical features and then buried. In our experiments the laser beam of the Raman spectrometer is focused on the thin layer of the salt being investigated. We use layers of salt with a thickness of a few grains to ensure that it is within the penetration depth of the laser and thus to be able to detect the onset of the formation of liquid brines. Our results are not sensitive to particle size because deliquescence starts on defects on the surface of salt crystals, and Raman spectroscopy is capable of detecting the onset of deliquescence on the surfaces of the salt crystals. Once the salt particles start to absorb water, they start to coalesce, forming larger particles. Indeed, most particles are rough because they are aggregates of smaller particles.

We have conducted two sets of experiments, one to investigate deliquescence when the salt is exposed solely to water vapor and the other to investigate the formation of liquid brines when a thin layer of salt is placed in direct contact with a layer of water ice, like that found in the shallow Martian subsurface by the Phoenix lander [*Smith et al.*, 2009; *Rennó et al.*, 2009]. In both cases the CO_2 atmosphere was kept saturated with water vapor at a total pressure of 800 Pa. In the first set of experiments, the temperature of the sample was fixed at -50°C, well above the -74°C eutectic temperature of $Ca(ClO_4)_2$ [*Marion et al.*, 2010]. In the second set of experiments, the salt was first placed on top of a layer of water ice at temperatures well below the salt's eutectic temperature. Then, the temperature was raised to values above the eutectic temperature at a rate of about 6°C/h to simulate the rate of the temperature increase in the shallow (~1 cm deep) Martian subsurface [*Savijärvi and Määttänen*, 2010]. This rate was increased at temperatures well above the eutectic point to speed up the experiment.

4.2.2 Raman Spectroscopy

Raman spectroscopy is an excellent tool for studying hydration and deliquescence. For example, in $Ca(ClO_4)_2$ vibrations of the tetrahedral perchlorate ion of the anhydrous crystalline salt produce a single Raman spectral peak at wave number $\nu \sim 990$ cm^{-1} [*Nuding et al.*, 2013], vibrations of perchlorate ions in hydrates produce spectral peaks at ~953 and ~936 cm^{-1}, while vibration of perchlorate ion pairs in aqueous solutions also produces a spectral peak at ~936 cm^{-1}. The spectral peaks at ~953 and 936 cm^{-1} are ideal for detecting changes in the hydration state [*Zhang and Chan*, 2003], but they can also be used to detect the formation of a solution, in particular the shift of the 953 to the 936 cm^{-1} spectral peak [*Gough et al.*, 2011]. Furthermore, changes in spectral peaks caused by O-H stretching can be used to detect a solution

unambiguously. As shown below, stretching of O-H at Mars environmental conditions produces spectral peaks from around 3000 to 3600 cm^{-1}. This portion of the spectrum shows distinct changes in the number, position, and width of spectral peaks when a solution forms. We argue that the O-H spectral region is more appropriate for studying the formation of liquid brines than the perchlorate spectral bands between ~930 and ~1000 cm^{-1}. The main reasons for this are that some of the O-H spectral peaks depend directly on the presence of liquid water and that the perchlorate spectral peaks depend most strongly on the hydration state of the salts and the concentration of the solutions [*Zhang and Chan*, 2003; *Miller and Macklin*, 1985].

We use Raman spectroscopy to study the formation of liquid perchlorate brines at temperature, pressure, and humidity conditions of the Mars polar region. Our analysis focuses on $Ca(ClO_4)_2$ because it has been detected at the Phoenix landing site, it has a low eutectic temperature (T_e), and it is expected to be ubiquitous on Mars [*Kounaves et al.*, 2014]. First, we obtain separate spectra of water ice and crystalline hydrated perchlorate salt experimentally, while that of liquid water was taken from *Zhang and Chan* [2003]. Then, we use Gaussian decomposition to compare these single spectra to the spectra taken during the two sets of experiments described above. This technique is applied to all Raman spectra obtained to determine the wave number and full width half maximum (FWHM) of their decomposed spectral peaks. After subtracting a baseline, the measured spectrum is decomposed into Gaussians using the Origin® software package. The condition that every relative maximum and minimum of the relevant portions of the spectrum has to be resolved is imposed. This resulted in fits with $\bar{R}^2 \geq 0.997$. A summary of the properties of the Gaussian decompositions of the spectra in the O-H stretching region shown here is presented in Table A.1 in the Appendix. Raman spectra were taken every 5 min and normalized by the amplitude of the perchlorate stretching band.

4.3 Results

4.3.1 Spectra of Single Components

Figure 4.1 shows the decomposed reference spectra for the single salt, water ice, and liquid water. Figure 4.1a shows that the Gaussian decomposition of $Ca(ClO_4)_2 \cdot 4H_2O$ at -50°C contains spectral peaks similar to those shown in literature [*Nuding et al.*, 2013]. It contains eight narrow peaks at 3446, 3471, 3487, 3515, 3542, 3564, 3603, and 3628 cm^{-1}, with all peaks except for one exhibiting a full width at half maximum (FWHM) $\leq$ 50 cm^{-1}. Figure 4.1b shows that the decomposition of the spectrum of pure water ice contains five peaks at ~3046, ~3115, ~3227, ~3336, and 3399 cm^{-1}, all with FWHM > 50 cm^{-1}. Figure 4.1c shows the Gaussian decomposition for liquid water with peaks at 3230, 3420, 3540, and 3620 cm^{-1} from data obtained from literature [*Zhang and Chan*, 2003], indicating that all spectral peaks have FWHM > 50 cm^{-1}. These spectral features are summarized in Table 4.1. The 3230 and 3420 cm^{-1} peaks for liquid water are ice-like components (C1 and C2), which explain their proximity to the 3227 and 3399 cm^{-1} peaks in ice.

In a first set of experiments, $Ca(ClO_4)_2 \cdot 4H_2O$ is exposed to a CO_2 atmosphere saturated with water vapor. In a second set of experiments, $Ca(ClO_4)_2 \cdot 4H_2O$ is placed in direct contact with ice. By comparing the number of decomposed spectral peaks, their wave number, and their width in both sets of experiments with those of the references summarized in Table 4.1, hydrated crystalline salts can be distinguished from solutions.

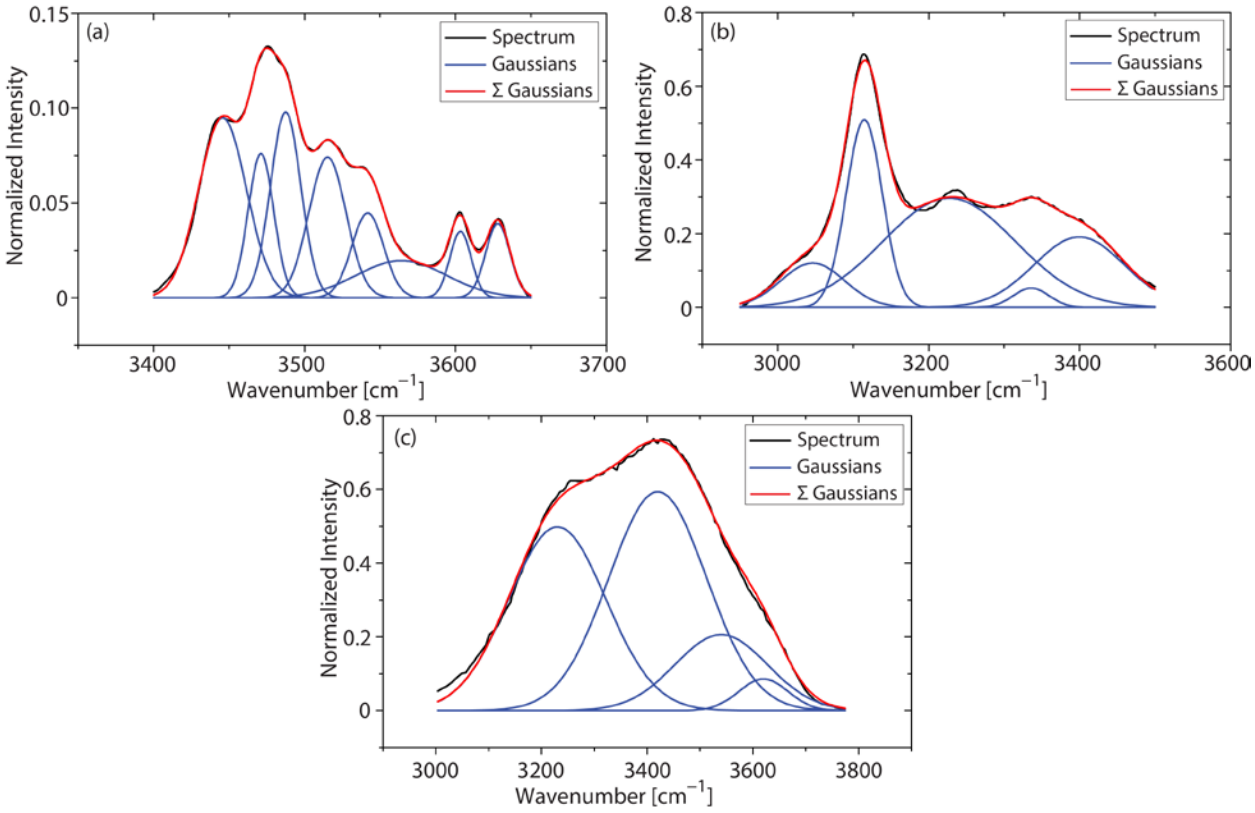

Figure 4.1: Decomposed Raman spectra of $Ca(ClO_4)_2 \cdot 4H_2O$, water ice, and liquid water: (a) The decomposed O-H vibrational spectrum of hydrated $Ca(ClO_4)_2$ at -50°C, 800 Pa, and 100% RH shows eight Gaussian components, at 3446, 3471, 3487, 3515, 3542, 3564, 3603, and 3628 cm^{-1}, with $\bar{R}^2 \geq 0.999$. (b) Water ice at -80°C and 800 Pa indicating five Gaussian components, at 3046, 3115, 3227, 3336, and 3399 cm^{-1}, with $\bar{R}^2 \geq 0.997$. (c) Decomposition of the O-H vibrational region of the spectrum of liquid water [*Zhang and Chan*, 2003], indicating four broad Gaussian components, at 3230, 3420, 3540, and 3620 cm^{-1}, with $\bar{R}^2 \geq 0.997$.

Substance	**Spectral peaks at ν (cm^{-1})**
$Ca(ClO_4)_2$ hydrates	3446 (37), 3471 (20), 3487 (24), 3515 (29), 3542 (25), 3564 (70), 3603 (17), 3628 (19)
Water ice	3046 (99), 3115 (57), 3227 (206), 3336 (56), 3399 (140)
Liquid water	3230 (217), 3420 (218), 3540 (206), 3620 (109)

Table 4.1: Spectral Signatures of Calcium Perchlorate, Liquid Water, and Water Ice. Values in parentheses are FWHM values for each peak.

4.3.2 Spectra of Brine Formation Experiments

Figure 4.2 shows results for the first set of deliquescence experiments. $Ca(ClO_4)_2$ at a constant temperature of -50°C (well above its eutectic point at -74°C) is exposed to a CO_2 atmosphere at a pressure of 800 Pa saturated with water vapor. Figure 4.2a shows eight narrow peaks and shoulders in the O-H vibrational band, indicating the presence of hydrated crystalline salts throughout the experiment. Figure 4.2b shows the decomposition of the spectrum of the O-H vibrational band, taken 205 min after the beginning of the experiment whose results are shown in Figure 4.2a. It shows that the O-H spectrum can be decomposed into Gaussians representing the crystalline salt, with the same number of peaks and similar positions and widths (narrow) as the crystalline salt (Figure 4.1a). This indicates the presence of $Ca(ClO_4)_2$ hydrates only. Indeed, spectral peaks in the O-H band indicating the occurrence of a solution were not detected within the limit of detection of the Raman spectrometer, even after the samples had been kept at T = -50°C (about 25°C above T_e) and RH = 100% for almost 3.5 h. Since the O-H spectrum remains unchanged over the duration of the experiment, whereas a small peak appears in the perchlorate band at 936 cm^{-1} (Figure 4.2a), and $Ca(ClO_4)_2 \bullet 4H_2O$ is not stable under the above mentioned experimental conditions, we conclude that a partial change in the hydration state from tetrahydrate to octahydrate occurs.

Similar results are obtained for the Gaussian decomposition of the other curves shown in Figure 4.2a. The 3.5 h limit corresponds to an upper bound of the period of time during which conditions at the Phoenix landing site would meet the conditions necessary for deliquescence to occur [*Möhlmann*, 2011]. As shown next, this result indicates that liquid brines are much less likely to occur on Mars by the absorption of water vapor from the air than when salts are in direct contact with water ice.

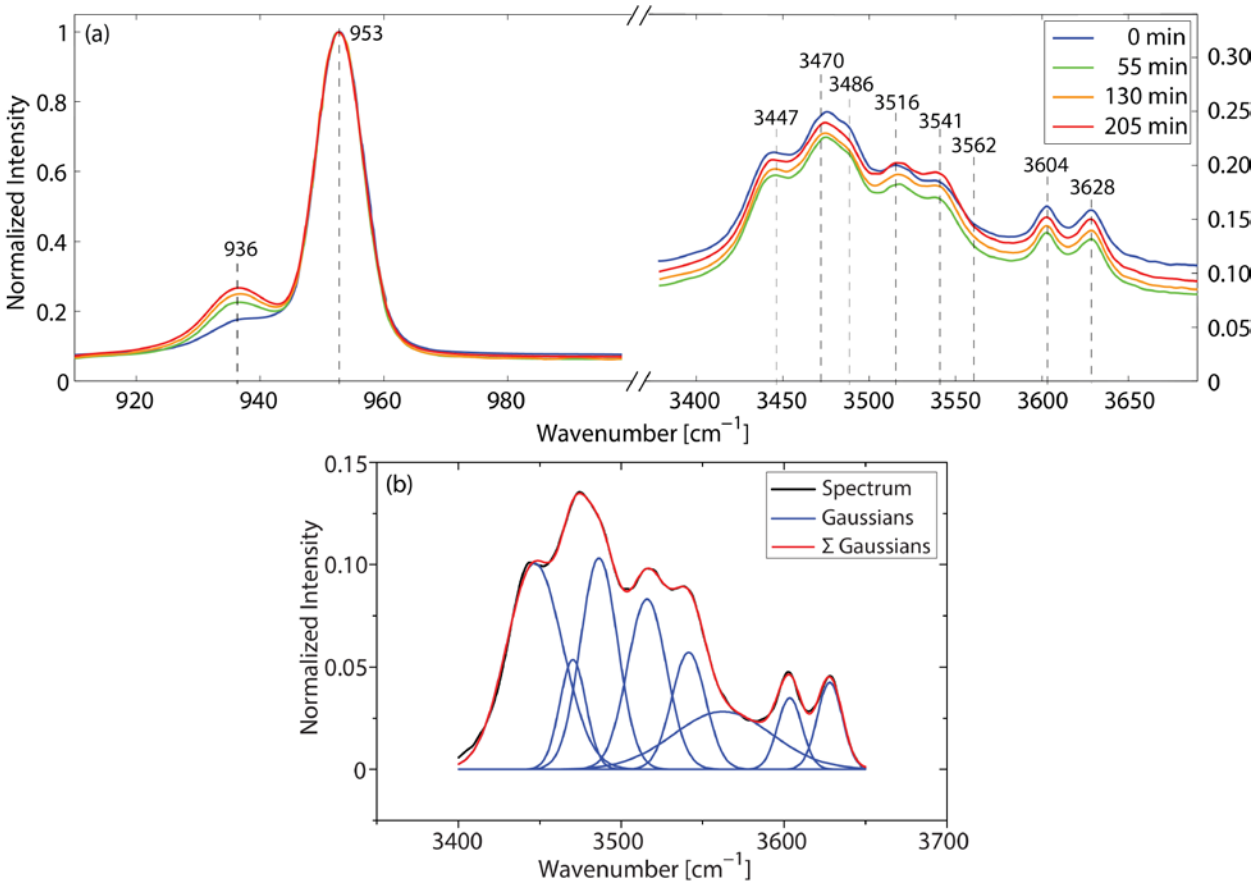

Figure 4.2: (a) Raman spectra of $Ca(ClO_4)_2$•$4H_2O$ exposed to saturated air. The spectra do not show evidence for deliquescence even after the sample has been kept at T = -50°C (about 25°C above $T_e \approx$ -74°C) and *RH* = 100% for 205 min. The values shown in the figure correspond to the spectral peaks of the Gaussian decomposition of the 205 min curve. Analysis of this decomposition indicates that all significant spectral peaks in the O-H stretching region correspond to hydrates. The appearance of a small peak at 936 cm^{-1} indicates a partial change to $Ca(ClO_4)_2$•$8H_2O$. (b) Decomposed O-H vibrational spectrum of the 205 min curve. It shows eight Gaussian components at 3447, 3470, 3486, 3516, 3541, 3562, 3604, and 3628 cm^{-1}, all except one of them with FWHM $\leq$ 50 cm^{-1}. Comparison with Figure 4.1a and Table 4.1 shows that these components indicate the presence of crystalline hydrated $Ca(ClO_4)_2$. $\bar{R}^2 \geq 0.999$.

Figure 4.3a shows the Raman spectra for $Ca(ClO_4)_2$•$4H_2O$ on top of water ice as the sample temperature is raised from below the eutectic temperature to values well above it, corresponding to those reached in the shallow subsurface during the warm season at the Phoenix landing site [*Smith et al.*, 2009; *Rennó et al.*, 2009]. Gaussian decomposition of the O-H vibrational spectrum of the blue curve, representing the spectrum just below the eutectic temperature, is shown in Figure

4.3b. It contains eight narrow peaks with FWHM ≤ 50 cm^{-1} and similar positions as those in Figure 1a, indicating the presence of $Ca(ClO_4)_2$ hydrates. It also contains four peaks with similar widths and positions as those in Figure 1b, indicating water ice. Spectral peaks indicating the presence of liquid water are not present in this spectrum.

In contrast, Figure 4.3c showing the Gaussian decomposition of the spectrum when the sample is about 20°C above the eutectic temperature (red curve in Figure 4.3a) contains the wider spectral peaks characteristic of liquid water. In particular, it shows peaks at 3545 and 3605 cm^{-1} with widths of 160 and 34 cm^{-1}, indicating that a solution has formed in less than ~1.5 h. The spectral peaks at 3060, 3127, and 3356 cm^{-1} indicate that ice is still present below the solution.

Results of experiments with $NaClO_4$ (shown in the Appendix, Figs. A.1 and A.2) are qualitatively similar to those described above. Preliminary results for the O-H band of $Mg(ClO_4)_2$ show similar Gaussians as in Figure 4.3c, indicating the presence of liquid water. Additionally, preliminary results of experiments with icy soil also indicate the formation of liquid brines but at a slower rate. These two cases are more complex and require a more detailed analysis. This will be addressed in a future publication.

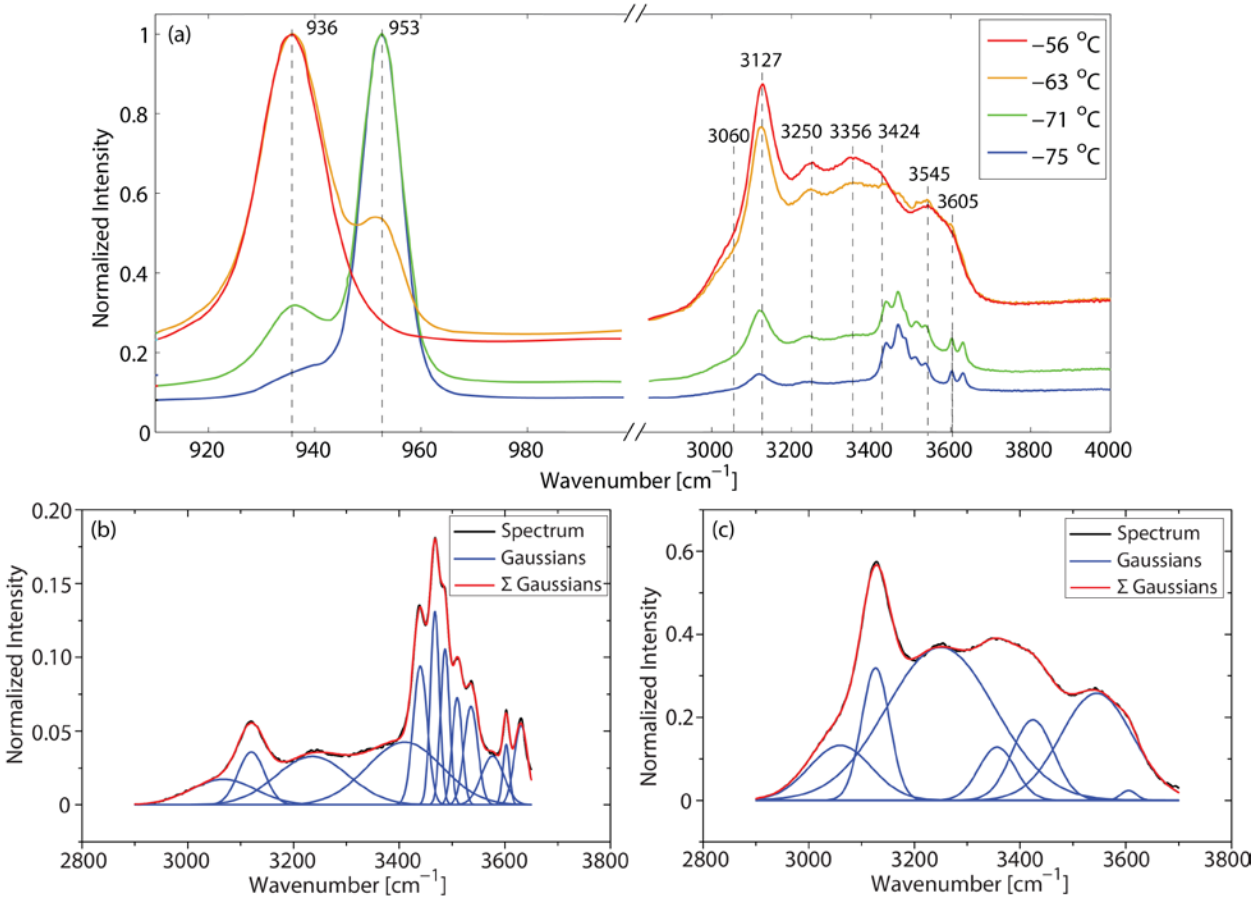

Figure 4.3: (a) Spectra of $Ca(ClO_4)_2$•$4H_2O$ in contact with water ice. The values shown in the figure correspond to the spectral peaks of the Gaussian decomposition of the -56°C curve. The blue and green curves contain spectral peaks indicating the presence of hydrated salt and water ice, similar to those shown in Figure 4.2 (see Table 4.1). The orange and red curves contain broad spectral peaks at ~3545 and 3605 cm^{-1}, indicating the formation of liquid brines by melting of the water ice within ~3 h after the beginning of the experiment. (b) Decomposed O-H vibrational band of the spectrum of $Ca(ClO_4)_2$ in contact with ice at -75°C. It shows 12 Gaussians components: at 3067, 3120, 3236, and 3410 cm^{-1} indicating the presence of ice and at 3440, 3468, 3487, 3510, 3536, 3577, 3602, and 3630 cm^{-1} indicating the presence of crystalline hydrated salt. $\bar{R}^2 \geq 0.999$. (c) Decomposed O-H vibrational band of the spectrum at -56°C. It shows seven Gaussians components at 3060, 3127, and 3356 indicating the presence of ice, at 3250 and 3424 cm^{-1} indicating the presence of liquid water or ice, and at 3545 and 3605 cm^{-1} indicating the presence of liquid water, all except one with a width of FWHM > 50 cm^{-1}. $\bar{R}^2 \geq 0.999$.

4.4 Discussion and Conclusion

The O-H vibrational band of the Raman spectra is excellent for studying the formation of liquid brines at Martian conditions. The change in the O-H spectrum from eight narrow peaks between ~3400 and 3600 cm^{-1} with nearly all of them having the widths of less than 50 cm^{-1} typical of the hydrated perchlorate salts, to the four wide peaks between ~3200 and 3600 cm^{-1} with the widths greater than 100 cm^{-1} typical of liquid water, is an unambiguous indicator of a solution. The changes in the O-H band provide a much clearer indication of the formation of the liquid phase than the changes in the perchlorate band (the ~930 to ~1000 cm^{-1} region of the spectrum) because it is less sensitive to changes in the salt hydration and the concentration of the solution [*Zhang and Chan*, 2003; *Miller and Macklin*, 1985]. Thus, observations of changes in the O-H vibrational band could aid the search for liquid brines on Mars.

The results described above indicate that perchlorate salts in contact with ice can form liquid brines during the short periods of the diurnal cycle during which the ground temperatures are above the salts' eutectic temperatures, whereas when atmospheric water vapor is the only source of water bulk deliquescence is too slow to occur. We conclude that liquid brines are likely to form in the shallow subsurface where water ice exists, since the heating of the ground by solar radiation causes the temperature of the shallow Martian subsurface to exceed the eutectic temperature of many salts found on Mars, while the top regolith inhibits sublimation and evaporation. The formation of liquid brines in the shallow subsurface resolves the apparent inconsistency between observational evidence for liquid brines on Mars and the slow kinetics of deliquescence on a cold and dry planet.

The results of our experiments suggest that the spheroids observed on a strut of the Phoenix lander formed on water ice splashed during landing [*Smith et al.*, 2009; *Rennó et al.*, 2009]. They

also support the hypothesis that “soft ice” found in one of the trenches dug by Phoenix was likely frozen brine that had been formed previously by perchlorates on icy soil. Finally, our results indicate that liquid water could form on the surface during the spring where snow has been deposited on saline soils [*Martínez et al.*, 2012; *Möhlmann*, 2011]. These results have important implications for the understanding of the habitability of Mars because liquid water is essential for life as we know it, and halophilic terrestrial bacteria can thrive in brines [*Mikucki et al.*, 2009; *Boetius and Joye*, 2009].

CHAPTER V

Formation and Persistence of Brine on Mars: Experimental Simulations throughout the Diurnal Cycle at the Phoenix Landing Site

This chapter is published: Fischer, E., Martínez, G. M., & Rennó, N. O. (2016), Formation and persistence of brine on Mars: experimental simulations throughout the diurnal cycle at the Phoenix landing site. *Astrobiology*, *16*(12), 937-948.

Abstract

In the last few years, water ice and salts capable of melting this ice and producing liquid saline water (brine) have been detected on Mars. Moreover, indirect evidence for brine has been found in multiple areas of the planet. Here, we simulate full diurnal cycles of temperature and atmospheric water vapor content at the Phoenix landing site for the first time and show experimentally that, in spite of the low Mars-like chamber temperature, brine forms minutes after the ground temperature exceeds the eutectic temperature of salts in contact with water ice. Moreover, we show that the brine stays liquid for most of the diurnal cycle when enough water ice is available to compensate for evaporation. This is predicted to occur seasonally in areas of the polar region where the temperature exceeds the eutectic value and frost or snow is deposited on

saline soils, or where water ice and salts coexist in the shallow subsurface. This is important because the existence of liquid water is a key requirement for habitability.

5.1 Introduction

The discovery of water ice and perchlorates at the surface and in the shallow subsurface of Mars is interesting because they could produce liquid saline water (brine) under Mars' present-day environmental conditions. Water ice was discovered in the shallow subsurface of polar and midlatitude regions [*Boynton et al.*, 2002; *Feldman et al.*, 2002; *Mitrofanov et al.*, 2002; *Byrne et al.*, 2009; *Smith et al.*, 2009]. Salts capable of melting this ice at Mars' present-day environmental conditions and producing brine were discovered in the polar and equatorial regions [*Hecht et al.*, 2009; *Glavin et al.*, 2013; *Ming et al.*, 2014], suggesting that they are distributed globally. Evidence for salt hydrates and brine has been found in regions ranging from polar to equatorial latitudes [*Rennó et al.*, 2009; *Cull et al.*, 2010a; *McEwen et al.*, 2011; *Martín-Torres et al.*, 2015; *Ojha et al.*, 2015], in spite of the Martian air [*Lewis et al.*, 1999] and top regolith [*Meslin et al.*, 2013] being extremely dry and bulk deliquescence (brine formation by absorption of water vapor only) at Mars' low temperatures being too slow to explain the observed phenomena [*Fischer et al.*, 2014].

We studied experimentally the formation and the persistence of brine throughout the diurnal cycle at the Phoenix landing site using Raman scattering spectroscopy and imaging. A previous study suggests that brine formation from water ice is the most likely mechanism to produce liquid water within the diurnal cycle [*Fischer et al.*, 2014].We focus on the formation of brine by the contact of either surface or subsurface water ice with $Ca(ClO_4)_2$ because this salt is likely present at the Phoenix landing site [*Hecht et al.*, 2009; *Kounaves et al.*, 2014] and at Gale

Crater [*Glavin et al.*, 2013], suggesting that it is ubiquitous on Mars [*Kounaves et al.*, 2014]. Furthermore, the eutectic temperature of $Ca(ClO_4)_2$ is extremely low (T_e ~ 199 K) [*Marion et al.*, 2010], and it changes phases at similar environmental conditions as a salt mixture closely matching the individual cation/anion concentrations found in the regolith of the Phoenix landing site on Mars' polar region [*Nuding et al.*, 2015]. Finally, we focus on $Ca(ClO_4)_2$ because liquid solutions of other perchlorate salts have already been studied in detail [*Chevrier et al.*, 2009]. It is likely that perchlorates have been deposited at the Phoenix landing site by atmospheric processes and concentrated into patches at the surface and in the shallow subsurface by freeze-thaw cycles *[Rennó et al.*, 2009; *Cull et al.*, 2014]. Our study focuses on the simplest process, the interaction of salts with water ice. This is the first step for the full understanding of brine formation on Mars. In the future, we plan to study the formation of brine by the interaction of saline soils with water ice.

Results of four comprehensive laboratory experiments are discussed in this article. The first three experiments were designed to investigate the formation of bulk brine on the surface of Mars' polar region, such as in the material exposed in a shallow trench (Dodo-Goldilocks) excavated by the Phoenix robotic arm on Sols 18-19 of the mission (Smith et al., 2009). The fourth experiment investigates the evolution of $Ca(ClO_4)_2$ salt subjected to a lower-amplitude diurnal temperature cycle like that expected on the struts of the Phoenix lander where surface/shallow-subsurface material was splashed and formed spheroids [*Rennó et al.*, 2009].

The Michigan Mars Environmental Chamber (MMEC) [*Fischer et al.*, 2014] is used to simulate the environmental conditions throughout the full diurnal cycle of each experiment reported in this article. Sol 19 of the Phoenix mission is chosen as the baseline because ice was unveiled at a depth of ~5 cm and removed with little effort around this sol [*Smith et al.*, 2009],

suggesting that it was likely frozen brine [*Rennó et al.*, 2009; *Cull et al.*, 2010a], which is much softer than freshwater ice.

5.2 Experimental Setup

All experiments reported in this study were conducted in the MMEC, a cylindrical chamber with internal diameter of 64 cm and length of 160 cm. The MMEC is capable of simulating temperatures ranging from 145 to 500 K, CO_2 pressures ranging from 10 to 10^5 Pa, and the entire range of relative humidity at the Phoenix landing site [*Fischer et al.*, 2014].

The first experiment was designed to study the formation of brine when salt is placed in contact with water ice, as it occurs when frost or snow are deposited on salty soil crusts. Distilled water was placed in a 0.3 cm^3 cylindrical sample holder at laboratory ambient conditions, and the temperature of the sample holder was lowered to ~190 K, about 9 K below the eutectic temperature of $Ca(ClO_4)_2$, to freeze the sample. Then, a thin (<2 mm) layer of salt crystals with typical particle diameters <300 μm was placed on the top of the ice. Particles of this size can move easily, accumulate in low topographical features, and then be buried because they are the most easily transported by saltation [*Kok and Rennó*, 2009]. In addition, layers of salt this thin were used because this thickness is within the penetration depth of the laser; thus the onset of the formation of brine anywhere in the sample can be detected. Our results are not sensitive to particle size because melting starts in the interface between salt crystals and ice, and Raman spectroscopy is capable of detecting its onset on the surfaces of the salt crystals. Next, the chamber pressure was reduced to 800 Pa, the chamber's Earth air atmosphere was replaced by dry CO_2, and then the sample temperature and the frost point temperature (of the MMEC's atmosphere) were continuously adjusted to follow those of the Martian diurnal cycle starting at midnight.

The ground temperature and frost point temperature at the Phoenix landing site on Sol 19 (Fig. 5.1) were obtained by a combination of numerical modeling and measurements (see the Appendix for details).

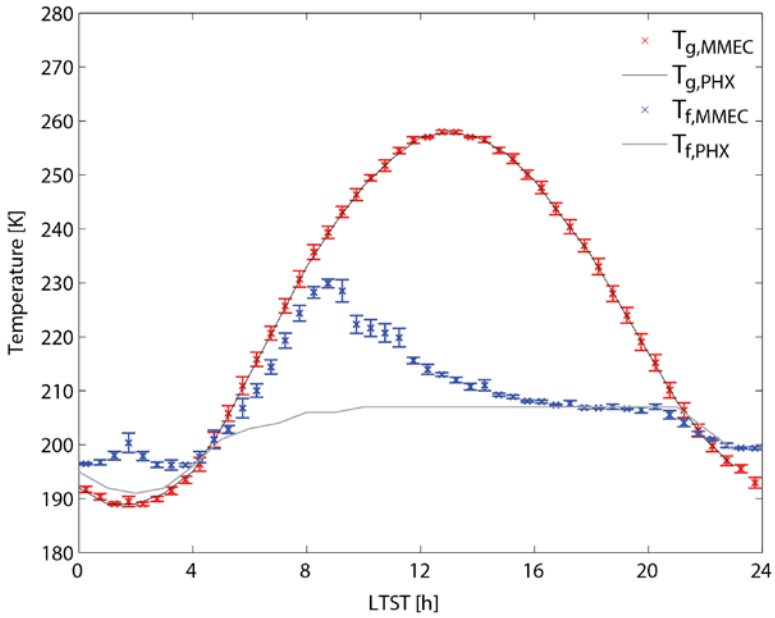

Figure 5.1: Environmental conditions on Sol 19, when "soft ice" was unveiled by the Phoenix robotic arm in the Dodo-Goldilocks trench. The black and gray lines represent values from numerical simulations of the ground temperature and frost point of the surrounding air at the Phoenix landing site, while red and blue crosses represent the temperature and frost point measured inside the MMEC. The ground temperature first exceeds the $Ca(ClO_4)_2$ eutectic value (199 K) at 04:32, about 5 min before the first visual evidence for the formation of brine in the MMEC. Detailed calculations of the environmental conditions on this sol are provided in the Appendix.

The experimentally (MMEC) simulated ground temperature (red crosses) closely matches values inferred from the Phoenix measurements (black curve), while the frost point temperature simulated by the MMEC (blue crosses) is higher than the values estimated (gray line) between 05:15 and 16:00 LTST (hereafter time always refers to local true solar time, LTST). This difference is caused by the fact that water ice and brine are significant sources of water vapor. Indeed, evaporation increases the frost point temperature as soon as brine forms. However, since the air around salt

crystals in contact with the ice is always close to the saturation value, this difference does not affect our results significantly [*Fischer et al.*, 2014]. In particular, frost points simulated experimentally and modeled numerically start to diverge at 05:15, about 45 min after the first visual evidence for the formation of brine (details in Section 5.3). At that time, the flow of water vapor into the chamber was stopped, while the flow of dry CO_2 was increased to mitigate the increase in frost point temperature. Still, evaporation from the brine and sublimation from the remaining water ice continued to increase the frost point until ~08:00.

To investigate the sensitivity of the results of this first experiment to the initial conditions (e.g., sample state, local time), two additional experiments were conducted. In particular, the second experiment started with liquid brine, while the third experiment started with frozen brine. In the second experiment, $Ca(ClO_4)_2$ was mixed with distilled water at ambient conditions until the salt had been completely dissolved (the salt amount and sample characteristics were similar to those in the first experiment). The resulting solution was placed in the sample holder, the chamber pressure was adjusted to 800 Pa, and the chamber air was replaced by CO_2. Then, the temperature of the sample holder and the MMEC frost point temperature were adjusted continuously to follow those of the Martian diurnal cycle between 13:45 and 06:30 shown in Fig. 5.2.

The third and fourth experiments started with frozen brine as the initial condition. In the third experiment, brine was produced as in the second experiment. Then, the temperature of the solution was lowered rapidly to values <150 K to freeze the brine and mitigate evaporation. Then, the chamber pressure was adjusted to 800 Pa, and the chamber air was replaced by CO_2. The temperature was kept below 150 K for at least 3.5 h to ensure freezing of the sample. Then, the simulation of the diurnal cycle started, following the temperature and frost point values shown in Fig. 5.3. In the fourth experiment, the MMEC atmosphere was kept saturated by the MMEC

control system throughout the experiment to simulate the humidity above the ground ice exposed underneath the Phoenix lander. In this experiment, the temperature of the sample was forced to follow that corresponding to the diurnal cycle on the strut shown in Fig. 5.4.

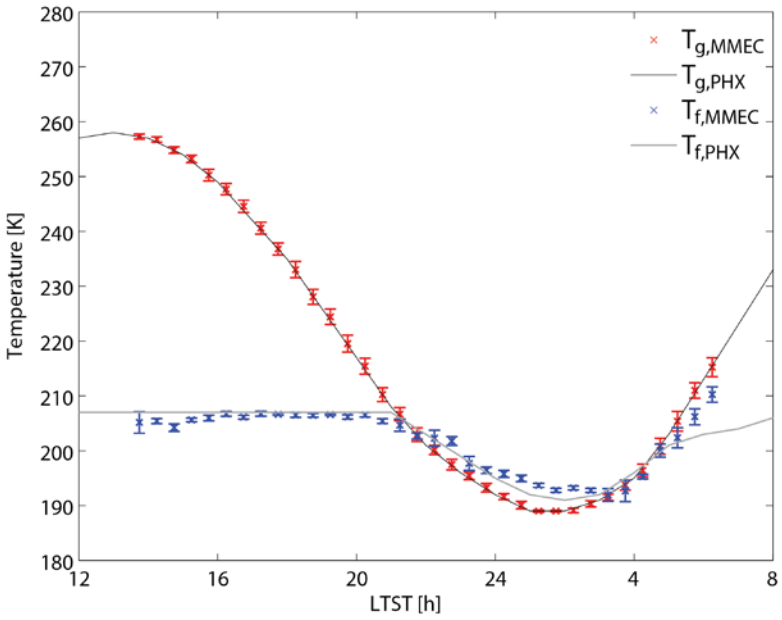

Figure 5.2: As in Fig. 5.1, but for the second experiment. To ensure similar sample conditions as in the first experiment, the second experiment started with brine at the beginning of crust formation at 13:45. The experiment ended at 06:30 of the next sol, about 2 h after the sample temperature exceeded the eutectic value.

In all experiments, the temperature of the sample holder was adjusted in 1 K increments to force it to follow the Martian diurnal cycle. The sample temperature, the chamber pressure, and the chamber frost point temperature were recorded at 1 Hz. Raman spectra of the sample and color images were acquired every 10 min. Gaussian decomposition of each spectrum was conducted during the entire diurnal cycles to search for changes in the phase of the samples. The wavenumber and full width half maximum (FWHM) of various spectral peaks are used to determine the phase of the samples by comparing them with reference values for crystalline perchlorate (salt), water ice, and liquid water [*Zhang and Chan*, 2003; *Fischer et al.*, 2014].

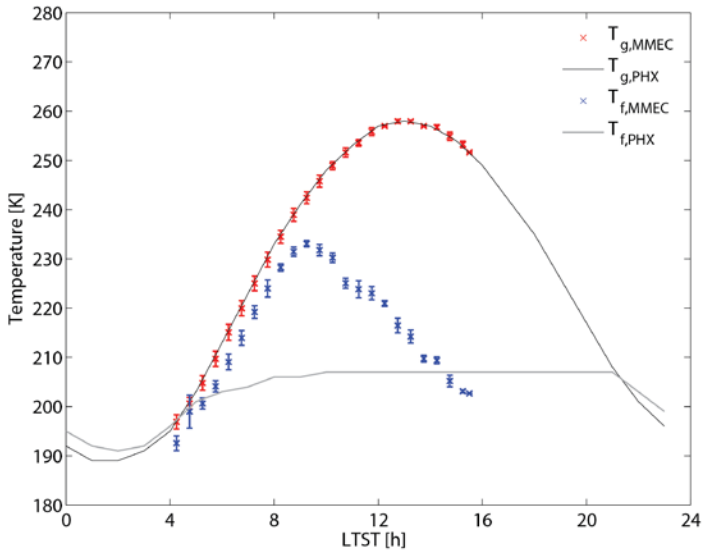

Figure 5.3: As in Fig. 5.1, but starting with a mix of water ice and calcium perchlorate at 04:00. Similar to the first experiment, the MMEC closely simulates the temperature in the trench (red crosses), but it overshoots the frost point temperature values inferred from the Phoenix measurements between 06:00 and 15:00 (blue crosses).

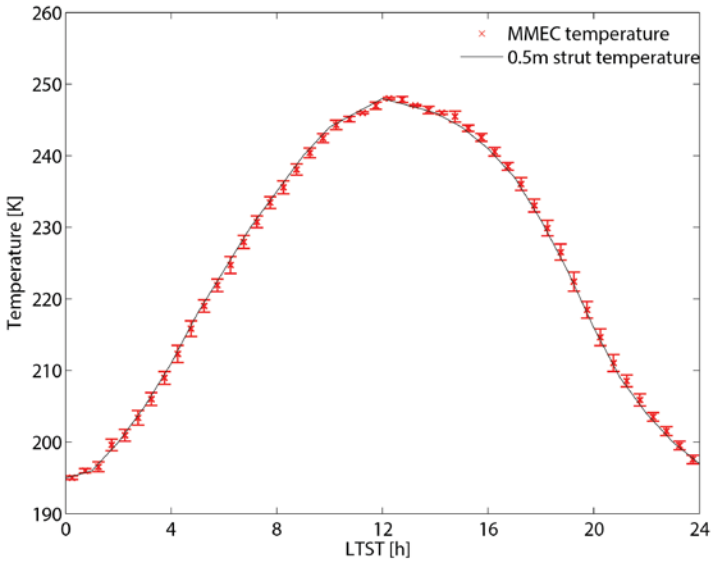

Figure 5.4: Sol 19 temperature at 0.5 m above the ground (the height of place on the Phoenix strut where spheroids were observed) at the Phoenix landing site. The black curve represents the diurnal evolution of the temperature (0.5 m above the surface), while red crosses represent the temperature experimentally simulated in the MMEC. The frost point temperature was not simulated in this experiment. The diurnal temperature cycle at 0.5 m height has lower amplitude than at the ground, with higher minimum and lower maximum temperatures. This causes the brine to stay liquid for most of the diurnal cycle.

Since our study focuses on the formation of bulk quantities of brine, images in the visible range of the spectrum (color images) are used as supporting evidence for the detection of the liquid phase. This is necessary because when brine starts to form the sample is heterogeneous, containing brine, crystalline salt, and water ice. Thus, spectral features of one particular component of the mixture might dominate the Raman spectrum because the diameter of the sample holder (~10 mm) is larger than that of the laser beam (~3 mm) of the Raman spectrometer.

5.3 Results

5.3.1 First Experiment: Diurnal Cycle of Salt Deposited on Ice at Martian Polar Surface Conditions

In the first experiment, the Gaussian decomposition of the Raman spectra taken at 00:10 (Figs. 5.5 and 5.6), when the temperature is below the eutectic value (Fig. 5.1), contains spectral peaks that indicate the presence of crystalline $Ca(ClO_4)_2$ hydrates and water ice (Table 5.1). At 05:15, the spectral peaks of crystalline $Ca(ClO_4)_2$ hydrates are still present, but the signal from water ice is stronger than at 00:10, with the 3068 cm^{-1} spectral peak of ice appearing and the other spectral peaks of ice intensifying (Fig. 5.5 and Table 5.1). At this time, spectral peaks indicating the presence of liquid water are not observed, even though the first visual evidence (color image) for the formation of brine occurs at 04:37, about 5 min after the temperature exceeds the eutectic value for $Ca(ClO_4)_2$ (Fig. 5.1). This occurs because, when ice starts to melt, $Ca(ClO_4)_2$ hydrates absorb meltwater (Fig. 5.7b) and become more translucent, increasing the signal of the ice below the salt. The heterogeneity of the sample in combination with the fixed position of the Raman laser may also lead to slight variations in the time when the liquid water peaks start to appear. At 08:00, the decomposition of the spectrum indicates the presence of brine; in particular, the 3578 cm^{-1}

spectral peak (Table 5.1) indicates the presence of brine unambiguously, which is consistent with the shift in the perchlorate peak from 954 to 936 cm^{-1} (Gough et al., 2011) (Fig. 5.6). The 3129 cm^{-1} peak at 08:00 indicates that ice (Table 5.1) is also present. No signal of crystalline $Ca(ClO_4)_2$ hydrates exists at this time, which is consistent with the lack of salt crystals in the image of the sample (Fig. 5.7c). By 11:00, all water ice peaks have disappeared, and the entire sample is liquid (Fig. 5.7d). As the temperature rises, water evaporation increases the concentration of the solution. At 13:45, a thin salt crust formed on the top of the sample, indicating that the brine solution became at least partially salt-saturated (Fig. 5.7e). The Gaussian decomposition of the spectrum taken at this time contains only the spectral peaks indicative of brine because the signal from the thin crust is insignificant. As the experiment progresses, evaporation continues and the salt crust thickens. The Gaussian decomposition of the spectrum taken at 23:55, when the temperature is already below the eutectic value (Fig. 5.1), indicates the presence of a salt crust and frozen brine below it (Table 5.1). At this time, the sample was composed almost entirely of crystalline salt hydrates because most of the bulk water originally in the sample had been lost by sublimation and evaporation (Fig. 5.7f). Any remaining solution below was saturated.

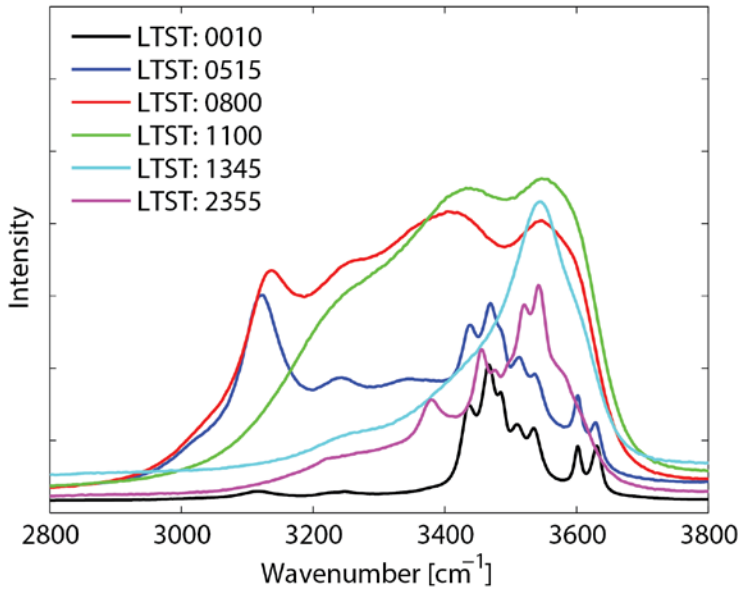

Figure 5.5: Raman spectra in the O-H stretching band throughout the full diurnal cycle shown in Fig. 5.1 (first experiment). The wavenumber and FWHM of the Gaussian components of each spectrum are shown in Table 5.1. The appearance of the broad peak at 3578 cm^{-1} in the spectrum taken at 08:00 clearly indicates the presence of liquid solution.

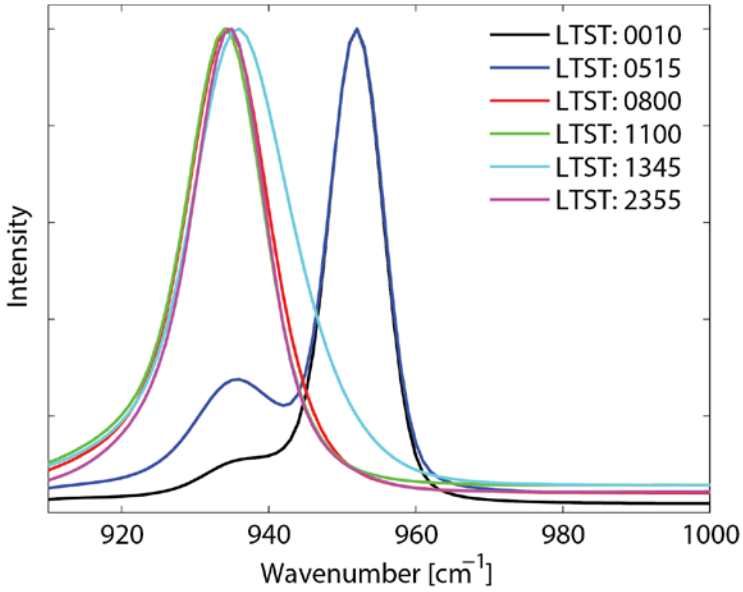

Figure 5.6: As in Fig. 5.5, but for the perchlorate vibration band. In the spectrum taken at 08:00, the ~954 cm^{-1} peak of crystalline $Ca(ClO_4)_2 \cdot 4H_2O$ shifted toward ~936 cm^{-1}, consistent with the presence of liquid solution. After the sample dries out at the end of the experiment, this peak does not shift back, indicating that it is not an unambiguous indicator for the presence of liquid brine.

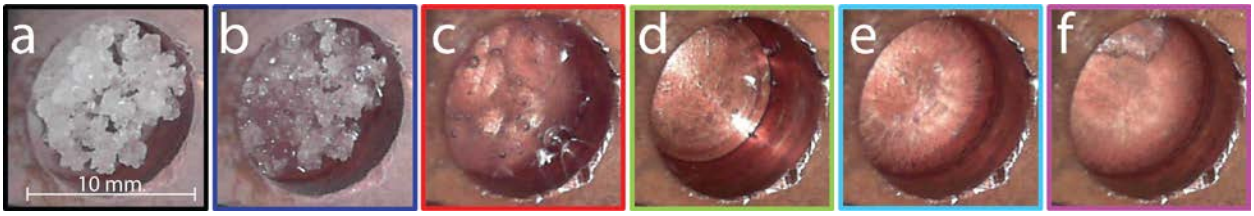

Figure 5.7: Images of the sample color-coded according to the spectra shown in Figs. 5.5 and 5.6. (a) Salt on top of ice at the start of the experiment at 00:10 when the temperature is below the eutectic value. (b) Evidence for brine at 05:15, shortly after the eutectic temperature is exceeded. (c) Salt has completely dissolved, but water ice is still present at 08:00. (d) Only brine is present at 11:00. (e) Evidence for the presence of a salt crust at 13:45. The salt crust can be distinguished from the liquid by its different reflective properties. (f) Mainly crystalline salt hydrates with frozen brine below it at end of the diurnal cycle at 23:55.

5.3.2 Second Experiment: Effect of a Subsequent Diurnal Cycle

To investigate the sensitivity of the results of the experiments to initial conditions (sample state) and to investigate what happens in successive diurnal cycles, a second experiment was performed starting with brine at 13:45 (Fig. 5.2), the time that the salt crust started to form in the first experiment, and ending on the next sol at 06:30. As explained next, evaporation of the initial brine during the afternoon hours caused the sample to dry substantially and to become mostly crystalline salt hydrates by midnight. The Raman spectrum of the O-H region (Fig. 5.8) shows this change by the transformation of the smooth curve representing salt-saturated brine at 13:45 to the narrow peaks indicating the presence of crystalline salt by midnight (Table 5.2). The perchlorate peak of the spectrum does not change considerably throughout this transformation (Fig. 5.9), indicating that the O-H spectrum is a better indicator for phase changes of the sample. Continued cooling of the sample below the eutectic temperature in this second experiment resulted in whitish solid material (Figs. 5.10b-5.10d), similar to the material found by the Phoenix lander in a shallow trench [*Rennó et al.*, 2009; *Cull et al.*, 2010a]. Brine was not detected when the temperature

exceeded the eutectic value on the next sol (Table 5.2; Figs. 5.10e-5.10f), indicating that the sample had extremely low water content.

Reference Spectra						First Experiment: Sol 19 Diurnal Cycle from Salt and Water Ice											
Salt		Ice		Water		LTST 0010		LTST 0515		LTST 0800		LTST 1100		LTST 1345		LTST 2355	
Peak	FWHM	Peak	FWHM	Peak	FWHM	Peak	FWHM	Peak	FWHM	Peak	FWHM	Peak	FWHM	Peak	FWHM	Peak	FWHM
		3046	99					3068	143								
		3115	57			3115	81	3122	60	3129	56						
		3227	206	3230	217	3249	113	3210	148	3219	280	3282	268	3256	219		
		3336	56													3311	271
		3399	140	3420	218	3437	147	3381	226	3434	224	3454	178	3495	249	3389	66
3446	37					3437	27	3440	31							3456	38
3471	20					3467	23	3470	24								
3487	24					3487	15	3488	16							3496	31
3515	29					3509	25	3512	28							3520	19
				3540	206					3578	114	3582	125	3555	106		
3542	25					3536	23	3539	23							3543	17
3564	70					3560	155	3569	122							3546	132
3603	17					3602	13	3602	15								
				3620	109												
3628	19					3630	18	3629	19								

Table 5.1: Gaussian components of the O-H stretching band of the reference Raman spectra of $Ca(ClO_4)_2 \cdot 4H_2O$, water ice, and liquid water (left) [*Zhang and Chan*, 2003; *Fischer et al.*, 2014], as well as of the Raman spectra shown in Fig. 5.5 (right). Each column contains the wavenumber and FWHM of each spectral peak. The values of the spectral peaks and their FWHM are color-coded to indicate the presence of salt (black), water ice (blue), either water ice or liquid water (gray), and liquid water (red). The Gaussian components of the spectrum taken at 00:10, when the temperature is below the eutectic value, contain spectral peaks of hydrated perchlorate salt and water ice. In spite of the temperature being above the eutectic value and the image of the sample indicating that the ice starts to melt at 04:37, spectral peaks corresponding to liquid water are not observed at 05:15. The fact that the signal of the ice at the bottom of the sample is stronger at this time (the appearance of a shoulder caused by the 3068cm^{-1} ice spectral peak and a general increase in intensity of all spectral peaks of ice, as shown in Fig. 5.5) provides indirect evidence that the ice has started to melt. The ice signal likely increases because the salt becomes more translucent when it absorbs liquid water. At 08:00 the Raman spectrum indicates the presence of liquid water unambiguously. The spectral peak at ~3129 cm^{-1} indicates that water ice is still present, but by 11:00 this peak has disappeared. Evaporation of water causes the salt concentration of the solution to increase continuously until a salt crust forms at 13:45 (Fig. 5.7e). At this time, the Gaussian components still contain spectral peaks corresponding to brine because the signal from the thin crust is weak. Evaporation thickens the salt crust until crystalline calcium perchlorate hydrates dominate the spectrum at 23:55. The brine freezes below the salt crust when the temperature decreases below the eutectic value. The Gaussian components fit the full measured spectrum with accuracy $\bar{R}^2 \geq 0.98\%$.

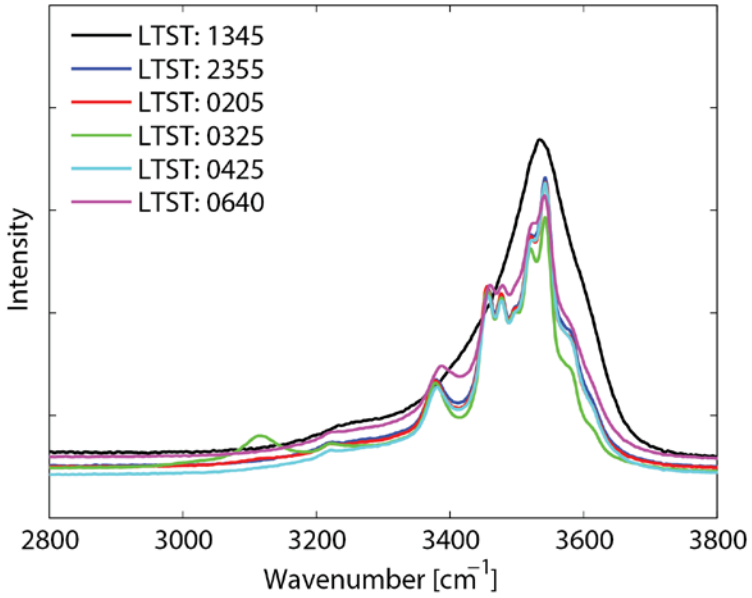

Figure 5.8: Raman spectra in the O-H stretching band throughout the partial diurnal cycle shown in Fig. 5.2 (second experiment). Gaussian components of each spectrum are shown in Table 5.2. A change from the smooth curve representing salt-saturated brine (black) to the narrow peaks indicating crystalline salt is observed.

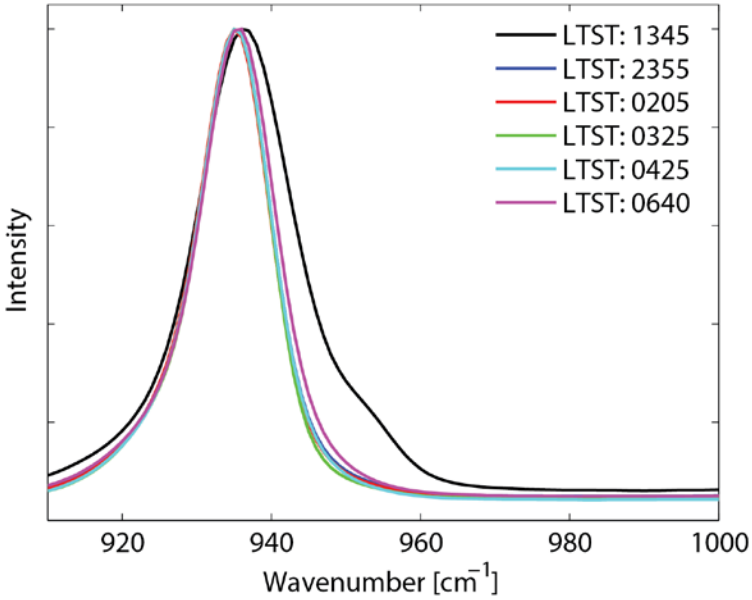

Figure 5.9: As in Fig. 5.8, but for the perchlorate vibration band. This experiment starts with brine and ends with hydrated calcium perchlorate. The perchlorate peak remains at 936 cm^{-1} during the entire experiment.

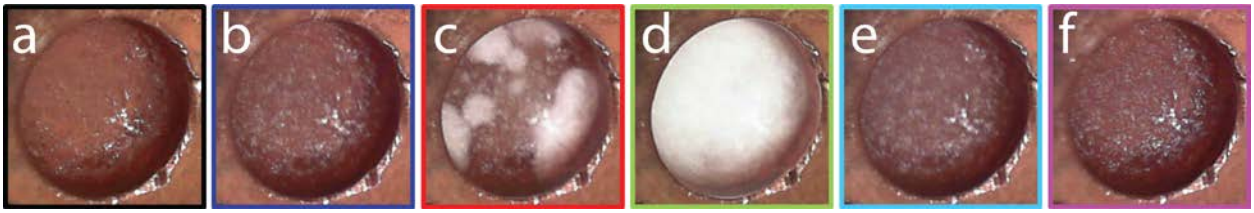

Figure 5.10: Images of the sample color-coded according to spectra shown in Figs. 5.8 and 5.9. (a) Evaporation of water causes a salt crust to start to form at 13:45. (b) Mainly crystalline perchlorate hydrates at the end of the diurnal cycle at 23:55. (c) The frozen brine starts to become white at 02:05. (d) Whitish frozen brine at 03:25, similar to the material found in the Dodo-Goldilocks trench. (e) The sample becomes translucent again after the eutectic temperature is exceeded at 04:25 and the remaining ice partially melts. (f) Wet calcium perchlorate hydrates at 06:40, with no evidence for brine. The fact that brine is not observed even 2 h after the eutectic temperature has been exceeded indicates that the sample lacks bulk water (frozen brine at 03:25 is whitish because it is nearly salt-saturated and therefore lacks bulk water).

5.3.3 Third Experiment: Diurnal Cycle of Initially Frozen Brine at Martian Polar Surface Conditions

To further analyze the impact of the initial state of the sample on the results, a third experiment starting with frozen brine instead of salt on top of ice (first experiment) or brine (second experiment) was conducted. This experiment covered the portion of the Sol 19 diurnal cycle between 04:00 and 15:30 (Fig. 5.3). This third experiment with frozen brine as the initial sample might be indicative of the evolution of the material unveiled at the Dodo-Goldilocks trench, while the first experiment with salt on top of ice as the initial sample represents the evolution of a soil salt crust covered by snow [*Whiteway et al.*, 2009] or frost [*Smith et al.*, 2009]. The evolution of the sample throughout diurnal cycles is similar in the first and third experiments (Fig. 5.11 and Table 5.3). However, a significant difference between them is that, at the beginning of the third experiment, when the temperature was still below the eutectic value and brine (liquid) was not present in the sample, the perchlorate peak is now located at 936 cm^{-1}, suggesting a different hydration state (Fig. 5.12). Consequently, in this case, the perchlorate peak in the Raman spectrum

at 936 cm^{-1} is the result of the presence of only crystalline salt hydrates, indicating that this peak is an ambiguous indicator of the presence of brine. Throughout the diurnal cycle, the sample underwent similar changes as those observed in the first experiment: the frozen brine melted when the eutectic temperature was exceeded, and evaporation of water from the brine produced a salt crust on the top of the sample (Fig. 5.13). However, both brine and the salt crust formed about 45 min later in the third experiment than in the first.

Reference Spectra						Second Experiment: Sol 19–20 Partial Diurnal Cycle from Liquid Brine											
Salt		Ice		Water		LTST 1345		LTST 2355		LTST 0205		LTST 0325		LTST 0425		LTST 0640	
Peak	FWHM	Peak	FWHM	Peak	FWHM	Peak	FWHM	Peak	FWHM	Peak	FWHM	Peak	FWHM	Peak	FWHM	Peak	FWHM
		3046	99														
		3115	57									3114	59				
		3227	206	3230	217			3223	47	3222	27	3223	24	3222	30	3224	30
		3336	56			3328	250	3387	340	3387	376	3355	433	3388	359	3395	338
		3399	140	3420	218	3413	83	3387	56	3387	58	3383	52	3388	57	3395	61
3446	37							3459	37	3457	33	3458	35	3459	37	3464	43
3471	20							3478	12	3478	12	3478	12	3479	13	3481	12
3487	24							3496	25	3495	24	3496	25	3496	23	3497	23
3515	29							3520	23	3520	24	3520	23	3520	25	3520	28
				3540	206	3539	136										
3542	25							3543	21	3543	21	3543	21	3543	21	3543	21
3564	70							3568	49	3569	46	3573	45	3567	52	3558	60
3603	17							3607	65	3608	57	3617	32	3603	75	3591	84
				3620	109												
3628	19																

Table 5.2: As in Table 5.1, but for the second experiment. The Gaussian decomposition of the spectrum at 13:45 shows a liquid water peak at 3539 cm^{-1}, indicating that the sample is brine when the salt crust forms (see Fig. 5.10a). Another peak at 3328 cm^{-1} seems to indicate the presence of ice, but this is unlikely because the temperature at 13:45 is the warmest of Sol 19, about 60 K above the eutectic point, and the sample was initially prepared as a saturated solution. A peak at a lower wavenumber (closer to the 3230 cm^{-1} peak in the water reference) with a slightly different FWHM leads to a similar accuracy for the complete decomposition. We believe that this is caused by inaccuracies in peak positions when wide FWHM values occur in the Gaussian decomposition, as it is the case for the 3328 cm^{-1} peak in this decomposition. Ambiguities in the detection of phase changes using Gaussian decomposition will be described in more detail in a future study. Only salt and ice peaks are present at 23:55 because most of the water in the sample has evaporated and the remaining solution is frozen (see Fig. 5.10b). The Gaussian decomposition does not change until 03:25, when an additional ice peak at 3114 cm^{-1} appears (see Fig. 5.8). At this time the frozen solution in the sample is whitish and opaque, similar to the material found in the Dodo-Goldilocks trench by the Phoenix lander (Fig. S2). At 04:25 the peak at 3114 cm^{-1} and the white color disappear (Fig. 5.10e). This happens when the temperature exceeds the eutectic value. At 06:40, about 2 h after exceeding the eutectic temperature, no peak indicating brine is detected, suggesting that the frozen solution is whitish because it is nearly salt-saturated. Most of the water substance has either evaporated or sublimated, and not enough water is available to form brine in a subsequent diurnal cycle.

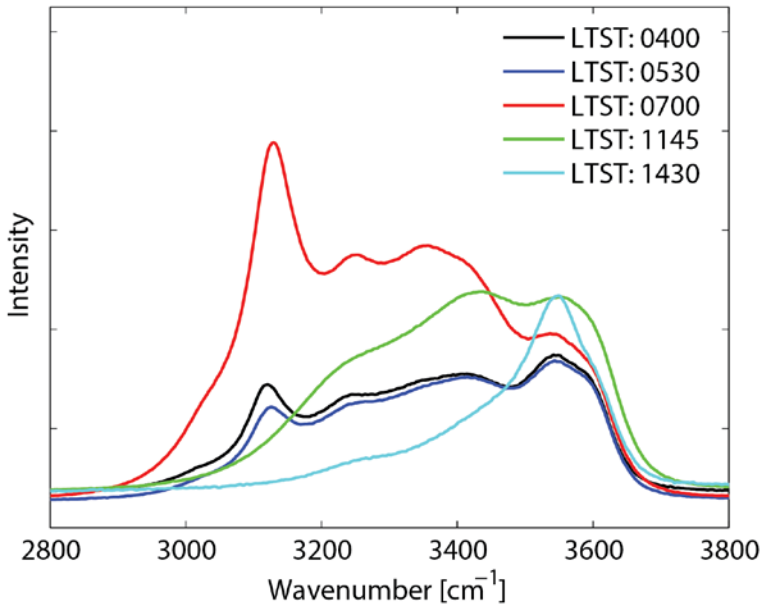

Figure 5.11: Raman spectra in the O-H stretching band throughout the partial diurnal cycle shown in Fig. 5.3 (third experiment). Gaussian components of each spectrum are shown in Table 5.3.

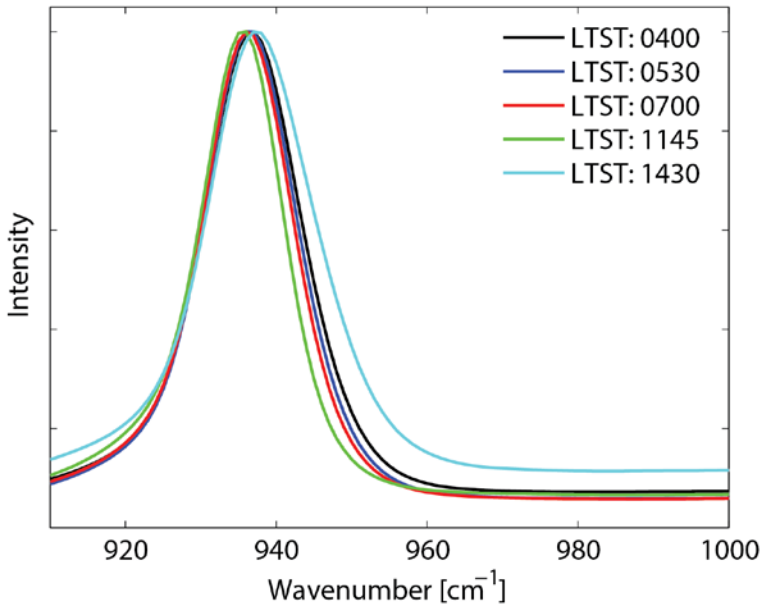

Figure 5.12: As in Fig. 5.11, but for the perchlorate vibration band. The perchlorate peak at 936 cm^{-1} is at a similar location for both, the mix of water ice and salt (frozen brine) (black curve) and brine (green and cyan curves), indicating that it is not an unambiguous indicator of brine.

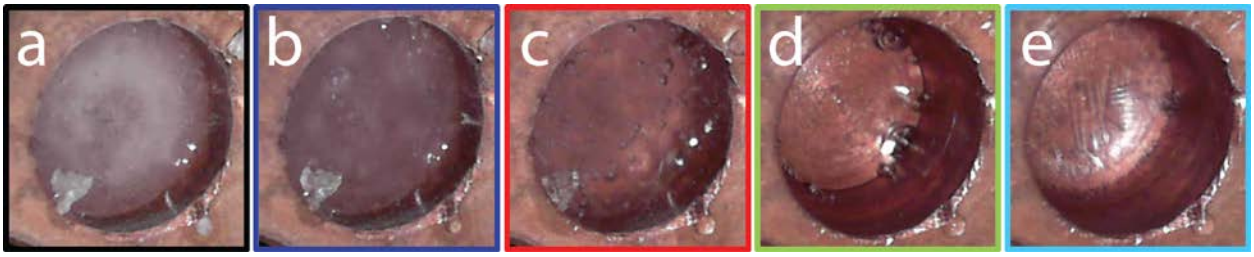

Figure 5.13: Images of the sample color-coded according to the spectra shown in Figs. 5.11 and 5.12. (a) Frozen mix of water ice and perchlorate salt at 04:00 at 195 K after preparing the sample at 150 K. The darker color compared to the whitish frozen brine in the second experiment shown in Fig. 5.10d is likely due to a larger water content in the frozen mix, consistent with the observation of brine later in the diurnal cycle when the eutectic temperature is exceeded. (b) Brine forms at 05:30, after the temperature exceeds the eutectic value. (c) Brine on top of frozen brine at 07:00. (d) Brine only at 11:45. (e) Start of crust formation at 14:30.

Reference Spectra						Third Experiment: Sol 19 Partial Diurnal Cycle from Frozen Brine									
Salt		Ice		Water		LTST 0400		LTST 0530		LTST 0700		LTST 1145		LTST 1430	
Peak	FWHM	Peak	FWHM	Peak	FWHM	Peak	FWHM	Peak	FWHM	Peak	FWHM	Peak	FWHM	Peak	FWHM
		3046	99			3051	128	3053	130	3075	156				
		3115	57			3119	56	3123	57	3128	61				
		3227	206	3230	217	3256	247	3264	265	3229	189	3274	260	3274	248
		3336	56							3346	50				
		3399	140	3420	218	3424	159	3428	156	3407	194	3455	187	3498	240
3446	37														
3471	20														
3487	24														
3515	29														
				3540	206	3559	119	3561	123	3573	113	3584	119	3558	107
3542	25														
3564	70														
3603	17					3607	40	3608	41						
				3620	109										
3628	19														

Table 5.3: As in Table 5.1, but for the third experiment. At 04:00 the spectrum contains ice and salt peaks, as well as a single water peak at 3559 cm^{-1}. The presence of the water peak might be caused by small amounts of brine in the ice even at temperatures far below the eutectic value. This behavior was also observed at the end of the fourth experiment, when brine remained liquid even after the sample was kept below the eutectic temperature for at least 30 min (Table 5.4). The spectral decomposition has barely changed by 05:30, when the eutectic temperature has been exceeded and brine starts to become visible in the image (Fig. 5.13b). At 07:00 the salt peak disappears, and only water and ice peaks are left, consistent with Fig. 5.13c. At 11:45 the ice has melted completely, and the ice peaks have disappeared from the spectrum. Only liquid water peaks remain until the onset of a crust formation at 14:30. The onset of brine and crust formation occurs 45 min later than in the first experiment.

5.3.4 Fourth Experiment: Diurnal Cycle of Initially Frozen Brine at the Environmental Conditions of the Phoenix Strut

A fourth experiment was conducted to simulate the full Sol 19 diurnal cycle on the Phoenix strut at about 0.5 m above the ground (Figs. 5.14-5.16 and Table 5.4), where spheroids were observed. This fourth experiment started at midnight (Fig. 5.4) with frozen brine that we hypothesize to be representative of the material splashed on the Phoenix lander strut during landing. The decomposition of the Raman spectrum of frozen brine at 12:15 (Fig. 5.14), when the temperature was still below the eutectic point, indicates the presence of ice and salt peaks (Table 5.4). Similar to the peak observed in the third experiment and shown in Fig. 5.12, the perchlorate peak for the frozen brine is at 936 cm^{-1} (Fig. 5.15). The first visual evidence of melting occurs at 01:35 (Fig. 5.16b), 5 min after the eutectic temperature is exceeded. However, changes in the Raman spectrum appear only after ~04:30, when the ice peak at ~3120 cm^{-1} starts to disappear as shown in Fig. 5.14. This might be the result of a lower rate of temperature increase (Fig. 5.4) in this experiment than in the previous experiments (Fig. 5.2). The ice peaks are completely gone by 12:35, with only the liquid water peaks remaining. The spectrum does not change from 17:15 until the end of the experiment (Table 5.4), with the sample remaining liquid until midnight, despite the sample temperature being below the eutectic value during the last ~30 min of the experiment (Fig. 5.4). Brine persisted longer than in the previous experiments because the temperature at the strut at 0.5 m above the surface was below the eutectic value for only ~3 h, compared to ~7 h at the ground (Fig. 5.1). In addition, the lower maximum temperature reduced loss of water by evaporation.

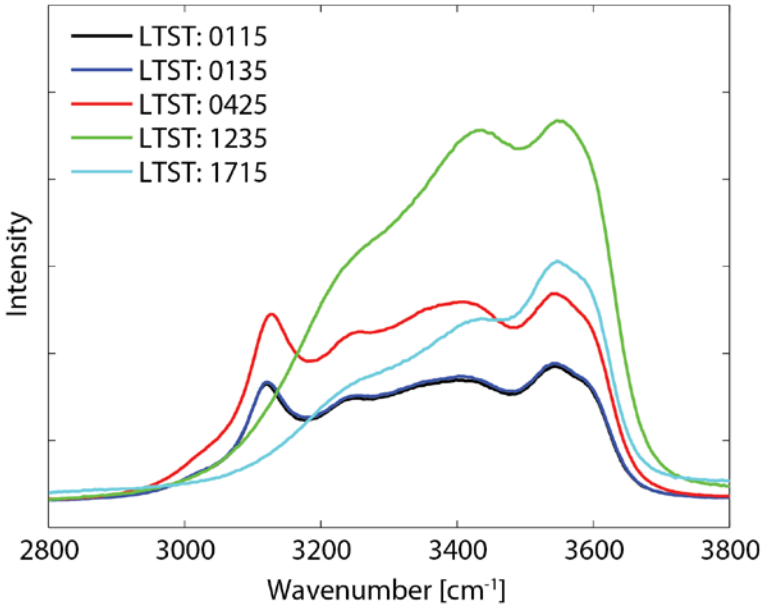

Figure 5.14: Raman spectra in the O-H stretching band throughout the diurnal cycle shown in Fig. 5.4 (fourth experiment). Gaussian components of each spectrum are shown in Table 5.4.

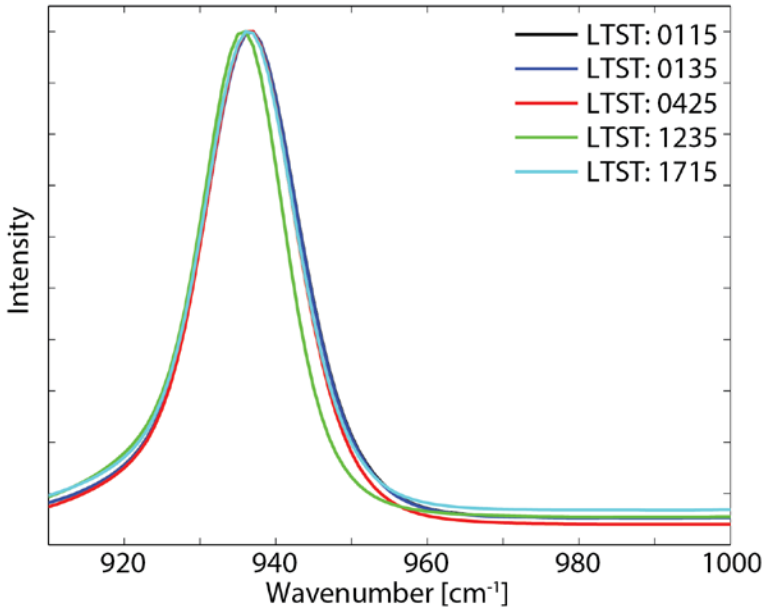

Figure 5.15: As in Fig. 5.14, but for the perchlorate vibration band. The perchlorate peak is at 936 cm^{-1} for both, the mix of water ice and salt and brine, similar to the peak shown in Fig. 5.12.

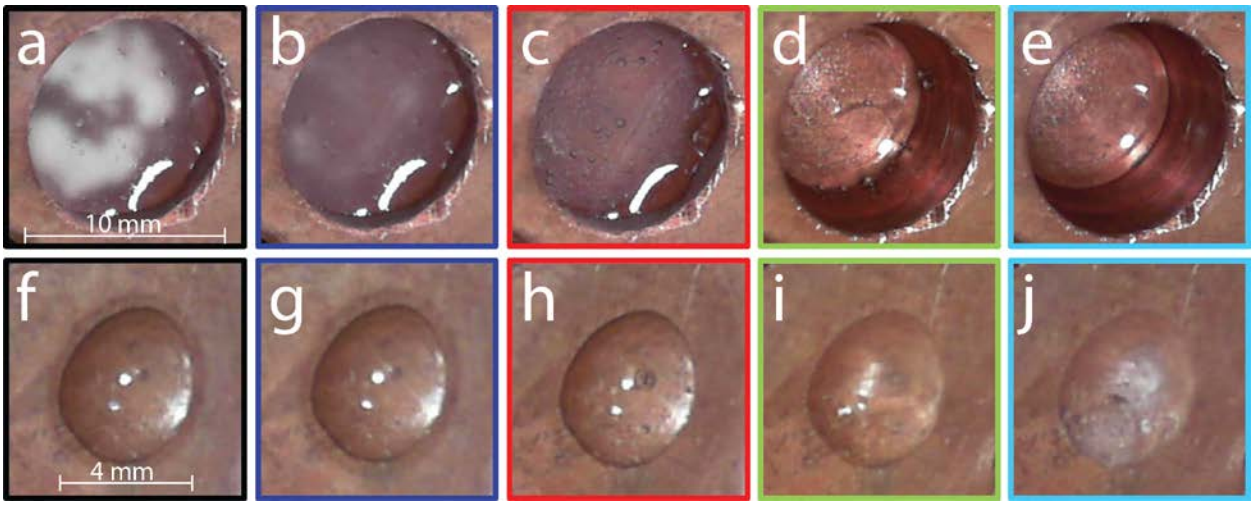

Figure 5.16: Images of the sample (a-e) and of a spheroid of the same composition (f-j), similar to those observed on the Phoenix strut, color-coded to represent the times when the Raman spectra were taken (Figs. 5.14 and 5.15). (a) Frozen mix of water ice and perchlorate salt at 01:15. Translucent areas in the sample compared to the completely whitish frozen brine in Fig. 5.10d are likely because of the larger water content of the frozen mix. (b) Onset of liquefaction at 01:35 after the temperature exceeds the eutectic value. (c) Brine and ice at 04:25, with the Raman signal indicating only the presence of ice (Table 5.4). (d-e) Only brine remains between 12:35 and 17:15. (f) Frozen spheroid at 01:15. (g) No clear sign of melting is observed at 01:35, after the eutectic temperature is exceeded. (h) Melting of the spheroid is indicated by bubble formation and movement. (i) Crust formation on the spheroid at 12:35. This indicates higher evaporation on the spheroid than on the sample holder likely because of the spheroid's larger surface-area-to-volume ratio. (j) Dry spheroid at 17:15.

5.4 Discussion

Our results show that, when water ice is in contact with $Ca(ClO_4)_2$ salt, either unmixed or as in a frozen brine, (liquid) brine forms within a few minutes in the unmixed case and within ~45 min in the case of frozen brine of the eutectic temperature being exceeded. Then, as the temperature increases during the diurnal cycle, evaporation increases the concentration of the solution, causing a salt crust to form on the top of the sample. Due to the limited penetration depth of the Raman laser, the exact time when a liquid phase ceases to exist in the sample cannot be measured unambiguously. Taking the first experiment as an example, this occurs because the position of the liquid water peak at 3555 cm^{-1} does not change abruptly between 13:45 and the end of the

experiment (Fig. 5.5; Table 5.1). Electrical conductivity or permittivity measurements may be able to determine the exact time that brine forms [*Zandonadi et al.*, 2015; *Heinz et al.*, 2016]. As evaporation thickens the salt crust, the 3555 cm^{-1} spectral peak indicating the presence of liquid water transitions smoothly into nearby peaks at 3543 and 3546 cm^{-1} indicating the presence of crystalline $Ca(ClO_4)_2$ hydrates. However, our results suggest that, while the temperature was above the eutectic value for about 17 h on Sol 19 (Fig. 5.1), brine could have formed and persisted in the Dodo-Goldilocks trench as long as enough water ice was present to compensate for evaporation. Our analysis also indicated that brine formed at about 04:37 (i.e., minutes after the ground temperature exceeded the eutectic value) and froze at about 22:20 (when the ground temperature decreased below the eutectic value).

Reference Spectra						Fourth Experiment: Sol 19 Diurnal Cycle of the Strut Temperature									
Salt		Ice		Water		LTST 0115		LTST 0135		LTST 0425		LTST 1235		LTST 1715	
Peak	FWHM	Peak	FWHM	Peak	FWHM	Peak	FWHM	Peak	FWHM	Peak	FWHM	Peak	FWHM	Peak	FWHM
		3046	99			3066	142	3069	145	3073	149				
		3115	57			3119	57	3121	58	3125	61				
		3227	206	3230	217	3213	162	3214	157	3216	157	3278	163	3289	262
		3336	56												
		3399	140	3420	218	3407	275	3406	274	3406	273	3454	181	3449	164
3446	37														
3471	20														
3487	24														
3515	29														
				3540	206							3582	121	3572	122
3542	25					3544	72	3544	72	3545	73				
3564	70														
3603	17					3600	63	3601	64	3601	67				
				3620	109										
3628	19														

Table 5.4: As in Table 5.1, but for the fourth experiment. The decomposition of the frozen mix at 01:15 contains ice and salt peaks. Despite exceeding the eutectic temperature at 01:30, spectral changes have not occurred by 04:25. This might be explained by a lower rate of temperature increase after crossing the eutectic temperature (Fig. 4) than that occurring on the ground (Fig. 2). The ice peaks start to disappear after ~04:30 and are completely gone by 12:35, with only the liquid water peaks remaining. This change is also visible in Fig. 5.16d, showing the remaining ice melting. The spectrum does not change from 17:15 until the end of the experiment, with the sample staying liquid even during the last 30 min of the experiment when the temperature decreases below the eutectic value. In this experiment, a salt crust does not form on the sample because the lower maximum temperature and near-saturated air mitigate evaporation.

Results of experiments with a soil-salt-ice mixture indicate that the presence of a soil causes a delay in brine formation. Results of these experiments will be the subject of a future article because of the added complexity to the observed Raman spectra.

Brine formation could also occur between polar and midlatitude regions, where frost and snow are seasonally deposited on saline soils [*Whiteway et al.*, 2009; *Martínez et al.*, 2012]; water ice is seasonally present in the shallow subsurface [*Cull et al.*, 2010b]; and temperatures exceed the eutectic value during a significant fraction of the sol (from minutes to hours depending on the location and time of the year) [*Möhlmann*, 2011; *Fischer et al.*, 2014; *Nuding et al.*, 2014]. Therefore, our results suggest that brine could form in the Martian polar region on seasonal timescales and persist for as long as the temperature remains above the eutectic value during diurnal cycles because the melting of water ice could compensate for evaporation.

Water ice is unlikely to be present in the shallow subsurface of midlatitudes and equatorial regions because it is not thermodynamically stable in these places [*Mitrofanov et al.*, 2002; *Schorghofer and Aharonson*, 2005]. However, frozen brine could be stable in the shallow subsurface of midlatitude regions, and brine could form temporally if the temperature exceeds the eutectic value. In addition, thin layers of frost are possible on polar-facing slopes of those regions throughout the day [*Vincendon et al.*, 2010], as well as on flat terrains at night [*Wall*, 1981; *Möhlmann*, 2008]. Under these conditions, frost in contact with $Ca(ClO_4)_2$ salt could produce brine, but only in the short time interval during which the ground temperature is above the eutectic value and the frost has not completely sublimated away.

$Ca(ClO_4)_2$ salt was detected at the Mars Science Laboratory landing site at Gale Crater [*Glavin et al.*, 2013], where evidence for nighttime formation of frost a few tenths of a micrometer thick [*Martínez et al.*, 2015; *Savijärvi et al.*, 2015] has been reported. However, frost can form at

Gale only between 04:00 and 06:00, when the ground temperature is below the eutectic point. This thin layer of frost would have likely sublimated away by ~07:00, when the ground temperature first exceeds the eutectic value on the sols when frost is predicted [*Martínez et al.*, 2015]. In addition, the solubility of $Ca(ClO_4)_2$ salts in ice of a thickness of a few tenths of a micrometer is not known. This indicates that brine is unlikely to form at the surface of Gale Crater.

5.5 Conclusion

The Phoenix lander discovered water ice [*Smith et al.*, 2009] and salts such as $Ca(ClO_4)_2$ with a eutectic temperature lower than the maximum diurnal ground temperature at its landing site [*Hecht et al.*, 2009]. In addition, Phoenix found indirect evidence for frozen brine in a shallow trench excavated by the Phoenix robotic arm on Sols 18-19 [*Rennó et al.*, 2009; *Cull et al.*, 2010a]. Here, we show that, at Phoenix landing site environmental conditions, brine forms minutes after the eutectic temperature is exceeded and stays liquid for ~18 h while the temperature is above the eutectic value if enough water ice is present to compensate for some of the water loss by evaporation. Furthermore, our experiments' results indicate that the spheroids observed on a strut of the Phoenix lander early in the mission might have remained liquid for most of the diurnal cycle (~22 h) if the melting of frozen brine splashed during the landing formed them. Thus, the Martian polar region may temporarily have one of the essential ingredients to be a habitat for microorganisms that thrive in brine [*Boetius and Joye*, 2009].

CHAPTER VI

Recalibration of the Phoenix Mission’s Relative Humidity Sensor

This chapter is in preparation for publication in a planetary science journal: Fischer, E., Martínez, G. M., Rennó, N. O., et al. (2018), Recalibration of the Phoenix Mission’s Relative Humidity Sensor.

Abstract

Here we show results of the recalibration of the Thermal and Electrical Conductivity Probe (TECP) relative humidity sensor of the Phoenix Mars lander. Due to uncertainties in its preflight calibration, which only partially overlapped the environmental conditions found at the Phoenix landing site, only the raw, unprocessed output of the TECP relative humidity sensor was available in NASA's Planetary Data System (PDS). Specifically, the TECP relative humidity sensor was neither calibrated at nighttime (< 208 K) nor at midday temperatures. The sensor's calibration was revised by *Zent et al.* [2016] to correct for inaccuracies at the lowest temperatures and the new processed RH values were recently posted in the PDS. We have been using a spare engineering unit of the TECP to recalibrate the sensor in the full range of Phoenix landing site conditions (extension to nighttime and midday conditions) in the Michigan Mars Environmental Chamber

(MMEC). Results of the recalibration show excellent agreement with those currently available in the PDS at nighttime hours, whereas during daytime conditions our water vapor pressure values are significantly higher, in accordance with modeling estimations and orbital observations. These results are important to improve our understanding of the exchange of water between the regolith and the atmosphere and thus of the current H_2O cycle. The recalibrated data will be posted in the PDS.

6.1 Introduction

The unveiling of water ice in the shallow subsurface [*Smith et al.*, 2009; *Renno et al.*, 2009], the discovery of perchlorate salts [*Hecht et al.*, 2009; *Kounaves et al.*, 2014] and the detection of near surface fog and snowfall all the way to the ground [*Whiteway et al.*, 2009; *Moores et al.*, 2010] make the Phoenix landing site an exciting place to search for liquid water on Mars. The Thermal and Electrical Conductivity Probe (TECP) onboard the Phoenix lander is an instrument that can aid this search.

The TECP is a component of the Microscopy, Electrochemistry and Conductivity Analyzer payload (MECA) [*Hecht et al.*, 2008] on the Phoenix lander. It is mounted on the Robotic Arm of the lander and was designed to monitor soil thermal properties and water content by performing six different types of measurements: temperature, thermal conductivity, volumetric heat capacity, electrical conductivity, dielectric permittivity and relative humidity [*Zent et al.*, 2009]. The TECP consists of a single electronics box, fitted with four needles, which can be inserted into the medium of interest such as the Martian soil (Fig. 6.1). The relative humidity sensor sits on the outside of the electronics box.

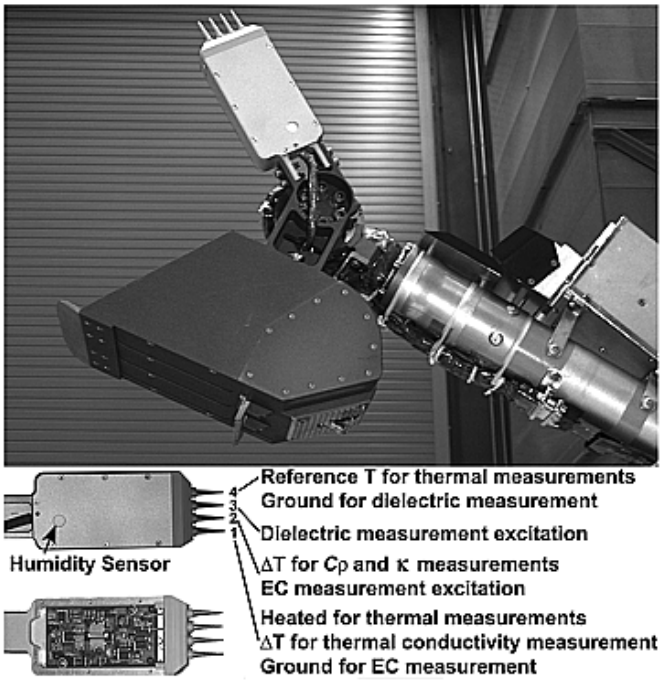

Figure 6.1: (Top) The TECP is mounted on the end of the 2.3 m long Robotic Arm. The TECP is 119 mm in length and its needles are 15 mm long. (Bottom) Close-up of the TECP, with the relative humidity sensor indicated by an arrow and with the function of each needle identified. From *Zent et al.* [2010].

The original calibration of the TECP relative humidity sensor was performed at the University of Washington Mars Atmospheric Simulation Chamber [*Zent et al.*, 2009], using a pair of frost point hygrometers (a Buck CR-1 chilled-mirror hygrometer similar to the one in the MMEC and an EdgeTech DewPrime I chilled-mirror hygrometer) as a reference. More than 50,000 measurements were obtained, covering a range of frost points from 194 to 263 K, and a range of temperatures from 208 to 303 K (with corresponding relative humidity values in range of ~0% to ~55%). From that data, a calibration function for the raw output of the sensor $DNRH = f(RH, T_b)$ was produced, where T_b is the temperature of the TECP board where the relative humidity sensor is mounted, and *RH* is the processed relative humidity derived from the frost point temperature (T_f) measured by the reference hygrometers, and the board temperature [*Zent et al.*, 2009].

Due to resource and time limitations, and the fact that the TECP was the first relative humidity sensor flown to the Martian surface, values of *DNRH* and T_b covered in the original calibration only partially overlap the environmental conditions found at the Phoenix landing site. Specifically, neither was the relative humidity sensor calibrated at $T_b < 208$ K, nor was it calibrated at high T_b and low *DNRH* values observed at midday. Therefore, high-level *RH* values processed using the calibration function around noon (when *Tb* is high and *DNRH* is low), and at dawn (when T_b is the lowest) presented large uncertainties because the calibration data set is at best sparse in these conditions [*Zent et al.*, 2016].

The calibration function was revised in 2011 and again in 2014 to correct for inaccuracies at the lowest temperatures [*Zent et al.*, 2012; *Zent et al.*, 2016]. In order to augment the original calibration at $T_b < 208$ K, flight data from sols 86, 91, 103, 104, and 122 taken between 00:00 and 04:00 were used to augment the laboratory data. On each of these sols Phoenix LIDAR measurements indicated that the Martian atmosphere was saturated throughout the lowest ~1 km after 23:00 [*Zent et al.*, 2012].

Here we show a recalibration of the TECP relative humidity sensor by significantly increasing the range of the calibration data. We recalibrate the TECP through the use of an engineering model on loan from the NASA Jet Propulsion Laboratory (JPL) exposed to the entire range of Phoenix landing site conditions in pressure, temperature and measured low-level relative humidity data in our Michigan Mars Environmental Chamber (MMEC), including those conditions not covered in the preflight calibration. Production and subsequent analysis of high-level *RH* data at the Phoenix landing site will greatly support experimental studies [*Nuding et al.*, 2014; *Fischer et al.*, 2014; *Fischer et al.*, 2016] of the formation and persistence of liquid brine at the Phoenix landing site. The following sections will give an overview of our calibration setup and

methodology (section 6.2), the results of our recalibration (section 6.3), a discussion and comparison of our results with previous calibrations and orbital measurements (section 6.4) and our conclusions of this study (section 6.5).

6.2 Setup and Methodology

6.2.1 Environmental Chamber

The recalibration of the TECP relative humidity sensor was performed in the MMEC, a cylindrical chamber with internal diameter of 64 cm and length of 160 cm (Fig. 6.2). The MMEC can simulate the entire range of environmental conditions encountered at the Phoenix landing site, including pressure between 720 and 860 Pa, temperature from 180 to 270 K and relative humidity from ~0 to >100%. This allows us to recalibrate the sensor within the entire range of its experienced in-situ conditions.

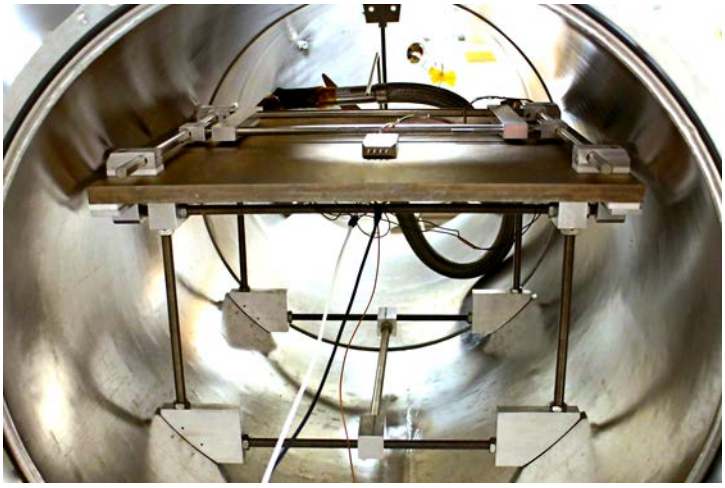

Figure 6.2: The Michigan Mars Environmental Chamber is capable of simulating Martian polar conditions, covering the environmental conditions found at the Phoenix landing site that were not tested during preflight tests. The TECP Engineering Model is sitting on top of thermal plate to allow thermal contact.

The MMEC has an automated feedback control system that uses a thermal plate with embedded cartridge heaters and a liquid Nitrogen cooling loop to control the temperature. Water vapor is added to the chamber through a temperature and pressure controlled H_2O bath. The relative humidity of the MMEC atmosphere can be adjusted to selected values by controlling the flow from the water bath into it. The local relative humidity is sampled right at the location of the TECP relative humidity sensor and measured by an independent chilled mirror hygrometer. The pressure is controlled by an automated feedback control system.

6.2.2 TECP Engineering Unit vs Flight Unit

The TECP engineering unit is an exact copy of the flight unit, but the dynamic range of the raw output of the relative humidity sensor's analog-to-digital converter differs between both units at the exact same conditions of frost and board temperature. This difference is within manufacturer specifications, but has to be accounted for in our recalibration. This difference is shown in Fig. 6.3, where the red points show the initial pre-flight calibration in terms of measured board temperature and raw humidity digital number output, and the blue points show the DNRH output of the engineering unit at the exact same board temperature and frost point temperature. To rectify this difference in the recalibration, we obtain a "translation function" g of the form:

$$DNRH_{eu} = g(DNRH_{fu}, T_b)$$

which relates the engineering unit output $DNRH_{eu}$ (Fig. 6.3 blue) to that of the flight unit $DNRH_{fu}$ (red) at the same environmental conditions. This translation function is obtained by simulating the known environmental conditions covered in the preflight flight unit calibration in our MMEC. To improve the accuracy of this translation function, we use additional values of in-situ measurement of T_b and $DNRH$ as pseudo-preflight calibration points (Fig. 6.3 green). There are two groups of

those points. One set is at the lowest observed T_b range, during the second half of the mission when near-surface fog was observed. This allows us to safely assume saturated atmospheric relative humidity conditions. The other set of pseudo-preflight calibration points is at the highest observed in-situ T_b values during midday, when we can assume that water vapor pressure values are below 5 Pa [*Savijärvi and Määttänen*, (2010); *Tamppari et al.*, 2010] and thus establish an upper bound for the frost point temperature at those conditions. This leads to the following translation function with a coefficient of determination of 86.2%:

$$DNRH_{eu} = -983.9 + 1.405 DNRH_{fu} + 3.317 \times 10^{-2} T_b$$

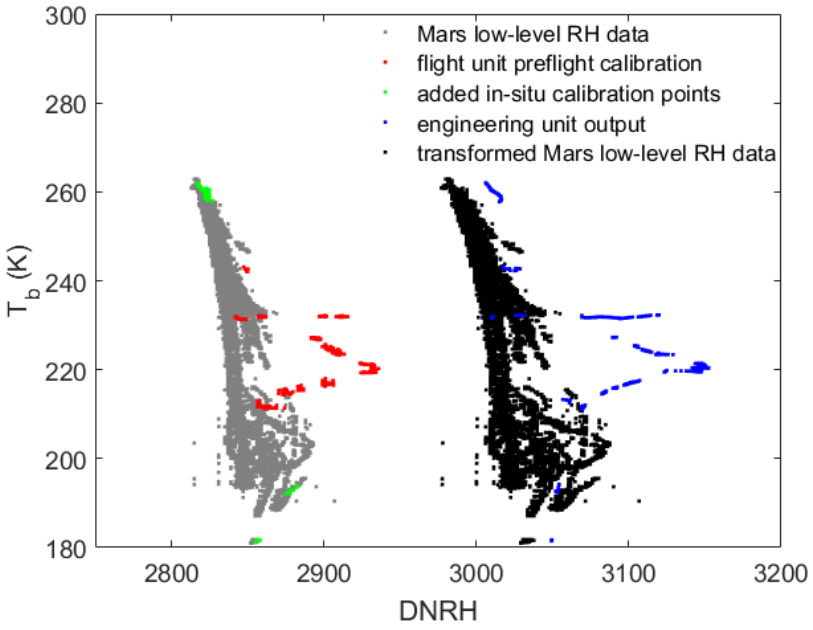

Figure 6.3: The TECP preflight calibration (red) only partially overlaps the relative humidity measurements at the Phoenix landing site (gray). We use the output of a TECP engineering unit (blue) at the same environmental conditions as the preflight calibration and at additional values known to have occurred at the landing site (green) to translate the in situ measurements into values the engineering unit would have recorded (black). We then cover this entire range of temperature and relative humidity conditions to calibrate the engineering unit and find a recalibration for the flight unit.

We then apply this translation function to the raw data obtained by the flight unit at the Phoenix landing site (Fig. 6.3, gray), resulting in the black cloud in Fig. 6.3. This is the output of the engineering unit of the relative humidity sensor, had it taken measurements concurrent with the flight sensor at the Phoenix landing site on the Martian surface.

6.2.3 A New Calibration Function

As the final step of the recalibration of the TECP relative humidity sensor, we cover the entire range of board temperature and relative humidity shown in black in Fig. 6.3. To achieve this, we place the engineering unit of the TECP inside our environmental chamber in good thermal contact with the chamber's thermal plate. We then lower the pressure inside the environmental chamber to 850 Pa of CO_2. Next, we dry out the chamber and sensor, before lowering the sensor's temperature to 181 K, the lowest temperature encountered throughout the Phoenix mission (see Fig. 6.3, black). While keeping the temperature constant, we start adding water vapor to the environment, increasing the relative humidity from ~0 to 100%. We repeat this process for the entire temperature range while measuring the raw output of the TECP humidity sensor and the frost point $T_{f,hyg}$ independently with a chilled mirror hygrometer.

We obtain a new calibration function f of the following form with a coefficient of determination of 95.1%:

$$T_{f,hyg} = f(DNRH_{eu}, T_b) = a_1 DNRH_{eu}^2 + a_2 DNRH_{eu} + a_3 \frac{DNRH_{eu}}{T_b} + a_4 T_b^2 + a_5 T_b + a_6$$

$$a_1 = -6.148 \times 10^{-4}$$

$$a_2 = 4.793$$

$$a_3 = -190.5$$

$$a_4 = 5.803 \times 10^{-2}$$

$$a_5 = -37.27$$

$$a_6 = -664.8$$

We can then apply the translation and new recalibration function to the in-situ *DNRH* values measured by the TECP to obtain the recalibrated frost point values at the Phoenix landing site:

$$T_f = f(g(DNRH_{fu}, T_b))$$

Equivalently to the frost point temperatures obtained we can calculate the water vapor pressure using the relation [*Savijärvi and Määttänen*, 2010]:

$$e = e_{s,i}(T_f) = 611.35\ exp\frac{22.542(T_f - 273.16)}{T_f + 0.32}$$

6.3 Results

Fig. 6.4 shows the water vapor pressure values obtained from our recalibration as a function of local true solar time with variations in sol number shown using color code. The daily maximum occurs at around noon and the minimum at ~02:00 LTST throughout the mission. Highest maximum diurnal values of water vapor pressure occur between sols 60 and 90. The maxima decrease in the late mission after sol 110, when the temperatures drop and the water vapor is deposited on the surface. The diurnal range in water vapor pressure is between the orders of 10^{-2} and 1 Pa and it starts to increase right after sunrise, which occurred at 02:00 LTST during the polar summer. This strongly suggests an active atmosphere-regolith interaction by water vapor deposition on or adsorption by the ground at night and sublimation at daytime.

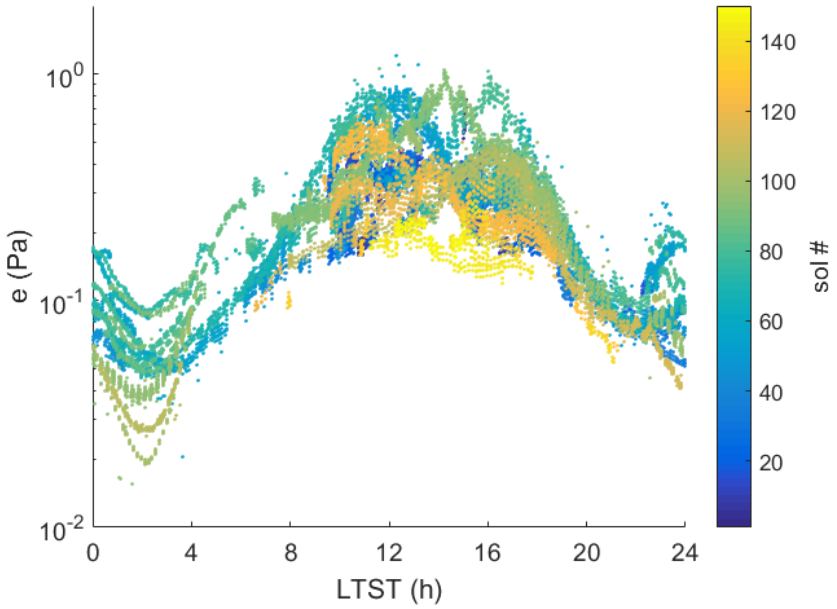

Figure 6.4: Water vapor pressure measured by the TECP for the entire range of board temperatures and color coded by sol number using the new calibration function.

Fig. 6.5 shows the diurnal cycle of relative humidity throughout the entire mission, color-coded by sol. The relative humidity was obtained using the board temperature of the relative humidity sensor as the local reference temperature. The relative humidity at different heights can be obtained by using different temperature measurements such as the MET temperatures above the lander, assuming a constant value of water vapor pressure in the vertical profile of the near-surface atmosphere. The behavior of the relative humidity shown in Fig. 6.5 is inversely related to the water vapor pressure, with relative humidity near zero through the daytime from ~08:00 to ~20:00 LTST and then quickly increasing to its maximum at 02:00 LTST. Saturation is first measured around sol 90, in excellent agreement with the LIDAR observations of fall streaks and ground fog reaching all the way to the ground from sol 109 [*Smith et al.*, 2009; *Whiteway et al.*, 2009] and nighttime frost from around sol 70 [*Zent et al.*, 2010].

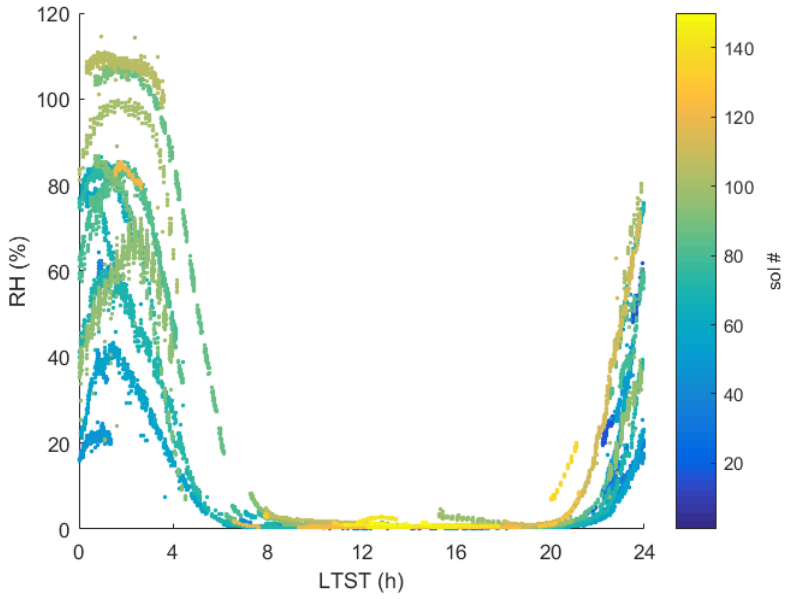

Figure 6.5: Recalibrated relative humidity data at the sensor throughout the diurnal cycle at the Phoenix landing site with color coded sol number. The occurrence of saturation (*RH* > 100%) around sol 90 coincides with the observation of ground fog at the landing site.

Fig. 6.6 shows the results of an error analysis of our relative humidity sensor recalibration in terms of water vapor pressure. The resulting error in local relative humidity at the sensor can be calculated from the frost point and board temperature. These uncertainties are based on random errors produced by the chilled mirror hygrometer during the experiments determining the new calibration function. The error in water vapor pressure shown here is on the order of 20% throughout the mission, stemming from the error in measured frost point temperature. This error does not include the small random error observed in the *DNRH* output of the sensor, which based on our experiments adds a maximum error of 5% in water vapor pressure.

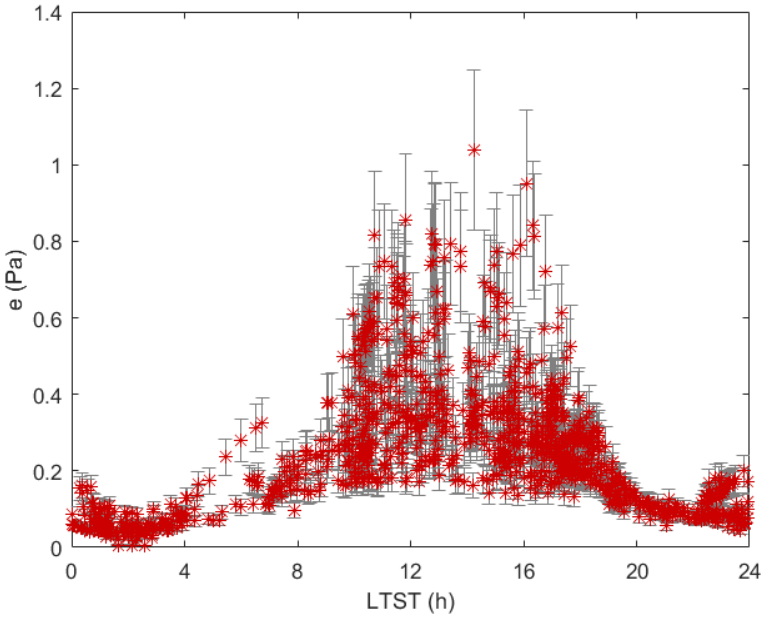

Figure 6.6: Error bars (gray) on the water vapor pressure data (red) shown in Fig. 6.4 based on our recalibration method. For illustrative purposes only 1% of all data points are shown here.

6.4 Discussion

While the seasonal exchange of adsorbed water between the regolith and the atmosphere is well understood, the diurnal exchange is rather unclear, partially due to a lack of ground-based estimations [*Martínez et al.*, 2017]. Accurate measurements of in-situ water vapor pressure or relative humidity are important to improve our understanding of the H_2O cycle. Besides Phoenix, the more recent MSL rover is the only mission carrying a relative humidity sensor to the Martian surface. The recalibration of the Phoenix relative humidity sensor will greatly improve our understanding of the diurnal H_2O exchange between the atmosphere and the ground.

Fig. 6.7 shows orbital measurements of water vapor column abundance in the vicinity of the Phoenix landing site throughout the northern summer at 14:00 LTST and derived water vapor pressure values assuming a constant water distribution [*Tamppari et al.*, 2010]. Our recalibrated values are at the lower end of the values derived from water vapor column abundances measured

from orbit. The intraseasonal variation of our obtained water vapor pressure values is consistent with that of satellite measurements of water vapor column abundance. The slightly lower maxima in our data compared to those in Fig. 6.7 are within possible errors in the assumptions for the satellite retrievals of precipitable water content (*PWC*) [*Martínez et al.*, 2016]:

$$PWC = \int_0^\infty q(z)\rho(z)dz = q_0 \int_0^\infty \rho_0 e^{-z/H} dz = \frac{H}{R_v}\frac{e_0}{T_0}$$

where q is the specific humidity, ρ is the air density, z is the altitude, H is the scale height of the atmosphere, R_v is the specific gas constant of water vapor and the index *0* indicates at the ground. Slight changes in temperature and scale height and inaccuracy in the assumption of a vertically uniform water vapor distribution can lead to different water vapor pressure values obtained from the column abundance.

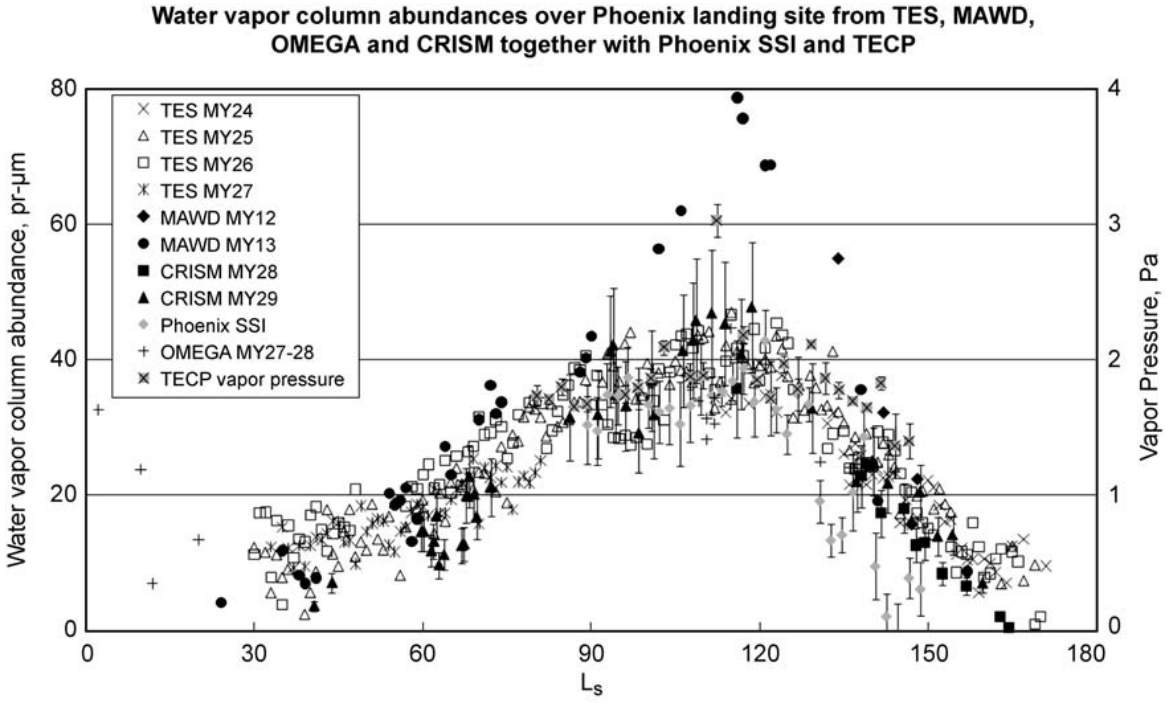

Figure 6.7: Orbital and in-situ estimates of water vapor pressure at the Phoenix landing site based on other instruments for comparison. The TECP data shown here are based on the 2009 calibration. The water vapor pressure values obtained from our recalibration are in the range of the values shown here. From *Tamppari et al.* [2010].

Fig. 6.8 shows a comparison between water vapor pressure values resulting from our recalibration in yellow, the original calibration in blue (withdrawn from the PDS due to problems with the pre-flight calibration) [*Zent et al.*, 2009], and a more recent calibration in orange (current PDS values) [*Zent et al.*, 2016]. During daytime our calibration shows water vapor pressure values similar to those of the original 2009 calibration, while during nighttime they are very similar to those of the more recent 2016 calibration. We believe this discrepancy is due to the difference in calibration range. We extended the calibration at daytime conditions, resulting in higher values compared to the previous calibration. For comparison, observed water vapor pressure values at the MSL landing site in Gale crater in the equatorial region of Mars are within the range of 0.01 to 0.08 Pa, about an order of magnitude lower than those shown here at Phoenix [*Martínez et al.*, 2017].

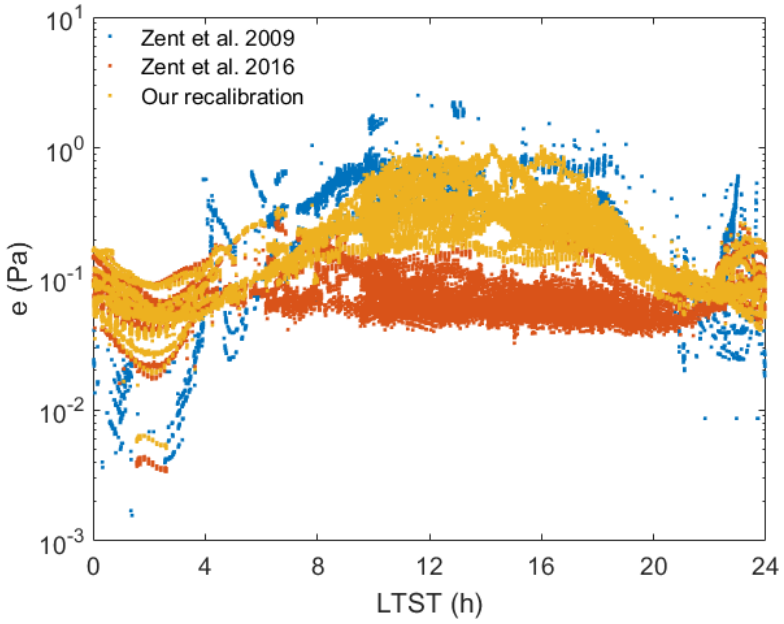

Figure 6.8: Comparison of our new calibration with previous calibration results. While our data is similar to the two previous calibrations at nighttime, it is an order of magnitude larger during daytime, where it is more similar to the original calibration.

6.5 Conclusion

We have completed the recalibration the Phoenix relative humidity sensor by covering the entire range of temperature and relative humidity conditions observed at the landing site. Specifically, we have extended the calibration to daytime conditions with very low relative humidity and high temperature values and to nighttime conditions with the lowest temperature and highest relative humidity conditions. The resulting humidity values measured at the Phoenix landing site correlate well with local observations of ground fog and frost, and with data from orbital instruments within their error range. Compared to the previous calibration, our data shows a larger diurnal range of water vapor pressure, at around two orders of magnitude. This implies a stronger exchange of water between the regolith and the atmosphere and stresses the role of the regolith in the global water cycle on Mars. We plan to make our recalibrated high-level relative humidity values available in the NASA PDS to make them accessible to the science community, enhancing the scientific return of the Phoenix mission years after the last signal from the lander. This would also allow them to be cross-checked by atmospheric modeling. Our results can lead to a better understanding of the hydrological cycle at the Phoenix landing site and the Martian northern polar region in general. They will also give us a better understanding of when conditions necessary for brine formation are met.

CHAPTER VII

Summary and Conclusions

The necessary conditions to form liquid brine on Mars, that is, salts with a low eutectic temperature such as perchlorates in the Martian soil, enough water vapor for the relative humidity to exceed a threshold for brine formation, and water ice in contact with the aforementioned salts, have been shown to be met in various locations across Mars, from polar to equatorial latitudes. Brine can form by two different processes on Mars: deliquescence, the formation of a solution by the absorption of atmospheric water vapor by hygroscopic salts, and the melting of water ice in direct contact with salts with low eutectic temperatures.

We have designed and built an environmental chamber that can simulate the entire range of Martian atmospheric conditions in terms of pressure, temperature and relative humidity, in order to study these two mechanisms of brine formation on Mars and to test, improve and calibrate sensors that can help us understand the environmental conditions at the Martian surface.

We have shown that Raman spectroscopy is an excellent technique for detecting the phase change associated with brine formation, as well as the hydration state of salts and saturation of a brine. We showed that the O-H vibrational band of the Raman spectrum of perchlorate salts is the preferential region to detect brine formation due to its clear changes in peak positions and widths with the change from crystalline salt to a solution, specifically the change in the O-H spectrum

from eight narrow peaks between ~3400 and 3600 cm^{-1} with nearly all of them having the widths of less than 50 cm^{-1} typical of the hydrated perchlorate salts, to the four wide peaks between ~3200 and 3600 cm^{-1} with the widths greater than 100 cm^{-1} typical of liquid water, is an unambiguous indicator of a solution. We further showed that the perchlorate band of the Raman spectrum (the ~930 to 1000 cm^{-1} region of the spectrum) can help in distinguishing hydration states of crystalline perchlorate salts by looking at the shift of the peak position, but our experiments show that this shift by itself is not a sufficient indicator of a brine. This experience in the observation of changes in the O-H and perchlorate vibrational band could aid the search for liquid brines on Mars with future missions flying Raman spectrometers.

By experimentally investigating the deliquescence of calcium perchlorate and the melting of ice using this salt, we learned that the two processes exhibit very different kinetics at Martian conditions, specifically those of the Phoenix landing site in the northern polar region. We found that while brine formation by melting is a very fast process once the environmental conditions are favorable, brine formation by deliquescence of a bulk salt pocket that might have formed due to freeze-thaw-cycles is much slower and was not observed within the time of favorable conditions within the diurnal cycle of temperature and relative humidity at the Phoenix landing site.

After suggesting that brine formation through ice is much faster than through deliquescence, we simulated entire diurnal cycles of the environmental conditions at the Phoenix landing site in our environmental chamber. The results obtained indicate that perchlorate salts in contact with ice can quickly form liquid brines within minutes after the ground temperature is above the salts' eutectic temperatures and can persist for up to 18 hours under the most favorable conditions, whereas when atmospheric water vapor is the only source of water bulk deliquescence is too slow to occur. Therefore we suggest that liquid brines are likely to form in the shallow

subsurface on Mars where water ice exists and the temperature of the shallow subsurface to can exceed the eutectic temperature of many salts found on Mars, while the top regolith inhibits sublimation and evaporation. This helps resolve the apparent inconsistency between the slow kinetics of deliquescence in the low pressure and water vapor content environment on Mars and observational evidence for temporarily liquid brine. Such observational evidence has been observed on the struts of the Phoenix lander where we suggest that saline soil mixed with subsurface water ice splashed onto during landing or in the trenches dug by its robotic arm where soft, likely saline, ice was uncovered. Furthermore, this result suggests that brine might form temporarily from frost formed on the saline soil.

To further aid in the understanding of the environmental conditions on Mars and specifically our understanding of the hydrological cycle at the Phoenix landing site, we have completed the recalibration of the relative humidity sensor of the TECP instrument onboard the Phoenix lander in our environmental chamber. The sensor had initially been calibrated in 2009 but after inconsistencies were uncovered due to limited pre-flight calibration capabilities and the fact that this was the first relative humidity sensor on Mars, the processed relative humidity data was pulled from the NASA PDS. Only recently, in 2016, a new calibration function was published and the data reposted in the PDS. In contrast to any previous calibration, we have performed our recalibration in the entire range of temperature and humidity encountered at the landing site. Compared to the previous calibration, our data shows a larger diurnal range of water vapor pressure because we expanded the calibration range. The humidity values resulting from our recalibration correlate well with local observations of ground fog and frost, and with data from orbital measurements. We will publish our recalibrated humidity data and upload it to the PDS.

Looking at Mars globally, the results of our studies suggest that temporary brine formation is the most likely to occur where subsurface ice and ample amounts of salts with low eutectic temperatures are present. This is the case in the polar regions such as at the Phoenix landing site. RSL at equator-facing dunes in low and mid-latitudes are unlikely to be formed by brine formation based on our findings, due to the lack of subsurface ice in the dunes and the amount of water vapor needed to sustain such large wet features by deliquescence. Even though there are favored dry mechanisms for Slope Streaks to form at low latitudes, the possible presence of subsurface ice at their locations does not exclude brine to be a wet mechanism of their formation based on our findings. Another areas under current investigation, the MSL site in Gale crater is unlikely to support the formation of liquid brine because of its lack of subsurface water ice that would have been detected by its Dynamic Albedo Neutron (DAN) instrument, as well as due to the site's low humidity.

Our results have important implications for the understanding of the habitability of Mars because liquid water is essential for life as we know it, and terrestrial bacterial life can thrive in brines. Thus, parts of Mars may temporarily have one of the essential ingredients to be a habitat for microorganisms that thrive in brine.

CHAPTER VIII

Future Work

8.1 Brine Kinetics

We investigated two mechanisms of brine formation in the previous chapters: formation by deliquescence of salts [*Renno et al.*, 2009; *Zorzano et al.*, 2009; *Davila et al.*, 2010; *Gough et al.*, 2011; *Nuding et al.*, 2015; *Nikolakakos and Whiteway*, 2015] and by melting of water ice through contact with salts [*Fairén et al.*, 2009; *Cull et al.*, 2010; *Chevrier et al.*, 2012; *Fischer et al.*, 2014; *Fischer et al.*, 2016]. We plan to further investigate the reaction kinetics of these two brine formation mechanisms at various Martian conditions within the range of environmental conditions that are favorable to deliquescence and melting (Figure 8.1), ranging from Martian equatorial to polar latitudes. Once we understand the reaction kinetics of brine formation at various temperatures and relative humidity conditions, we will investigate the persistence of these brines, even into unfavorable environmental conditions. This will help us understand any possible hysteresis effects associated with deliquescence and efflorescence, as well as with melting and freezing of brine. Last, we plan to expand these environmental conditions to those of other planetary bodies in our solar system, such as the so-called Icy Worlds, Jovian and Cronian moons

such as Titan, Europa or Enceladus, that may support life. To achieve this, our environmental chamber will have to be improved to be capable of simulating the more extreme environmental conditions at the Icy Worlds.

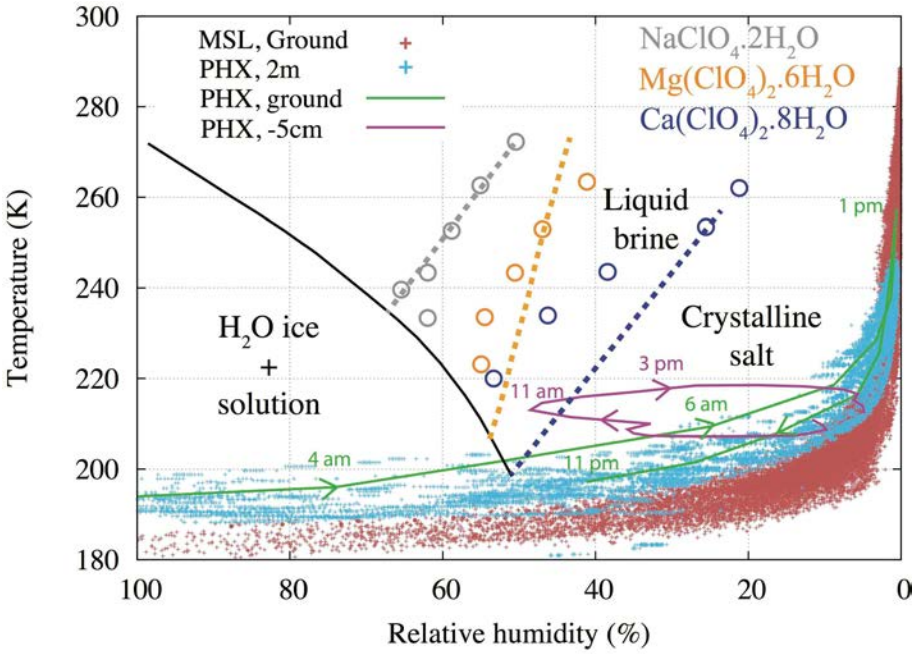

Figure 8.1: Stability diagram as in Fig. 1.2, with superimposed values of: simultaneous RH and ground temperature for the first 1772 sols of the MSL mission (maroon), simultaneous RH and air temperature at 2 m measured by the PHX/MET instrument for the entire duration (151 sols) of the PHX mission (sky-blue), simulated ground (green) and subsurface (purple) temperature on sol 19 of the PHX mission. Results from previous laboratory experiments of deliquescence of Ca, Mg and Na perchlorates are shown in colored circles. RH values shown here have been calculated with respect to liquid, in accordance with the dashed lines representing phase change.

We plan to use our environmental chamber to simulate a variety of surface conditions representative of various locations on Mars and beyond. We plan to conduct experiments with a variety of salts existent in the Martian soil, such as $Ca(ClO_4)_2$, $Mg(ClO_4)_2$ and $NaClO_4$ to establish a reference for the dependence of brine formation on temperature and relative humidity at a wide range of Martian conditions and beyond. Figure 8.1 shows the stability diagram of these salts, overlaid with measured and modeled conditions at the MSL and Phoenix landing sites. It shows

that conditions at those sites could be temporarily favorable for brine formation. We also plan to conduct experiments to investigate the dependence of brine formation and persistence on the ice-salt ratio, ice and salt distribution in the sample, and percentage of salt in the Martian soil simulant.

8.2 Mixed Salts

In the previous chapters we looked into brine formation from single salts. We further plan to investigate how brine formation, both from deliquescence and melting of water ice, changes for complex brines, more realistic mixtures of salts that can theoretically form brines at lower temperatures than their individual constituents [*Brass*, 1980]. A sketch of the ternary phase diagrams showing this phenomenon can be seen in Figure 8.2. First, we will experimentally determine the eutectic temperatures of mixtures of salts that exist in the Martian soil and of those assumed to be present on the Icy Worlds. Next we will simulate Martian diurnal cycles and investigate the formation and stability of n-eutectic brines of multiple salts in ice inclusion [*Hall et al.*, 1988]. Finally, we plan to expand the experimental conditions to those of the icy worlds and repeat the experiments.

8.3 Planetary Protection

The goal of planetary protection is to prevent biological contamination of other planetary bodies by terrestrial organisms (forward contamination) and of the Earth by samples returned from them (backward contamination) [*Conley and Rummel*, 2010]. One of the top goals of NASA's Planetary Protection Program is to improve our understanding of the potential for both forward (transfer of viable organisms from Earth) and backward contamination (transfer of extraterrestrial organisms to Earth) in order to refine protocols for spacecraft preparation and operations. We plan

to study the formation of frost and brine droplets on a selection of spacecraft materials to shed light on their implications to forward contamination. We will focus on studying the planetary environmental conditions and transport processes that could permit the mobilization of spacecraft-associated contaminants to locations in which Earth organisms might thrive. This research could lead to the development of additional procedures for spacecraft sterilization that are compatible with spacecraft materials and assemblies, specifically the identification and removal of biogenic ice nuclei from spacecraft surfaces.

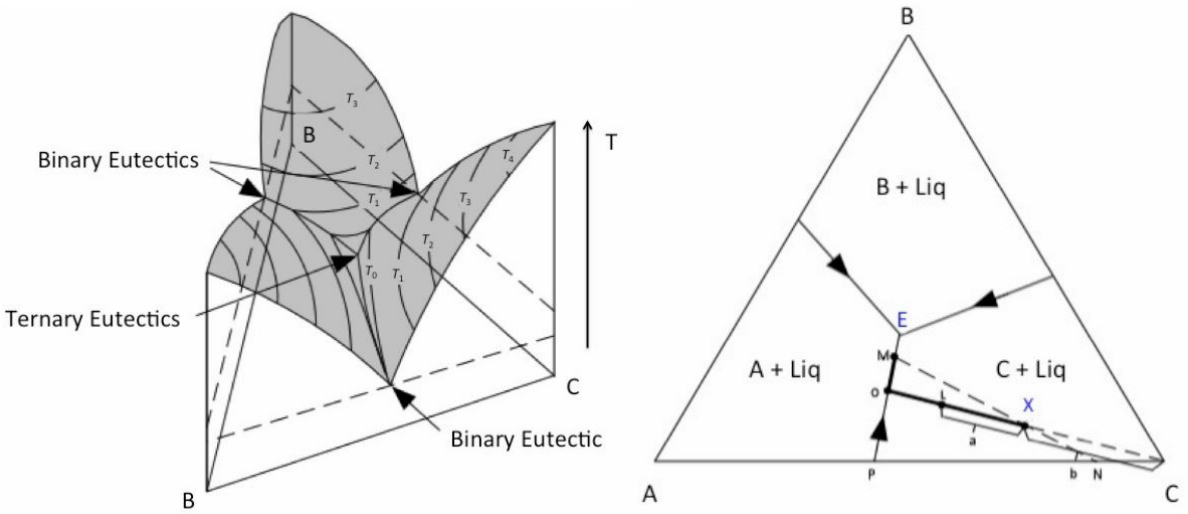

Figure 8.2: Three- and two-dimensional sketches of a ternary phase diagram. (Left) Liquidus surfaces colored in gray, with composition plotted along the sides of the triangular base, and temperature plotted vertically. Isotherms are shown as contours on the gray liquidus surfaces. The binary eutectics are represented by the boundary curves between the surfaces that the two phases on each side of the curve crystalizes. (Right) Crystallization path of mixture of composition X, showing that the solids resulting from the crystallization of mixture X (bold path) contains components A, B and C.

To achieve this goal we plan to study the potential for frost to form on a variety of typical planetary lander or rover outer surfaces at Martian conditions. Additionally we will investigate how organic ice nuclei and inorganic Martian dust analogue can affect frost formation and the possibility of this frost to form liquid brine on these surfaces. The next steps are to understand the

habitability of these brine microenvironments and to estimate the potential of aeolian processes to transport material from a spacecraft landed on Mars to other places on the planet.

8.4 Mission Support

Chapter VI describes our recalibration effort of the TECP relative humidity sensor onboard the Phoenix lander. Based on the experience gained in this project, we have started to collaborate with the Finnish Meteorological Institute on calibration updates of the REMS relative humidity sensor onboard Curiosity and on the preflight calibration of the MEDA relative humidity sensor which will fly onboard Mars 2020 (Fig. 8.3). Our environmental chamber is an ideal testbed for these calibrations, since it is the only chamber (known to us) that is able to accurately simulate simultaneous Martian temperature and relative humidity values at Martian pressure.

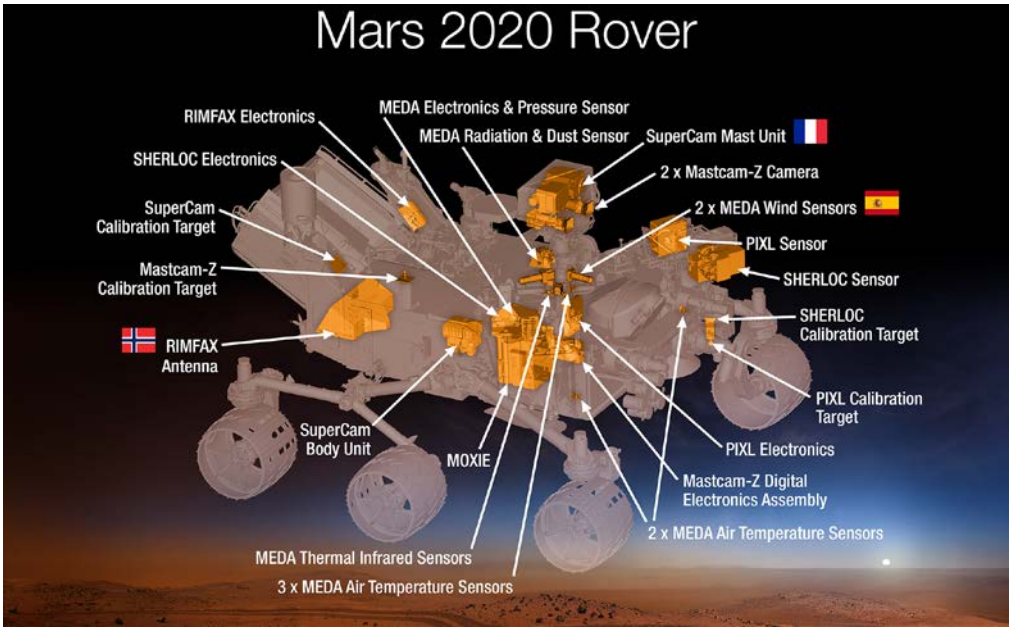

Figure 8.3: Overview of the Mars 2020 rover instruments including MEDA. Image credit: NASA.

APPENDICES

A.1 Supplementary Material for Chapter IV

Figure	Peaks	Peak Center (cm^{-1})	Peak Height	Peak FWHM	$\overline{R}^2$
1a	8	3445.67	0.09	37.32	0.999
		3471.12	0.08	20.00	
		3487.49	0.10	23.74	
		3515.20	0.07	29.08	
		3541.86	0.04	24.94	
		3564.14	0.02	70.13	
		3603.29	0.03	16.62	
		3628.01	0.04	19.00	
1b	5	3046.41	0.12	99.07	0.997
		3114.74	0.51	56.51	
		3227.14	0.30	206.09	
		3335.80	0.05	56.19	
		3399.35	0.19	140.46	
1c	4	3230.00	0.50	216.80	0.997
		3420.00	0.59	218.13	
		3540.00	0.21	205.79	
		3620.00	0.09	109.38	
2b	8	3446.92	0.10	40.44	0.999
		3470.38	0.05	18.89	
		3486.42	0.10	26.79	
		3515.84	0.08	28.14	
		3541.44	0.06	24.52	
		3562.39	0.03	71.15	
		3603.51	0.03	17.78	
		3628.01	0.04	18.04	
3b	12	3067.00	0.02	143.83	0.999
		3120.26	0.04	59.22	
		3235.63	0.03	161.31	
		3410.35	0.04	167.22	
		3439.75	0.09	31.23	
		3467.61	0.13	20.22	
		3486.80	0.11	20.05	
		3509.69	0.07	22.22	
		3535.76	0.07	30.43	
		3576.71	0.03	50.00	
		3602.46	0.04	14.71	
		3630.48	0.05	29.89	
3c	7	3059.77	0.13	138.23	0.999
		3126.56	0.32	62.21	
		3249.65	0.37	241.34	
		3356.42	0.13	81.32	
		3424.28	0.19	92.20	
		3544.89	0.26	160.28	
		3605.32	0.02	34.22	
S2	4	3230.34	0.11	177.75	1.000
		3437.28	0.25	251.41	
		3558.78	0.09	83.42	
		3610.27	0.10	73.01	

Table A.1: Characteristics of the Gaussian decompositions of the spectra shown in the figures of this letter. This data is necessary to reproduce decomposition figures from the main body and figures in the auxiliary material.

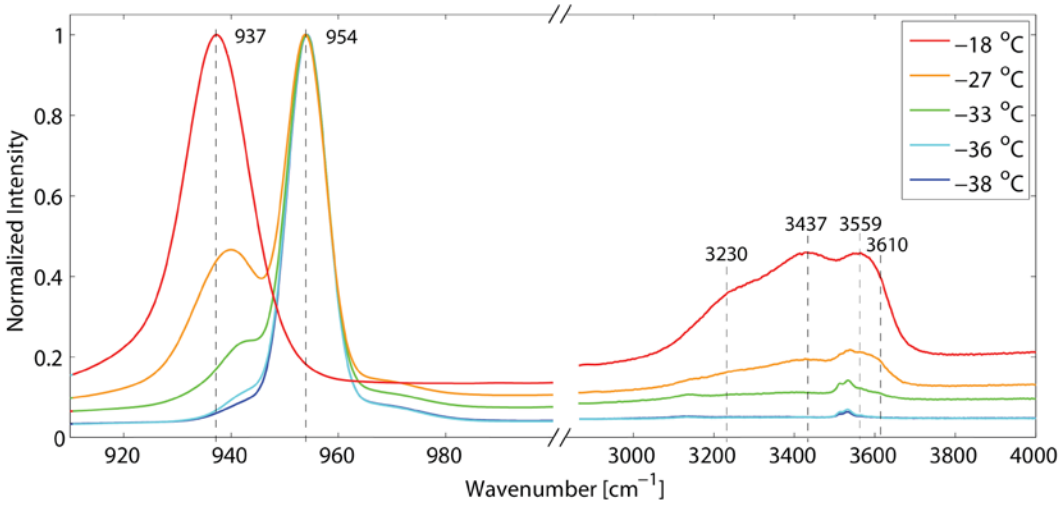

Figure A.1: Spectra of sodium perchlorate in contact with ice. Experiments similar to those for $Ca(ClO_4)_2$ were performed for $NaClO_4$ in contact with ice while the temperature of the sample was raised above its eutectic temperature $T_e \approx$ -37 ºC at the typical rate occurring diurnally in the shallow Martian subsurface. When the crystalline salt (here mostly anhydrous $NaClO_4$ but with small peaks in the O-H region indicating partial hydration) hydrates or forms a liquid solution, the 954 cm^{-1} peak in the Raman spectrum shifts toward 937 cm^{-1}. The appearance of the typical O-H vibrational band for liquid water indicates the occurrence of a liquid solution within about 1 hour of the start of the experiment, when the salt is in contact with ice at environmental conditions of Mars' polar region.

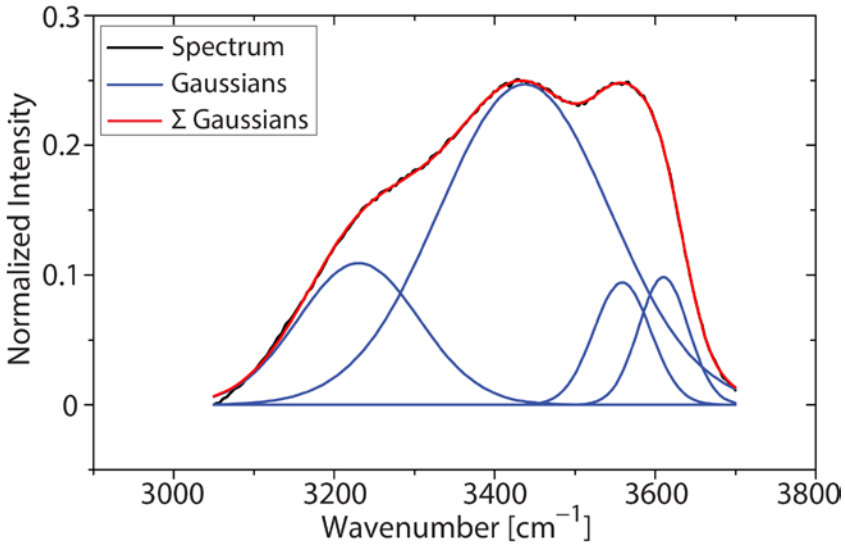

Figure A.2: Decomposed OH vibrational spectrum of $NaClO_4$ in contact with ice at -18 ºC. The O-H vibrational spectrum at -18 ºC shown in Figure A.1 contain four Gaussians components at 3230, 3437, 3559, and 3610 cm^{-1} with FWHM > 50 cm^{-1} indicating the presence of liquid water. $\bar{R}^2 \approx 1.000$.

A.2 Supplementary Material for Chapter V

A.2.1 The Michigan Mars Environmental Chamber

All experiments reported in this article were conducted in the Michigan Mars Environmental Chamber (MMEC), a cylindrical chamber with internal diameter of 64 cm and length of 160 cm (Figure 3.1). The MMEC is capable of simulating temperatures ranging from 145 to 500 K, CO_2 pressures ranging from 10 to 10^5 Pa, and the entire range of relative humidity at the Phoenix landing site.

The MMEC temperature is regulated by an automated feedback control system using a thermal plate with embedded cartridge heaters and a liquid Nitrogen cooling loop. The temperature can be measured at eight locations inside the chamber, including the sample holder. The pressure is controlled by an automated feedback control system. Water vapor is added to the chamber through a temperature and pressure controlled H_2O bath. The relative humidity of the MMEC atmosphere can be adjusted to selected values by controlling the flow from the water bath into it. The relative humidity of the chamber air with respect to the sample holder is determined by measuring the frost point with a chilled mirror hygrometer. A camera is used to image the samples while a Raman scattering spectrometer is used to detect phase changes in the sample. The Raman spectrometer laser is pointing at a fixed location in the sample holder.

A.2.2 Data Analysis

Gaussian decomposition is used to analyze the Raman spectra quantitatively. After subtraction of the baseline signal, the measured spectrum is decomposed into Gaussians using the Origin® software package. The condition that every relative maximum and minimum of the relevant portions of the spectrum has to be resolved is imposed, this results in fits with $\bar{R}^2 \geq 0.98$.

Then, the characteristics of the spectral peak of each Gaussian are compared with those of the references, as shown in Tables 5.1-5.4.

A.2.3 Environmental Conditions at the Phoenix Landing Site on Sol 19

Here we describe the procedure used to calculate the temperature cycles shown in Figures 5.1-5.4, which correspond to the temperature cycle at the Dodo-Goldilocks trench excavated by the Phoenix RA on sols 18-19 (Figure 1.3, right), the temperature cycle at the portion of the strut where the spheroids were observed (Figure 1.3, left), and the frost point temperature cycle of the surrounding air in the trench.

In the first three experiments, we obtained the trench temperature and the frost point temperature of the surrounding atmosphere using a 1D hydrostatic column model developed to simulate environmental conditions at locations such as the Phoenix landing site (68°N) [*Savijärvi and Määttänen*, 2010]. This model includes 28 atmospheric layers up to 28 km, with the separation between layers increasing with height to resolve turbulent motions more accurately closer to the ground. Due to high vertical resolution near the ground, a short time step of 10 s is used to minimize possible nonlinear numerical instabilities. To avoid climate drift, the model is run for four sols with the same external forcing to ensure that the models repeats its diurnal cycle, which typically occurs after the third sol.

We tuned the model to match the Phoenix in situ measurements of near-surface air temperature, surface pressure, dust opacity, precipitable water content (PWC) and planetary boundary layer (PBL) height as closely as possible. In addition, we tuned the model to match satellite estimations of the vertical extent of water vapor (hygropause) at the Phoenix landing site on around sol 19. Simulated ground temperature and frost point temperature shown in Figures S3

are obtained when the best match between measured and simulated quantities is achieved. Specifically, the air temperature and surface pressure were measured by the MET station [*Davy et al.*, 2010; *Taylor et al.*, 2010], dust opacity and PWC were measured by the Surface Stereo Imager [*Tamppari et al.*, 2010], the PBL height was estimated by the light detection and ranging instrument (LIDAR) [*Whiteway et al.*, 2009], and the vertical extent of water vapor was estimated from measurements by the Thermal Emission Spectrometer (TES) instrument [*Pankine and Tamppari*, 2015].

The model surface pressure and dust opacity are set to observed values of ~840 Pa and 0.5, while the thermal inertia and surface albedo are set to values of 150 SI and 0.18, similar to the values mapped by the Mars Global Surveyor [*Savijärvi and Määttänen*, 2010] at the Phoenix landing site. This combination of values provides the best match between simulated (black curve) and measured (gray asterisks) temperatures at 2 m shown in Figure A.3, and therefore the most realistic values of the simulated ground temperature (red curve).

The surface wetness (β) and the initial vertical profile of specific humidity (q) are set to values such that the simulated PWC integrated over the entire column (28 km) matches the value of about 30 pr-μm observed by the Phoenix Surface Stereo Imager [*Tamppari et al.*, 2010]. Variations of β and q values have a negligible impact on the simulated temperature at the ground and at 2 m above the surface, but strongly affect PWC values. Here we set β to a value of ~0.03% and q(z) to a value such that it leads to a constant initial vertical profile of relative humidity of 80% across vertical domain of the model (28 km). This combination of values provides the best match between simulated and measured PWC and vertical extent of water vapor, and thus the most realistic values of the simulated frost point temperatures at the surface (Figure A.3, blue curve). Further details to ensure the reliability of the numerical simulation are given next. Ground-based

measurements by the LIDAR onboard the Phoenix lander indicated that the PBL extended to heights of around 4 km. The results of simulations with our numerical model are consistent with LIDAR observations; in particular, the model predicts PBL heights of about ~4 km. The vertical extent of water vapor at the Phoenix landing site on sol 19 (Ls ~ 85°) was around 10-12 km, as estimated from satellite TES measurements [*Pankine and Tamppari*, 2015]. Furthermore, the results of simulations with our numerical model are consistent with TES estimations; in particular the model predicts that 94% of the simulated PWC (~28 pr-μm) is located within the first 10 -12 km, with only about 57 % of the simulated PWC (17 pr-μm) distributed within the PBL. Obviously, the density of water vapor decreases exponentially with height and is very low above 10-12 km, which explains why the contribution from this vapor to the PWC is negligible compared to that below the first 10-12 km.

In the fourth experiment, the temperature of the portion of the strut where the spheroids darken and appear to liquefy (~0.5 m above the surface) is calculated as the average between the numerically simulated ground temperature shown in Figure A.3 and the temperature at the top of the strut measured by an engineering sensor located at the bottom of the lander deck (~1 m above the surface). Since the engineering sensor started to make measurements only on sol 60 [*Renno et al.*, 2009], the temperature at the top of the strut on sol 19 was estimated as follows. First the differences between the temperatures measured by MET at 1.25 m and the temperatures measured by the engineering sensor on sol 60 are calculated. Then, these differences are assumed to be of the same order as on sol 19, and are used to estimate the temperature at the top of the strut from the MET measurements at 1.25 m above the surface on sol 19. This approach is justified by the fact that the MET and the engineering sensors were both located at similar heights, and the

assumption that thermal contamination from the rover deck affects both sensors in a similar fashion.

The Thermal and Electrical Conductivity Probe (TECP) aboard the Phoenix lander measured ground temperature and relative humidity [*Zent et al.*, 2010]. However, none of these measurements have been used in this study. On one hand, ground temperatures were first measured by the TECP on sol 46, when temperatures were noticeably higher than on sol 19. In addition, the thermal coupling between the TECP needles and the soil was impaired by the low thermal conductivity of the regolith, which resulted in very steep thermal gradients near the surface [*Zent et al.*, 2010]. On another hand, relative humidity measurements by the TECP were removed from the NASA PDS in December 2010 because of uncertainties in pre-flight instrument calibration. Values of temperature and relative humidity covered in the pre-flight calibration [*Zent et al.*, 2009] overlapped only partially with the environmental conditions later found at the Phoenix landing site [*Renno et al.*, 2009; *Davy et al.*, 2010; *Tamppari et al.*, 2010]. For these reasons, we have calculated ground and frost point temperatures using a numerical model developed to simulate Mars' polar conditions [*Savijärvi and Määttänen*, 2010].

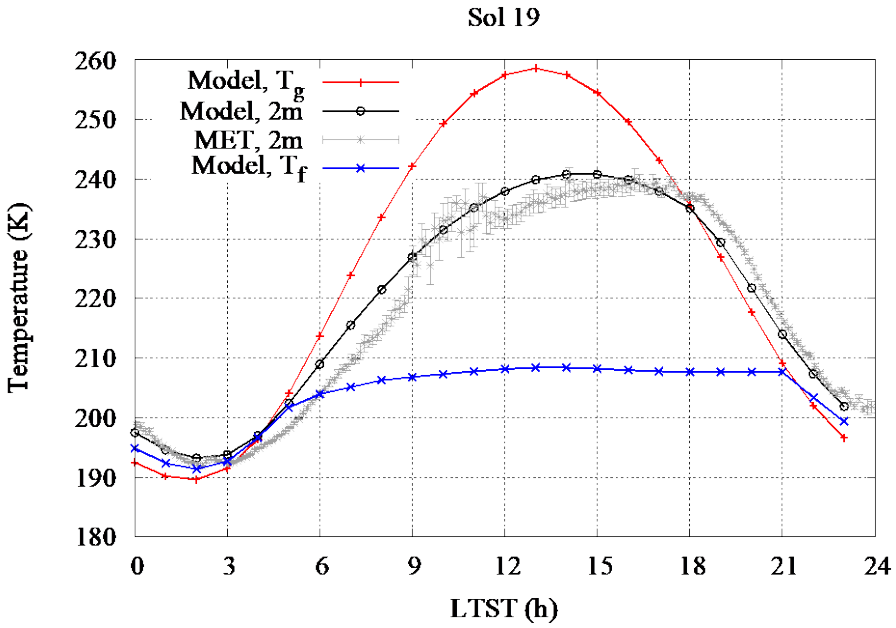

Figure A.3: Simulated ground temperature (red curve), simulated air temperature at 2 m above the ground (black curve), air temperature measured at 2 m by MET (gray asterisks) and simulated frost point temperature above the surface (blue curve) on sol 19.

B. Design Drawings of the Michigan Mars Environmental Chamber

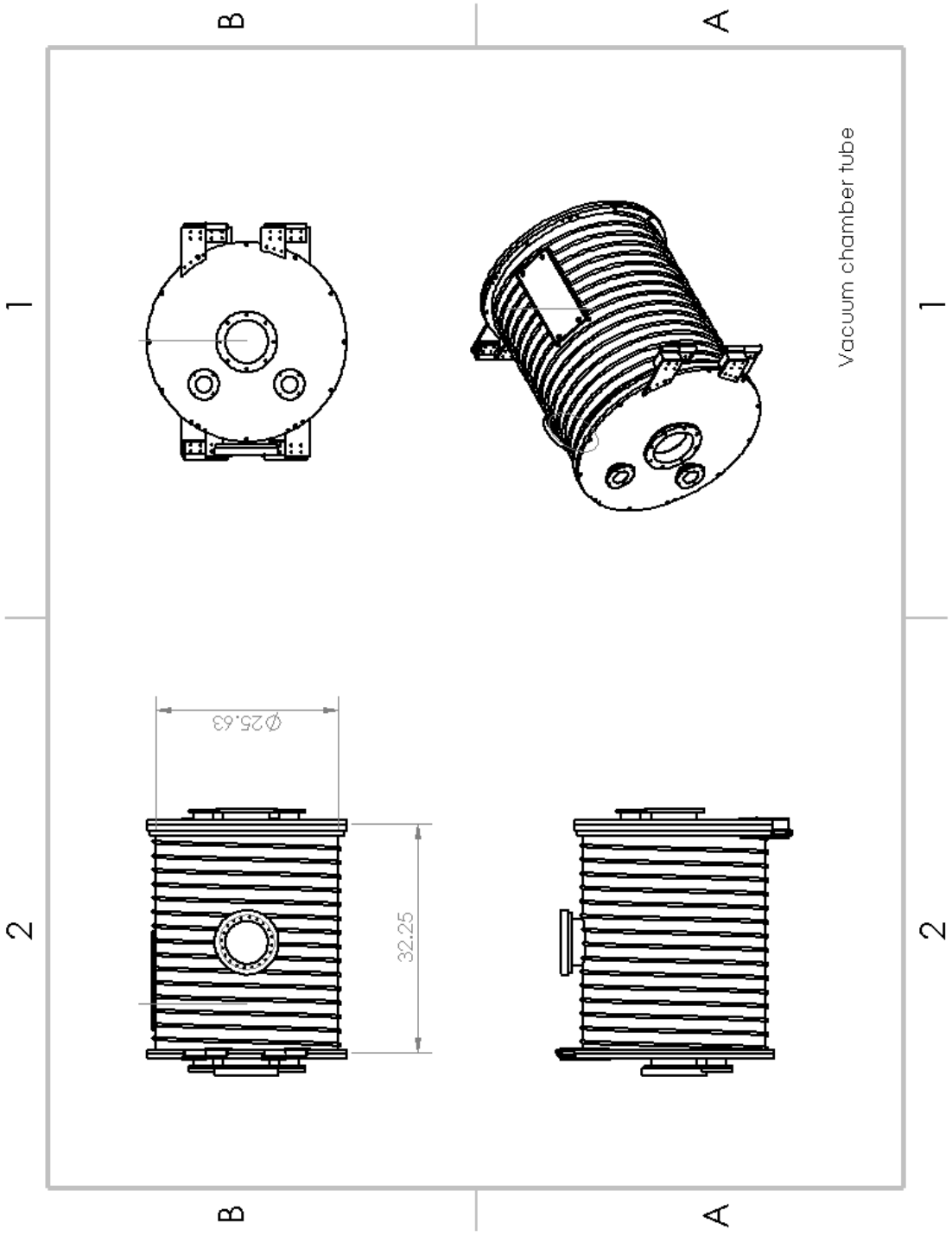

Figure B.1: Simplified CAD drawing of the external Michigan Mars Environmental Chamber structure. The updated version is doubled in length, consisting of two of the tubes shown here. Dimensions are in inches.

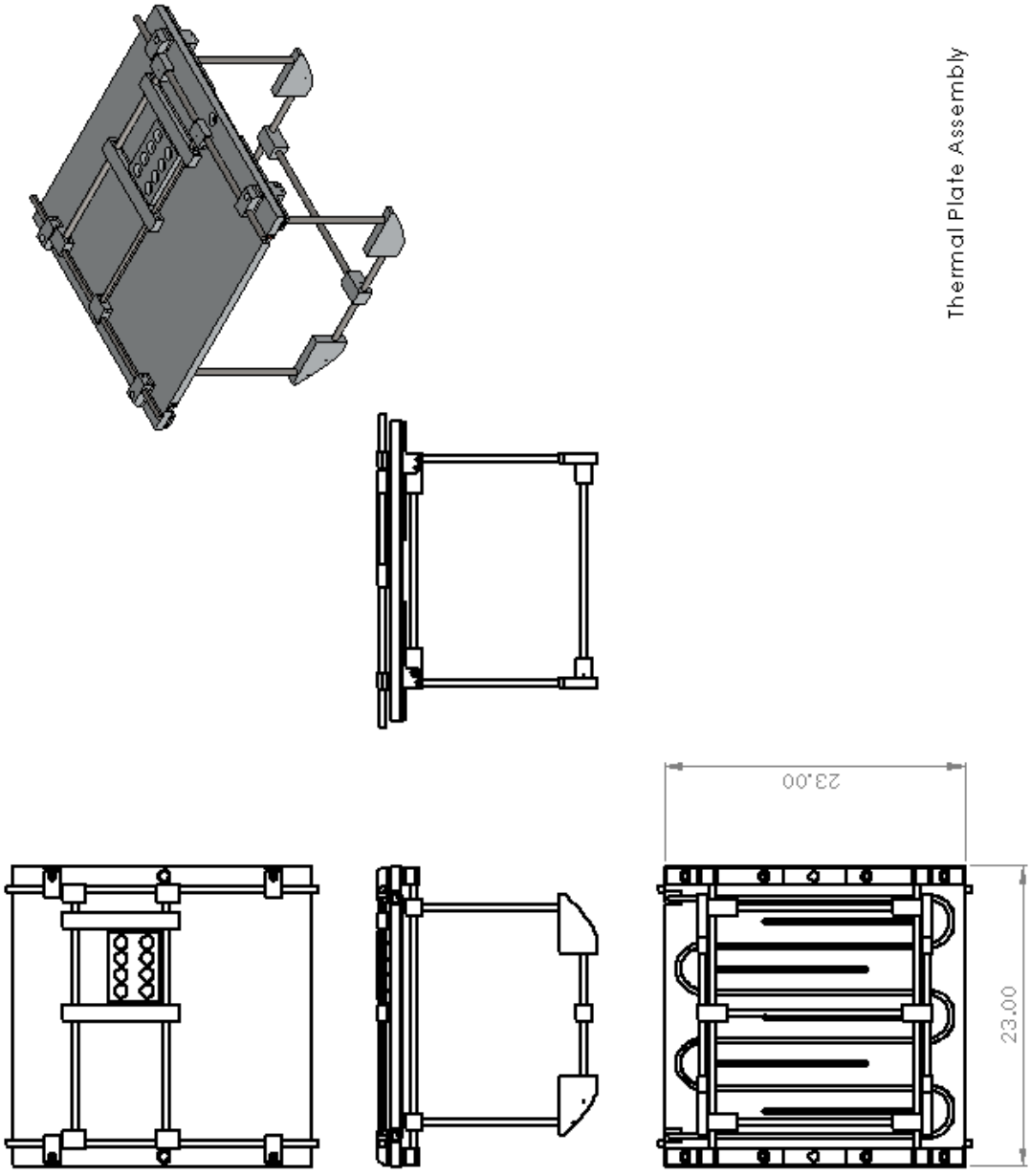

Figure B.2: Simplified CAD drawing of the thermal plate setup inside the Michigan Mars Environmental Chamber, showing a sample holder, the plate's insulation from the chamber walls, its cooling loops for the LN_2 and the cartridge heaters at the bottom of the thermal plate. Dimensions are in inches.

BIBLIOGRAPHY

Beegle, L. W., Bhartia, R., DeFlores, L. P., Asher, S. A., Burton, A. S., Clegg, S. M., … & Williford, K. H. (2014). SHERLOC: Scanning habitable environments with Raman & luminescence for organics & chemicals, an investigation for 2020. In *AGU Fall Meeting Abstracts*. Vol. 1, p. 06.

Bell III, J. (2008). *The Martian Surface-Composition, Mineralogy, and Physical Properties*. Cambridge University Press.

Biddanda, B. A., Nold, S. C., Ruberg, S. A., Kendall, S. T., Sanders, T. G., & Gray, J. J. (2009). Great Lakes sinkholes: a microbiogeochemical frontier. *EOS Transactions 90*(8), 61-62.

Boetius, A., & Joye, S. (2009). Thriving in salt. *Science, 324*(5934), 1523-1525.

Boynton, W. V., Feldman, W. C., Squyres, S. W., Prettyman, T. H., Brückner, J., Evans, L. G., ... & Englert, P. A. J. (2002). Distribution of hydrogen in the near surface of Mars: Evidence for subsurface ice deposits. *Science, 297*(5578), 81-85.

Brass, G. W. (1980). Stability of brines on Mars. *Icarus, 42*(1), 20-28.

Bryson, K. L., Chevrier, V., Sears, D. W., & Ulrich, R. (2008). Stability of ice on Mars and the water vapor diurnal cycle: Experimental study of the sublimation of ice through a fine-grained basaltic regolith. *Icarus, 196*(2), 446-458.

Byrne, S., Dundas, C. M., Kennedy, M. R., Mellon, M. T., McEwen, A. S., Cull, S. C., ... & Cantor, B. A. (2009). Distribution of mid-latitude ground ice on Mars from new impact craters. *Science, 325*(5948), 1674-1676.

Campbell, J. L., Gellert, R., Lee, M., Mallett, C. L., Maxwell, J. A., & O'Meara, J. M. (2008). Quantitative in situ determination of hydration of bright high-sulfate Martian soils. *Journal of Geophysical Research: Planets (1991–2012), 113*(E6).

Chevrier, V. F., & Altheide, T. S. (2008). Low temperature aqueous ferric sulfate solutions on the surface of Mars. *Geophysical Research Letters, 35*(22).

Chevrier, V. F., Hanley, J., & Altheide, T. S. (2009). Stability of perchlorate hydrates and their liquid solutions at the Phoenix landing site, Mars. *Geophysical Research Letters, 36*(10).

Chevrier, V. F., & Rivera-Valentin, E. G. (2012). Formation of recurring slope lineae by liquid brines on present-day Mars. *Geophysical Research Letters, 39*(21).

Clark, B. C. (1978). Implications of abundant hygroscopic minerals in the martian regolith. *Icarus, 34*, 645-665.

Clark, B. C., & Van Hart, D. C. (1981). The salts of Mars. *Icarus, 45*(2), 370-378.

Clark, B. C., Morris, R. V., McLennan, S. M., Gellert, R., Jolliff, B., Knoll, A. H., ... & Yen, A. (2005). Chemistry and mineralogy of outcrops at Meridiani Planum. *Earth and Planetary Science Letters, 240*(1), 73-94.

Conley, C. A., & Rummel, J. D. (2010). Planetary protection for human exploration of Mars. *Acta Astronautica, 66*(5-6), 792-797.

Cull, S. C., Arvidson, R. E., Catalano, J. G., Ming, D. W., Morris, R. V., Mellon, M. T., & Lemmon, M. (2010a). Concentrated perchlorate at the Mars Phoenix landing site: Evidence for thin film liquid water on Mars. *Geophysical Research Letters, 37*(22).

Cull, S., Arvidson, R. E., Morris, R. V., Wolff, M., Mellon, M. T., & Lemmon, M. T. (2010b). Seasonal ice cycle at the Mars Phoenix landing site: 2. Postlanding CRISM and ground observations. *Journal of Geophysical Research: Planets, 115*(E5).

Cull, S., Kennedy, E., & Clark, A. (2014). Aqueous and non-aqueous soil processes on the northern plains of Mars: insights from the distribution of perchlorate salts at the Phoenix landing site and in Earth analog environments. *Planetary and Space Science, 96*, 29-34.

Davila, A. F., Duport, L. G., Melchiorri, R., Jänchen, J., Valea, S., de los Rios, A., ... & Wierzchos, J. (2010). Hygroscopic salts and the potential for life on Mars. *Astrobiology, 10*(6), 617-628.

Davy, R., Davis, J. A., Taylor, P. A., Lange, C. F., Weng, W., Whiteway, J., & Gunnlaugson, H. P. (2010). Initial analysis of air temperature and related data from the Phoenix MET station and their use in estimating turbulent heat fluxes. *Journal of Geophysical Research: Planets, 115*(E3).

Dolenko, T. A., Churina, I. V., Fadeev, V. V., & Glushkov, S. M. (2000). Valence band of liquid water Raman scattering: some peculiarities and applications in the diagnostics of water media. *Journal of Raman Spectroscopy, 31*(8-9), 863-870.

Dundas, C. M., McEwen, A. S., Chojnacki, M., Milazzo, M. P., Byrne, S., McElwaine, J. N., & Urso, A. (2017). Granular flows at recurring slope lineae on Mars indicate a limited role for liquid water. *Nature Geoscience, 10*(12), 903.

Dundas, C. M., Bramson, A. M., Ojha, L., Wray, J. J., Mellon, M. T., Byrne, S., ... & Clark, E. (2018). Exposed subsurface ice sheets in the Martian mid-latitudes. *Science, 359*(6372), 199-201.

Fairén, A. G., Davila, A. F., Gago-Duport, L., Amils, R., & McKay, C. P. (2009). Stability against freezing of aqueous solutions on early Mars. *Nature, 459*(7245), 401.

Farmer, C. B. (1976). Liquid water on Mars. *Icarus, 28*(2), 279-289.

Feldman, W. C., Boynton, W. V., Tokar, R. L., Prettyman, T. H., Gasnault, O., Squyres, S. W., ... & McKinney, G. W. (2002). Global distribution of neutrons from Mars: Results from Mars Odyssey. *Science, 297*(5578), 75-78.

Ferris, J. C., Dohm, J. M., Baker, V. R., & Maddock, T. (2002). Dark slope streaks on Mars: Are aqueous processes involved?. *Geophysical Research Letters, 29*(10).

Fischer, E., Martínez, G. M., Elliott, H. M., & Rennó, N. O. (2014). Experimental evidence for the formation of liquid saline water on Mars. *Geophysical Research Letters, 41*(13), 4456-4462.

Fischer, E., Martínez, G. M., & Rennó, N. O. (2016). Formation and persistence of brine on Mars: experimental simulations throughout the diurnal cycle at the Phoenix landing site. *Astrobiology, 16*(12), 937-948.

Glavin, D. P., Freissinet, C., Miller, K. E., Eigenbrode, J. L., Brunner, A. E., Buch, A., ... & Cabane, M. (2013). Evidence for perchlorates and the origin of chlorinated hydrocarbons detected by SAM at the Rocknest aeolian deposit in Gale Crater. *Journal of Geophysical Research: Planets, 118*(10), 1955-1973.

Gough, R. V., Chevrier, V. F., Baustian, K. J., Wise, M. E., & Tolbert, M. A. (2011). Laboratory studies of perchlorate phase transitions: Support for metastable aqueous perchlorate solutions on Mars. *Earth and Planetary Science Letters, 312*(3-4), 371-377.

Green, W. J., & Lyons, W. B. (2009). The Saline Lakes of the McMurdo Dry Valleys, Antarctica. *Aquatic geochemistry, 15*(1-2), 321-348.

Haberle, R. M., McKay, C. P., Schaeffer, J., Cabrol, N. A., Grin, E. A., Zent, A. P., & Quinn, R. (2001). On the possibility of liquid water on present-day Mars. *Journal of Geophysical Research: Planets (1991–2012), 106*(E10), 23317-23326.

Hall, D. L., Sterner, S. M., & Bodnar, R. J. (1988). Freezing point depression of NaCl-KCl-H_2O solutions. *Economic Geology, 83*(1), 197-202.

Harri, A. M., Genzer, M., Kemppinen, O., Gomez-Elvira, J., Haberle, R., Polkko, J., ... & Richardson, M. (2014). Mars Science Laboratory relative humidity observations: Initial results. *Journal of Geophysical Research: Planets, 119*(9), 2132-2147.

Hecht, M. H., Marshall, J., Pike, W. T., Staufer, U., Blaney, D., Braendlin, D., ... & Markiewicz, W. J. (2008). Microscopy capabilities of the microscopy, electrochemistry, and conductivity analyzer. *Journal of Geophysical Research: Planets, 113*(E3).

Hecht, M. H., Kounaves, S. P., Quinn, R. C., West, S. J., Young, S. M. M., Ming, D. W., ... & DeFlores, L. P. (2009). Detection of perchlorate and the soluble chemistry of martian soil at the Phoenix lander site. *Science, 325*(5936), 64-67.

Heinz, J., Schulze-Makuch, D., & Kounaves, S. P. (2016). Deliquescence-induced wetting and RSL-like darkening of a Mars analogue soil containing various perchlorate and chloride salts. *Geophysical Research Letters, 43*(10), 4880-4884.

Jakosky, B. M., & Phillips, R. J. (2001). Mars' volatile and climate history. *Nature, 412*(6843), 237.

Joye, S. B., & Samarkin, V. A. (2009). Metabolic variability in seafloor brines revealed by carbon and sulphur dynamics. *Nature Geoscience, 2*(5), 349-354.

Junge, K., Krembs, C., Deming, J., Stierle, A., & Eicken, H. (2001). A microscopic approach to investigate bacteria under in situ conditions in sea-ice samples. *Annals of Glaciology, 33*(1), 304-310.

King, C. M., Schorghofer, N., & Wagstaff, K. L. (2010). Martian slope streaks form sporadically throughout the year. In *Lunar and Planetary Science Conference* (Vol. 41, p. 1542).

Kok, J. F., & Renno, N. O. (2009). A comprehensive numerical model of steady state saltation (COMSALT). *Journal of Geophysical Research: Atmospheres, 114*(D17).

Kounaves, S. P., Chaniotakis, N. A., Chevrier, V. F., Carrier, B. L., Folds, K. E., Hansen, V. M., ... & Weber, A. W. (2014). Identification of the perchlorate parent salts at the Phoenix Mars landing site and possible implications. *Icarus, 232*, 226-231.

Kreslavsky, M. A., & Head, J. W. (2009). Slope streaks on Mars: A new “wet” mechanism. *Icarus, 201*(2), 517-527.

Leshin, L. A., Mahaffy, P. R., Webster, C. R., Cabane, M., Coll, P., Conrad, P. G., ... & Eigenbrode, J. L. (2013). Volatile, isotope, and organic analysis of martian fines with the Mars Curiosity rover. *Science, 341*(6153), 1238937.

Lewis, S. R., Collins, M., Read, P. L., Forget, F., Hourdin, F., Fournier, R., ... & Huot, J. P. (1999). A climate database for Mars. *Journal of Geophysical Research: Planets, 104*(E10), 24177-24194.

Mahaffy, P. R., Webster, C. R., Atreya, S. K., Franz, H., Wong, M., Conrad, P. G., ... & Owen, T. (2013). Abundance and isotopic composition of gases in the Martian atmosphere from the Curiosity rover. *Science, 341*(6143), 263-266.

Marion, G. M., Catling, D. C., Zahnle, K. J., & Claire, M. W. (2010). Modeling aqueous perchlorate chemistries with applications to Mars. *Icarus, 207*(2), 675-685.

Martín-Torres, F. J., Zorzano, M. P., Valentín-Serrano, P., Harri, A. M., Genzer, M., Kemppinen, O., ... & Goetz, W. (2015). Transient liquid water and water activity at Gale crater on Mars. *Nature Geoscience, 8*(5), 357.

Martínez, G. M., Renno, N. O., & Elliott, H. M. (2012). The evolution of the albedo of dark spots observed on Mars polar region. *Icarus, 221*(2), 816-830.

Martínez, G. M., & Renno, N. O. (2013). Water and brines on Mars: current evidence and implications for MSL. *Space Science Reviews, 175*(1-4), 29-51.

Martínez, G. M., Fischer, E., Rennó, N. O., Sebastián, E., Kemppinen, O., Bridges, N., ... & Vicente-Retortillo, A. (2016). Likely frost events at Gale crater: Analysis from MSL/REMS measurements. *Icarus, 280*, 93-102.

Martínez, G. M., Newman, C. N., De Vicente-Retortillo, A., Fischer, E., Renno, N. O., Richardson, M. I., ... & Harri, A. M. (2017). The modern near-surface Martian climate: A review of in-situ meteorological data from Viking to Curiosity. *Space Science Reviews, 212*(1-2), 295-338.

McEwen, A. S., Ojha, L., Dundas, C. M., Mattson, S. S., Byrne, S., Wray, J. J., ... & Gulick, V. C. (2011). Seasonal flows on warm Martian slopes. *Science, 333*(6043), 740-743.

Meslin, P. Y., Gasnault, O., Forni, O., Schröder, S., Cousin, A., Berger, G., ... & Le Mouélic, S. (2013). Soil diversity and hydration as observed by ChemCam at Gale Crater, Mars. *Science, 341*(6153), 1238670.

Mikucki, J. A., Pearson, A., Johnston, D. T., Turchyn, A. V., Farquhar, J., Schrag, D. P., ... & Lee, P. A. (2009). A Contemporary Microbially Maintained Subglacial Ferrous" Ocean". *Science, 324*(5925), 397-400.

Miller, A. G., & Macklin, J. W. (1985). Vibrational spectroscopic studies of sodium perchlorate contact ion pair formation in aqueous solution. *The Journal of Physical Chemistry, 89*(7), 1193-1201.

Ming, D. W., Archer, P. D., Glavin, D. P., Eigenbrode, J. L., Franz, H. B., Sutter, B., ... & Mahaffy, P. R. (2014). Volatile and organic compositions of sedimentary rocks in Yellowknife Bay, Gale Crater, Mars. *Science, 343*(6169), 1245267.

Mirabel, P., Reiss, H., & Bowles, R. K. (2000). A theory for the deliquescence of small particles. *The Journal of Chemical Physics, 113*(18), 8200-8205.

Mitrofanov, I., Anfimov, D., Kozyrev, A., Litvak, M., Sanin, A., Tret'yakov, V., ... & Hamara, D. (2002). Maps of subsurface hydrogen from the high energy neutron detector, Mars Odyssey. *Science, 297*(5578), 78-81.

Möhlmann, D. T. F. (2008), The influence of van der Waals forces on the state of water in the shallow subsurface of Mars. *Icarus 195*.1, 131-139.

Möhlmann, D.T.F. (2011), Latitudinal distribution of temporary liquid cryobrines on Mars. *Icarus, 214*, 236-239.

Moore, J. M., & Bullock, M. A. (1999). Experimental studies of Mars-analog brines. *Journal of Geophysical Research: Planets, 104*(E9), 21925-21934.

Moores, J. E., Lemmon, M. T., Smith, P. H., Komguem, L., & Whiteway, J. A. (2010). Atmospheric dynamics at the Phoenix landing site as seen by the Surface Stereo Imager. *Journal of Geophysical Research: Planets, 115*(E1).

Nikolakakos, G., & Whiteway, J. A. (2015). Laboratory investigation of perchlorate deliquescence at the surface of Mars with a Raman scattering lidar. *Geophysical Research Letters, 42*(19), 7899-7906.

Nuding, D., Rivera-Valentin, E. G., Gough, R. V., Chevrier, V. F., & Tolbert, M. A. (2013). Deliquescence of calcium perchlorate: An investigation of stable aqueous solutions relevant to Mars. In *AAS/Division for Planetary Sciences Meeting Abstracts* (Vol. 45).

Nuding, D. L., Rivera-Valentin, E. G., Davis, R. D., Gough, R. V., Chevrier, V. F., & Tolbert, M. A. (2014). Deliquescence and efflorescence of calcium perchlorate: an investigation of stable aqueous solutions relevant to Mars. *Icarus, 243*, 420-428.

Nuding, D. L., Davis, R. D., Gough, R. V., & Tolbert, M. A. (2015). The aqueous stability of a Mars salt analog: instant Mars. *Journal of Geophysical Research: Planets, 120*(3), 588-598.

Ojha, L., Wilhelm, M. B., Murchie, S. L., McEwen, A. S., Wray, J. J., Hanley, J., ... & Chojnacki, M. (2015). Spectral evidence for hydrated salts in recurring slope lineae on Mars. *Nature Geoscience, 8*(11), 829.

Osterloo, M. M., Hamilton, V. E., Bandfield, J. L., Glotch, T. D., Baldridge, A. M., Christensen, P. R., ... & Anderson, F. S. (2008). Chloride-bearing materials in the southern highlands of Mars. *Science, 319*(5870), 1651-1654.

Pankine, A. A., & Tamppari, L. K. (2015). Constraints on water vapor vertical distribution at the Phoenix landing site during summer from MGS TES day and night observations. *Icarus, 252*, 107-120.

Rao, M. N., Sutton, S. R., McKay, D. S., & Dreibus, G. (2005). Clues to Martian brines based on halogens in salts from nakhlites and MER samples. *Journal of Geophysical Research: Planets, 110*(E12).

Read, P. L., & Lewis, S. R. (2004). *The Martian climate revisited: atmosphere and environment of a desert planet*. Springer Science & Business Media.

Rennó, N. O., Bos, B. J., Catling, D., Clark, B. C., Drube, L., Fisher, D., ... & Kounaves, S. P. (2009). Possible physical and thermodynamical evidence for liquid water at the Phoenix landing site. *Journal of Geophysical Research: Planets, 114*(E1).

Rull, F., Maurice, S., Diaz, E., Lopez, G., & Catala, A. (2013, March). Raman Laser Spectrometer (RLS) for Exomars 2018 Rover Mission: Current status and science operation mode on powdered samples. In *Lunar and Planetary Science Conference* (Vol. 44, p. 3110).

Savijärvi, H., & Määttänen, A. (2010). Boundary-layer simulations for the Mars Phoenix lander site. *Quarterly Journal of the Royal Meteorological Society, 136*(651), 1497-1505.

Savijärvi, H. I., Harri, A. M., & Kemppinen, O. (2015). Mars Science Laboratory diurnal moisture observations and column simulations. *Journal of Geophysical Research: Planets, 120*(5), 1011-1021.

Schmidt, M. E., Ruff, S. W., McCoy, T. J., Farrand, W. H., Johnson, J. R., Gellert, R., ... & Schroeder, C. (2008). Hydrothermal origin of halogens at Home Plate, Gusev crater. *Journal of Geophysical Research: Planets, 113*(E6).

Schorghofer, N., & Aharonson, O. (2005). Stability and exchange of subsurface ice on Mars. *Journal of Geophysical Research: Planets, 110*(E5).

Sheehan, W. (1996). The planet Mars: A history of observation & discovery. University of Arizona Press.

Smith, P. H., Tamppari, L. K., Arvidson, R. E., Bass, D., Blaney, D., Boynton, W. V., ... & DeJong, E. (2009). H_2O at the Phoenix landing site. *Science, 325*(5936), 58-61.

Sullivan, R., Thomas, P., Veverka, J., Malin, M., & Edgett, K. S. (2001). Mass movement slope streaks imaged by the Mars Orbiter Camera. *Journal of Geophysical Research: Planets, 106*(E10), 23607-23633.

Tamppari, L. K., Bass, D., Cantor, B., Daubar, I., Dickinson, C., Fisher, D., ... & Kleinböhl, A. (2010). Phoenix and MRO coordinated atmospheric measurements. *Journal of Geophysical Research: Planets, 115*(E5).

Taylor, F. W. (2010). The scientific exploration of Mars. Cambridge, UK, New York: Cambridge University Press.

Thomas, D. N., & Dieckmann, G. S. (2002). Antarctic sea ice--a habitat for extremophiles. *Science, 295*(5555), 641-644.

Vincendon, M., Forget, F., & Mustard, J. (2010). Water ice at low to midlatitudes on Mars. *Journal of Geophysical Research: Planets, 115*(E10).

Wall, S. D. (1981), Analysis of condensates formed at the Viking 2 Lander site: The first winter. *Icarus 47*(2), 173-183.

Williams, D. R. (2016, December 23). *Mars Fact Sheet*. Retrieved from https://nssdc.gsfc.nasa.gov/planetary/factsheet/marsfact.html.

Wilson, J. T., Eke, V. R., Massey, R. J., Elphic, R. C., Feldman, W. C., Maurice, S., & Teodoro, L. F. (2018). Equatorial locations of water on Mars: Improved resolution maps based on Mars Odyssey Neutron Spectrometer data. *Icarus, 299*, 148-160.

Whiteway, J. A., Komguem, L., Dickinson, C., Cook, C., Illnicki, M., Seabrook, J., ... & Pathak, J. (2009). Mars water-ice clouds and precipitation. *Science, 325*(5936), 68-70.

Zandonadi, D., Jr., Renno, N. O., Fischer, E. (2015). WET – A soil wetness sensor for Mars. In *66th International Astronautical Congress*.

Zent, A. P., Hecht, M. H., Cobos, D. R., Campbell, G. S., Campbell, C. S., Cardell, G., ... & Mehta, M. (2009). Thermal and electrical conductivity probe (TECP) for Phoenix. *Journal of Geophysical Research: Planets, 114*(E3).

Zent, A. P., Hecht, M. H., Cobos, D. R., Wood, S. E., Hudson, T. L., Milkovich, S. M., ... & Mellon, M. T. (2010). Initial results from the thermal and electrical conductivity probe (TECP) on Phoenix. *Journal of Geophysical Research: Planets*, *115*(E3).

Zent, A. P., Hecht, M. H., Hudson, T. L., Wood, S. E., & Chevrier, V. F. (2012). A revised calibration function for the TECP humidity sensor of the Phoenix mission. In *Lunar and Planetary Science Conference* (Vol. 43).

Zent, A. P., Hecht, M. H., Hudson, T. L., Wood, S. E., & Chevrier, V. F. (2016). A revised calibration function and results for the Phoenix mission TECP relative humidity sensor. *Journal of Geophysical Research: Planets*, *121*(4), 626-651.

Zhang, Y. H., & Chan, C. K. (2003). Observations of water monomers in supersaturated $NaClO_4$, $LiClO_4$, and $Mg(ClO_4)_2$ droplets using Raman spectroscopy. *The Journal of Physical Chemistry A*, *107*(31), 5956-5962.

Zorzano, M. P., Mateo-Martí, E., Prieto-Ballesteros, O., Osuna, S., & Renno, N. (2009). Stability of liquid saline water on present day Mars. *Geophysical Research Letters*, *36*(20).